NTNU

Norwegian University of
Science and Technology

Design and Analysis of Stationary Reference Frame Controllers for Active Front End Converter

Arne Sigurd Holter

Master of Energy and Environmental Engineering
Submission date: June 2016
Supervisor: Roy Nilsen, ELKRAFT

Norwegian University of Science and Technology
Department of Electric Power Engineering

Problem Description

In the course of the last years, an increasing number of DC based distributed generation units have been connected to the external utility AC grid. For smart and seamless integration of these units, active front end converters together with their associated control systems have been utilized, due to their proven abilities for providing high quality, suitable power conversion.

Traditionally, the conventional power production has been based on large centralized power plants. Due to an increasing demand of electrical power on one hand, and environmental issues and limited amounts of fossil energy resources on the other, one sees a trend in the development of the electrical infrastructure towards a more decentralized power generation system, integrating more small-scale renewable distributed energy generation units as well as their associated power electronic converters. Unlike the conventional power plants, distributed generation units lack some of the favorable properties of these generators, and might compromise grid stability and power quality, depending on their technology, penetration and control. A successful integration of these converters is therefore highly dependent on the implementation of their control system. In order to proactively tackle these issues, this is the selected topic to be studied in this thesis, with the following tasks to be performed:

1. The state-of-the-art for active front end converters is identified
2. The operation of the converter and possible implementations of its control system are examined
3. A mathematical system model is to be derived for control design purposes
4. A digital simulation model is developed for testing and analysis of the performance of different stationary reference frame current- and voltage controllers

Abstract

Application of power electronic converters in distributed energy generation systems has been a rapid growing technology over the last years, the control of these systems being the topic of much research. One of these types of converters is the *active front end* (AFE) converter, some of its main advantageous properties including the possibility of bidirectional power flow, also making it applicable for electrical drive systems.

In this thesis, literature is considered for identifying the state-of-the-art and possible system implementations of an active front end converters along with its associated control system.

A mathematical model of an AFE converter system is derived in the continuous frequency domain, and eight different current controllers are separately studied and designed considering this model. Out of these controllers, a discretized model of a proportional integral multi-resonant controller is designed, and a double loop cascaded control system is considered, employing this type of controllers.

Furthermore, a discretized simulation model of the system is developed, to aid controller design and for controller evaluation purposes. The inherent shortcomings of *proportional* (P), *proportional integral* (PI), and *proportional integral derivative* (PID) controllers for tracking of sinusoidal references in the stationary $\alpha\beta$-reference frame are examined. It will be shown, that successful tracking performance is achieved in the simulation model, using a single loop PI multi-resonant current control system, and in a double loop cascaded control employing this type of controllers. Moreover, the ability of resonant harmonic compensation is studied in a simulation environment, using PI multi-resonant controllers when connected to a three-phase full-bridge diode rectifier.

Sammendrag

Bruken av kraftelektroniske omformere i distribuerte kraftsystemer har gjennomgått en rask teknologisk utvikling i de siste årene, og de tilhørende styresystemene har vært tema for mange forskningsprosjekter. En av disse omformerne er den aktive likeretteren, med fordeler som blant annet inkluderer toveis effektflyt, noe som også gjør den egnet til bruk i elektriske motordrifter.

I denne oppgaven vil litteratur bli betraktet for å identifisere "state-of-the-art", i tillegg til ulike systemimplementasjoner for den aktive likeretteren og dens styresystem.

En matematisk modell av et aktivt likerettersystem er utledet i det kontinuerlige frekvensdomenet, og åtte ulike strømkontrollere er designet for denne modellen. Av disse kontrollerne vil en digital modell av en proporsjonal integral multiresonant kontroller bli designet, i tillegg til et dobbelsløyfe-kaskade kontrollsystem som benytter denne typen kontroller.

Videre, vil en digital simuleringsmodell av systemet bli utviklet som en del av designprosessen, og for å teste og sammenligne de ulike kontrollerne. Ulempene ved bruk av *proporsjonal-* (P), *proporsjonal integral-* (PI) og *proporsjonal integral derivat-* (PID) kontrollere ved følging av sinusformede referanser i stasjonært $\alpha\beta$-referansesystem er undersøkt. Det vil bli vist at suksessfull følging er oppnådd i simuleringsmodellen med en enkel strømkontrollsløyfe ved bruk av PI multi-resonant kontrollere, og i et dobbelsløyfes kaskadekontrollsystem med bruk av samme type kontrollere. I tillegg er konseptet som omfatter harmonisk kompensering studert og testet i simuleringsmodellen ved bruk av PI multi-resonante kontrollere i et tilfelle der omformeren er koblet til en trefase diodelikeretterbru.

Preface

This thesis was written as a part of the master's programme at the Department of Electrical Power Engineering at the Norwegian University of Science and Technology. The work was carried out during the spring semester of 2016.

I first encountered power electronic converters and their control in my earlier years at NTNU and wanted to learn more about them. I therefore selected this, as the topic of my specialization project in the autumn semester. A relevant problem description for my master's thesis regarding control of active front end converters was further specified in the beginning of this semester, in close cooperation with my supervisor, Dr. Roy Nilsen, of Wärtsilä Norway AS.

The readers of this report are assumed to have an academic background from power engineering, and a basic understanding of power electronics and control theory.

Acknowledgment

First, and foremost, I would like to thank my supervisor, professor Roy Nilsen. Writing a master's thesis is certainly not always a straight-forward task, and without his guidance, I would certainly not have been able to reach the results that are presented in this report.

Now that this chapter of my academical career is about to come to an end, I would also like to thank my study colleges for making this time a memorable and joyful one.

Finally, I would like to thank my family and friends for always supporting me through the more difficult time periods.

Contents

List of Tables

List of Figures

Nomenclature

Abbreviations:

AC	Alternating Current
AFE	Active Front End
DC	Direct Current
DER	Distributed Energy Resources
DG	Distributed Generation
MO	Modulus Optimum
MOSFET	Metal–Oxide–Semiconductor Field-Effect Transistor
PI	Proportional Integral
PID	Proportional Integral Derivative
PR	Proportional Resonant
PWM	Pulse Width Modulation
RHC	Resonant Harmonic Compensation
RMS	Root Mean Square
SO	Symmetrical Optimum
SRF	Synchronous Reference Frame
SVPWM	Space Vector Pulse Width Modulation
TDD	Total Demand Distortion
THD	Total Harmonic distortion
THIPWM	Third Harmonic Injection Pulse Width Modulation
VISMA	Virtual Synchronous Machine

Symbols:

ϕ^*	Target lead angle
ϕ	Lead angle
ψ	Phase margin
ω_{135}	Angular frequency corresponding to system phase of -135°
ω_0	Rated electrical angular velocity
A	Total harmonic power
a	Symmetrical optimum tuning factor
B	Symmetrical optimum-acceleration parameter
C	Filter capacitor
$D(s)$	Regulator transfer function

$e(s)$	Regulator error signal	Q	Reactive power
$F(s)$	Anti-aliasing transfer function	S	Apparent power
f_0	Fundamental grid-frequency	S_i	Transistor in phase/converter leg, i
$G(s)$	Plant transfer function	Sw_i	Switching function of converter leg, i
H	Harmonic Power	T_1	Plant time constant
h	Individual harmonic component	T_d	PID controller derivative time constant
$h_{0i}(s)$	Open current control loop transfer function	T_{dsp}	Processor time delay
$h_{0i,n}(s)$	Open current control loop-transfer function, with no controller	T_f	Anti-aliasing time delay
$h_v(s)$	Disturbance transfer function	T_i	Controller integral time constant
i_1	Converter side current	T_{pwm}	Modulator time delay
i_2	Grid side current	T_{sum}	Equivalent time delay
i_c	Capacitor current	T_{sw}	Converter switching period
I_L	Demand load current at PCC	v_1	Converter output voltage
I_n	Rated converter output current	v_2	Grid side voltage
I_{sc}	Short-circuit current at PCC	v_c	Capacitor voltage
K_{135}	Gain corresponding to phase of -135°	V_{carr}	Carrier voltage
K_c	PID controller gain	V_{dc}	DC link voltage
K_i	PI controller gain	V_{LL}	RMS line-voltage
L_1	Filter inductance	V_n	Rated converter RMS output voltage
M_a	Modulation index	V_r	Voltage reference vector amplitude
$M(s)$	Modulator transfer function	$v^*_{a,b,c}$	Voltage reference for phase a,b,c
P	Active power	Z_{base}	Converter impedance base value
$P(s)$	Processor transfer function		

Chapter 1

Introduction

1.1 Background and Motivation

Currently, the worldwide electrical infrastructure is undergoing an extensive change, driven by an increasing demand for electrical energy, environmental issues, energy politics, and a rapid technological development, especially in the field of power electronics. This change is a gradual process towards the realization of the smart grid, a vision of the future power system where the flow of electrical power and communication between producer and consumer are to becoming bidirectional.

The development and integration of *distributed generation* (DG) is an another important aspect of this change, in which the traditional centralized power generation plants are to be complemented by a higher penetration of low-scale production plants at the distribution level. In the course of the last years, the worldwide installed power, based on *distributed energy resources* (DER), such as grid-connected photovoltaic power plants and wind turbines, have experienced an exponential growth. As a result, the total generation capacity as well as the penetration of renewable environmental friendly energy resources are increasing. Incorporating these resources inside microgrids that can either be operated in grid-connected mode or in islanded mode, appears to be a promising way of obtaining smart implementation of these resources in the energy system. However, this development is causing the grid structure to become ever more complex. Moreover, acknowledging the intermittent nature of many of the renewable energy resources,

their performances depending on meteorological and geographical conditions, the total power generation is prone to become more volatile. Further, the grid-stability, power quality and reliability can be compromised, based on the penetration, technology and the control of these distributed energy resources. Traditionally, these challenges have been met by utilizing large rotating masses of synchronous generators in large, conventional power plants. Now, they also have to be solved at the distribution level, in order to realize the vast potential related to the smart grid paradigm and renewable distributed energy resources.

The key for overcoming these challenges is related to the control and co-ordination of the individual power generation units, that is, the control of their corresponding power electronic converters. This topic has gained a lot of interest in research, and the field of power electronic converters and their control have experienced a vast development over the last years. In literature, numerous proven solutions have been put forward on converter technologies, topologies and control algorithms for grid-synchronization, current- and voltage control, anti-islanding strategies, and more, all with the objective of improving the performance and operation of distributed energy resources. The most basic task of these controllers is to inject suitable AC current and voltage signals into the external utility grid. In recent years, resonant type controllers have gained much attention in research due to their ability of managing this task, also when employed in the stationary reference frame.

In this thesis, the properties of the active front end converter will be studied along with its operation, and different stationary reference frame current- and voltage controllers will be considered, including resonant type controllers.

Problem Formulation

The problem to be studied in this thesis is formulated as follows:

"Which controllers can be embedded in the current and voltage control structure of an active front end converter system and how do they differ in terms of their implementation and performance when tracking a fundamental frequency sinusoidal reference? An active front

end converter system with different stationary reference frame controllers is to be modeled, designed and tested for further investigation of this problem using a simulation software."

This is a problem of high relevance due to the current development of the electrical grid infrastructure, where an increasing number of DER systems are being connected to the electrical grid, and thus, more power electronic applications. If the current development is to proceed into the coming years, solutions have to be made for the control of these systems in order to retain power quality, grid reliability and stability. Suitable power conversion is the most fundamental and crucial part of this control.

1.2 Objectives

The main objectives of this thesis are summarized below:

1. To identify the state-of-the-art for active front end converters
2. To present the operation and possible implementations of the converter and its control system
3. To derive a mathematical model of the AFE converter system for control design purposes
4. To develop a digital simulation model for testing and evaluation of the performance of different stationary reference frame current- and voltage controllers

1.3 Limitations

Some of the most important limitations of this study are presented in this section.

Perhaps the most important limitation of this type of work, is time. Dealing with a problem as comprehensive as the one of this thesis, there are numerous possibilities of how to approach it, as well as there are different aspects of it to examine. However, time is a very limited resource

in this type of work. To limit the scope of work is therefore of great importance.

Another limitation of the work in this study is the use of mathematical models and simulation software. In many cases, models and simulation software provide results with a satisfactory degree of precision, reflecting the physical reality of the system of interest. Unfortunately, these tools have clear limitations, compared to the actual reality. Therefore, ideally, a laboratory set-up should have been made for testing of the physical system of interest, and comparing these results to those obtained from the simulation model. However, due to the time limitation already mentioned, the practical approach of this problem is, as for now, put in the list of "Further Work".

1.4 Approach

The work of this thesis can be divided into three main parts: Literature study, controller design and simulation testing.
In order to meet the four objectives presented in Section 1.2, the following corresponding scientific approaches are used throughout this thesis:

1. For identifying the state-of-the art for active front end converters, a literature study will be conducted, considering scientific articles as well as other relevant literature.

2. Relevant literature will also be considered for studying the converter operation, its different controllers and possible control system implementations.

3. Scientific articles, theses and dissertations will be studied in order to derive a mathematical model of the active converter. Literature will also be studied for optimization of current and voltage controllers, and their design will be performed using the mathematical programming tool, "Matlab".

4. In order to test the individual stationary reference frame controllers of the active front end converter, a model in the block-diagram simulation environment, "Simulink", will be developed, based on the findings from the literature study and the mathematical model of the system. This simulation model will be an extension of an existing model that already

contains some of the basic system function blocks. The results from the simulations are to be compared to those of the design process, as well as with the findings from the literature study.

1.5 Outline of Report

The rest of this report is organized as follows:

Chapter 2 provides a brief introduction and presentation of the state-of-art for active front end converters

In Chapter 3, the system components and the basic operation of the converter is described with the objective of reaching a mathematical model of the system phase voltages in the time-domain.

Chapter 4 presents the underlying theory and some of the possible implementations of the converter control system. The different control reference frames are reviewed, as is some of the possible current- and voltage controllers, and their corresponding optimization strategies are introduced. Theory behind the discretization process of resonant controllers is also provided in this chapter.

In Chapter 5, the background theory of harmonics and LC filter design is given, as well as some of the standards regarding distortion limits.

Chapter 6 describes the procedure in which the AFE rectifier and corresponding control system models are elaborated and designed in the continuous frequency-domain. First, eight different controllers of the inner current loop are considered, before the outer voltage control loop is studied and designed, employing a PI multi-resonant controller.

In Chapter 7, simualation results are provided of seven case studies testing some of the con-

trollers considered in Chapter 6. These results are also compared to the behavior that should be expected based on the results of the design process of Chapter 6.

Finally, the results obtained throughout are discussed, and conclusions made in Chapter 8. Recommendations for further work are provided in this chapter, as well.

Chapter 2

State-of-the-Art for Active Front End Converters

The active front end converter is a three-phase power electronic converter connected to the grid through a passive filter, consisting of either an inductor or a combination of capacitors and inductors. Its applications are mainly those of suitable power conversion for grid-connected electrical applications, electrical motor drives and power conditioning. The converter can also be referred to as an *active rectifier* or a *voltage source converter*.

Over the course of the last years, an increasing number of these power electronic converters have been installed in the electrical grid. This is due to their many appealing characteristics, driven by the ever advancing technological development of power electronics, high-power semiconductor devices, and advanced control strategies [1], [2]. An adapted list from [3], [4], of some of the beneficial characteristics of the active front end converter is given below:

- **Reduced harmonic distortion in the grid**

  Because the AFE converter draws sinusoidal currents from the grid, the harmonic distortion in the grid current and voltage can be limited to ~ 1-5%, independent of the operation status, which is less than what can be achieved with diode and thyristor based converters.

- **Controllable DC voltage**

  Using an AFE converter, the DC voltage level can be controlled, allowing it to be kept constant at different points of operation.

- **Bidirectional power flow**

  The ability of the AFE converter to transfer power in both directions is perhaps its most important feature, making it applicable for generative breaking in motor drives and in energy storage systems. Moreover, the converter can be applied in conventional unidirectional power generation units.

- **Active power filter capability**

  Due to its ability to control the grid-current, the AFE converter can be used for power conditioning purposes by actively injecting currents of non-fundamental frequency into the grid, achieving harmonic cancellation.

- **Reactive power control**

  The reactive power flow of the AFE converter is controllable, meaning that the power factor can be selected and unity power factor can be maintained.

- **Improvement of grid-stability**

  Through the concepts of active filtering and reactive power control, the converter can contribute to increase the overall grid-stability. This positive effect on grid-stability can be further enhanced by connecting the converter to an energy storage system and integrating *virtual synchronous machine* (VISMA) functionalities, such as virtual damping and inertia in the converter control structure, [5].

The performance of the converter is usually evaluated in terms of its efficiency, the output power quality, measured in the harmonic distortion injected into the main grid, the complexity of its circuit topology and control system, and the implementation cost. Traditionally, the two level AFE converter solution has been utilized, but in recent years, modular multilevel converter topologies have gained increased interest. This is mainly due to their increased redundancy following their modular structure, their increased voltage capability, lower switching losses, and reduced harmonic distortion, compared to that related to the conventional two-level converters at the same switching frequency [6]. However, a drawback with multilevel converters is, that as their size, circuit topology, and their control structure increase, the number of transistors, circuit components and state variables increase, as well [7].

Chapter 3

Active Front End Converter Operation and Modeling

This chapter aims to give an introduction to the operation and modeling of the AFE rectifier system employing a three-phase two-level power electronic converter. This is done in order to provide the basic understanding of the system of interest in this thesis, and how it can be modeled for simulation purposes. A schematic of a two-level three-phase converter model is given in Figure 3.1, adapted from [8].

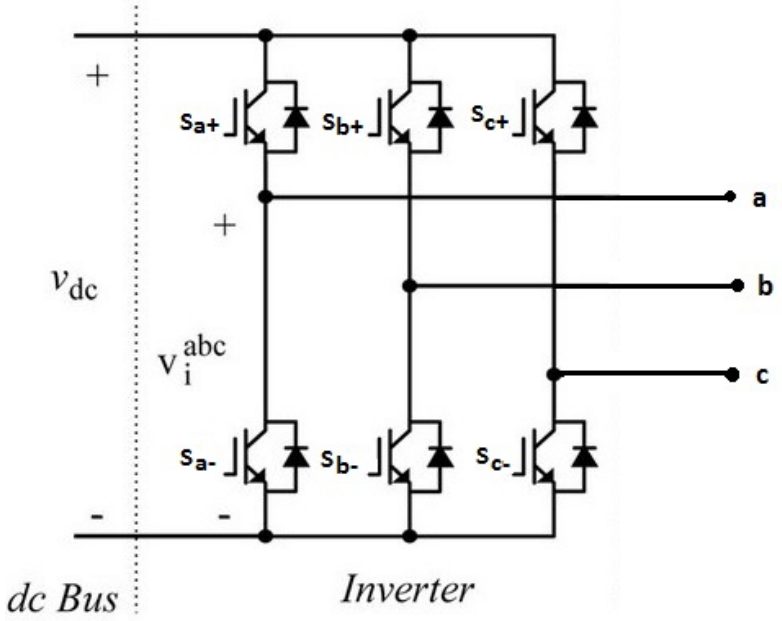

Figure 3.1: Three-phase two-level converter model, adapted from [8].

The converter is connected to a DC bus on one side, and an AC network on the other. Each phase on the AC side is connected to one of the three converter legs. In this topology, two transistors, with their corresponding anti-parallel diodes are present in each converter leg, the individual transistor states being controlled by gate signals. Only one of the two transistors in the same leg can be open at a time. They can both be open simultaneously, but both transistors in one leg can not be closed at the same time. If this is to occur, the DC bus will be short-circuited, and the transistors may be destroyed. In order to prevent this from happening, a blanking time is normally introduced in the switching operation of the converter. The switching procedure described above, enables the converter to output two different voltage levels, $\pm v_{dc}$, hence, the name, *two-level* converter.

For system modeling, a switching function, Sw_i can be defined, with subscript, $i = a, b, c$, referring to the phase of interest. By allowing, $Sw_i = 1$ to represent the transistor on-state, and $Sw_i = 0$ to represent the transistor off-state, the switching function of phase i can be expressed as in (3.1) [3]:

$$Sw_i = \frac{1}{2} \cdot (S_{i+} - S_{i-}), \tag{3.1}$$

with the same transistor notation as in Figure 3.1. The switching function of 3.1 will hence return $\pm\frac{1}{2}$, based on the states of the transistors in the converter leg referred to the neutral point of the DC bus. With this reference, the voltage of phase i is given by Equation (3.2), [3]:

$$v_i = Sw_i \cdot v_{dc} \tag{3.2}$$

Using the negative terminal of the DC bus as reference, Sw_i will return either 1 or 0.

The complete AFE rectifier of interest in this thesis can be divided into three main parts: the DC bus, the inverter, and a passive output LC filter, as illustrated in Figure 3.2, adapted from [8].

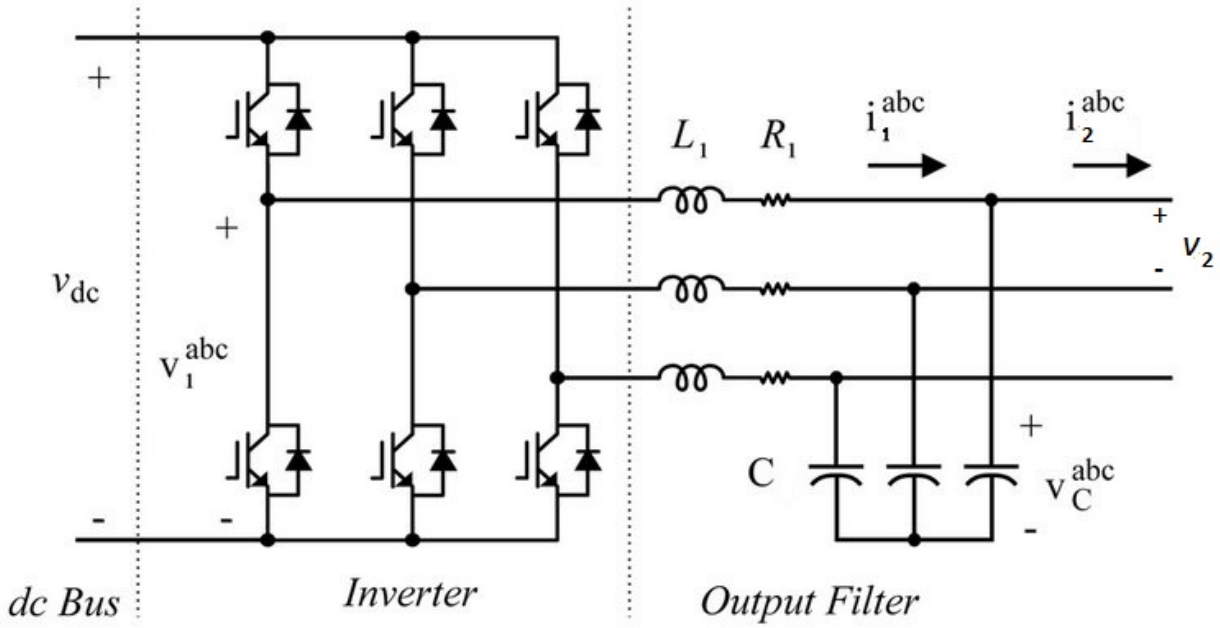

Figure 3.2: AFE rectifier model, adapted from [8].

Considering the parameters of Figure 3.2, and the switching function of (3.1), the following mathematical model can be derived for phase i, under the assumption of a balanced three phase system, and neglecting the resistance of the power switches [9]:

$$v_{dc}\left\{Sw_i - \frac{1}{3}\left(\sum_{i=a,b,c} Sw_i\right)\right\} = L_1\frac{di_{1,i}}{dt} + R_1 i_{1,i} + v_c + v_2 \tag{3.3}$$

The switching signals of the transistors are usually generated by means of a modulator, integrated in the converter control system.

Chapter 4

Active Front End Converter Control Theory

In this chapter, an overview of some of the possible control system implementations for AFE converters is given. Some of the different modulation strategies, sampling techniques, control signal reference frames, and current- and voltage controllers, described in literature, are presented. Discretization strategies for resonant controllers are reviewed, and controller optimization is briefly introduced.

4.1 Modulation Strategies for Three-Phase Two-Level Converters

This section presents some of the most commonly used modulation strategies for obtaining suitable switching signals for the transistor gates of a three-phase two-level converter.

4.1.1 Sinusoidal Pulse Width Modulation

The carrier-based sinusoidal pulse width modulation (PWM) strategy is one of the most basic and fundamental techniques for obtaining a three-phase output voltage of a converter. In this strategy, the transistor switching patterns are determined by comparing three sinusoidal reference signals, displaced 120 degrees in time to a single triangular carrier waveform, as illustrated in Figure 4.1.

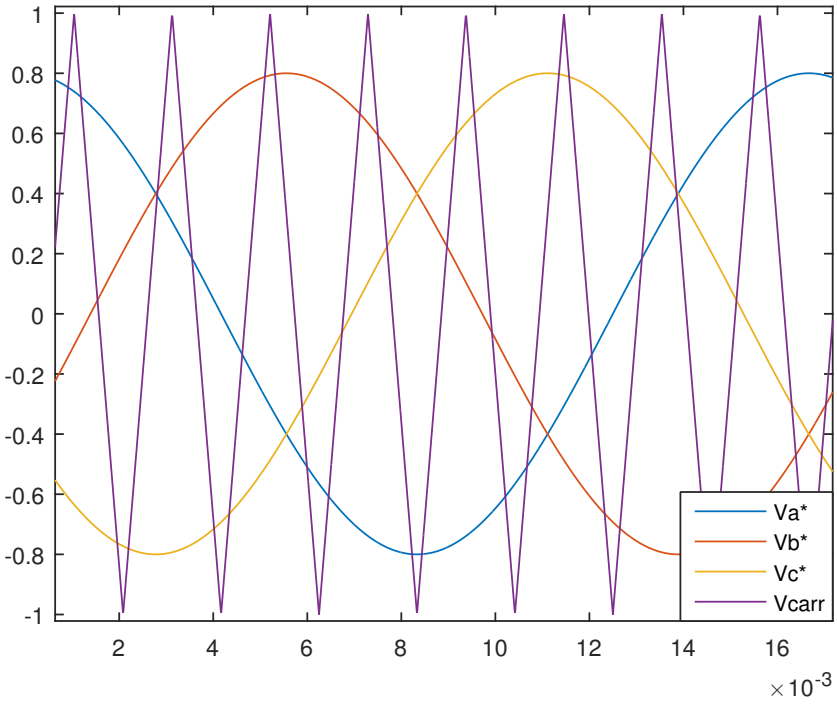

Figure 4.1: Phase voltage references and carrier signal of a sinusoidal PWM

Considering Figure 4.1, the switching patterns of the transistors in one of the converter legs are computed according to the following logic: Whenever the reference signal corresponding to the phase of interest is above the carrier signal, the uppermost transistor is in a conductive state, while the lower transistor remains open. When the reference signal is below the carrier wave, the switching states of the two transistors are interchanged. The switching frequency of the transistors is governed by the frequency of the carrier wave. Each of the reference voltages of Figure 4.1 correspond to one of the individual phases of the converter, and are given by the following equations [10]:

$$v_a^* = V_r \cos(\omega_n t), \tag{4.1}$$

$$v_b^* = V_r \cos(\omega_n t - 120^\circ), \tag{4.2}$$

$$v_c^* = V_r \cos(\omega_n t - 240^\circ), \tag{4.3}$$

where $\omega_n t$ is the voltage vector angle, and V_r is the amplitude of the reference voltage vector which can be expressed as shown below, using the modulation index, M_a, and the peak value of the carrier voltage, V_{carr}:

$$V_r = M_a V_{carr} \tag{4.4}$$

As long as the modulation index is kept within the interval, $0 < M_a \leq 1$, the modulator will remain inside its linear region, resulting in a sinusoidal output voltage and a linear relation between the reference voltage and the converter output voltage. Within this region, the relation between the output line-line RMS-voltage and the DC voltage is given by Equation (4.5) [11]:

$$V_{LL} = \frac{\sqrt{3}}{2\sqrt{2}} M_a V_{dc} \tag{4.5}$$

4.1.2 Sinusoidal Pulse Width Modulation with Third Harmonic Injection

Another common modulation strategy is that of the *third harmonic injection pulse width modulation* (THIPWM). The voltage references of the THIPWM are quite similar to those described in Section 4.1.1 for the sinusoidal PWM. The difference lies in the harmonic contribution that is added in all of the three equations of (4.6), (4.7), and (4.8), resulting in the following phase voltage references [10], [12]:

$$v_a^* = V_r(\cos(\omega_n t) + M_3 \cos(3\omega_n t)), \tag{4.6}$$

$$v_b^* = V_r(\cos(\omega_n t - 120^\circ) + M_3 \cos(3\omega_n t)), \tag{4.7}$$

$$v_c^* = V_r(\cos(\omega_n t - 240^\circ) + M_3 \cos(3\omega_n t)), \tag{4.8}$$

where M_3 is the modulation index of the third harmonic. Because the additional harmonic component is the same in all of the three phases, the resulting line voltages will be pure sinusoidal signals. The phase voltage references applied in the THIPWM are illustrated in Figure 4.2, along with their respective carrier signals.

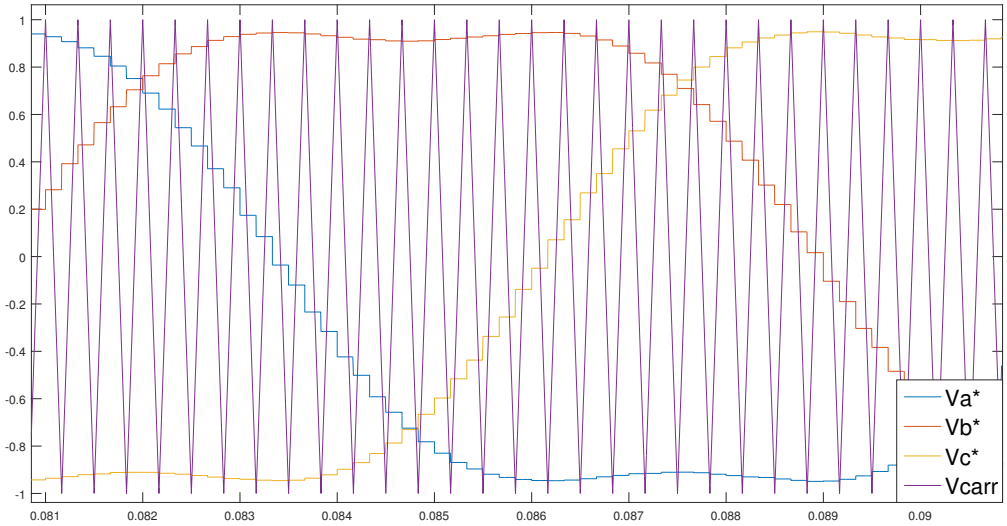

Figure 4.2: Simulation in Matlab displaying the phase voltage references of a sinusoidal THIPWM

It can be shown, that the reference signals generated by this PWM strategy are similar to those of another commonly used modulation technique, know as the *space vector pulse width modulation* (SVPWM). When compared to the pure sinusoidal PWM, the THIPWM and SVPWM both provide a better utilization of the DC link voltage. The third-harmonic injection in the leg voltage references leads to an increase in the linear modulation range. Injecting the third harmonic with an amplitude of one sixth of the fundamental harmonic, that is, $M_3 = \frac{1}{6}$, the maximum of the fundamental can be increased by a factor of 15.47 %, compared to pure sine-triangle carrier-based scheme [13]. Applying this factor in (4.5), the following relation is valid between the RMS line-voltage of the converter and the DC link voltage:

$$V_{LL} = \frac{V_{dc}}{\sqrt{2}} \tag{4.9}$$

Operation of the converter outside the linear region is possible and can be performed by increasing the modulation index further. This will, however, result in an increase of the harmonics in the converter output, requiring additional filtering.

This modulation strategy is the one utilized in the modulator implementation of the simulation model in Chapter 7.

4.2 Sampling

This section provides a brief summary of [14], describing three of the most common sampling techniques applied for carrier-based sinusoidal pulse width modulation strategies.

4.2.1 Natural Sampling

When natural sampling is applied, the reference signal is being continuously compared to the triangular carrier signal. Transistor switching operations are performed whenever the reference signal intersects the the carrier. Having a sinusoidal, or another time-varying reference signal, this sampling strategy results in an asymmetrical switching procedure, across the peak of the carrier signal.

4.2.2 Symmetrical Sampling

Using symmetrical sampling, the reference signal is sampled once per switching period of the carrier, and the reference is kept constant throughout. The sampling takes place, either at the peak or the bottom of the carrier, depending on the implementation. As a result, the switching signal is symmetrical compared to the top-bottom of the carrier, as apposed to the case of natural sampling.

4.2.3 Asymmetrical Sampling

When using asymmetrical sampling, the reference is sampled twice per carrier signal time period, thus, the sampling frequency is twice that of symmetrical sampling. The sampling occurs at rising and falling curves of the carrier, at time periods, $\frac{\pi}{2}$, and $-\frac{\pi}{2}$, of the waveform respectively. In the same way as for the natural sampling, this strategy results in an asymmetrical switching procedure across the peak of the carrier signal. This can be seen in Figure 4.3, extracted from a simulation in Matlab of a sinusoidal PWM with third harmonic injection, using asymmetrical sampling.

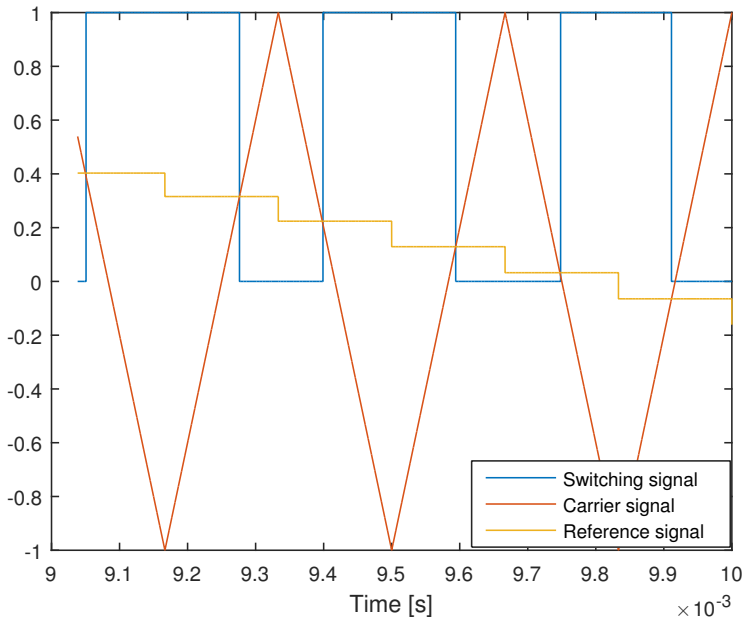

Figure 4.3: Simulation in Matlab of one phase of a THIPWM with asymmetrical sampling

This sampling strategy is the one utilized in the modulator implementation of the simulation model in Chapter 7.

4.3 Control Signal Reference Frames

Due to their similarities, the same methodology for control of adjustable speed drive systems and grid-connected converters, can be implemented. Three main possible reference frame models are described in literature, forming the basis of the control paradigm of these systems. These control structures include, the natural abc-reference frame, the stationary $\alpha\beta$-reference frame, and the synchronous dq-reference frame. An illustration of their orientations is given in Figure 4.4.

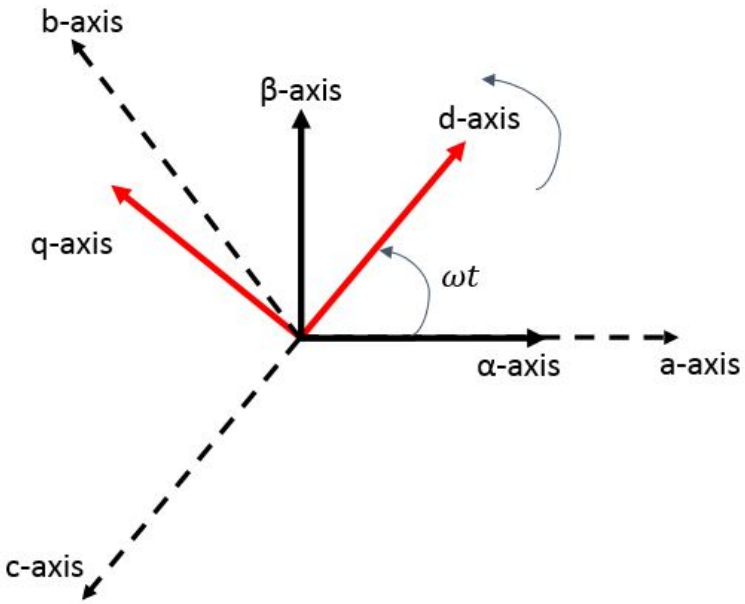

Figure 4.4: Orientation of the natural abc-reference frame, the stationary $\alpha\beta$-reference frame, and the synchronous dq-reference frame

The concept of these structures involves adaptation of the fundamental components of the three-phase system to the different reference frames throughout the system control loops. This is achieved by means of mathematical transformations. Even though the same control objectives can be reached, using the different reference frames, they all possess individual advantages and disadvantages when employed with their associated controllers. Some of these properties, along with the mathematical transformations related to these three reference frames will be elaborated throughout this section.

4.3.1 Natural abc-Reference Frame Control

Natural abc-reference frame control is the most basic and direct way of controlling a three-phase system. In this control structure, the phase signals are controlled individually and directly, using three controllers and without utilizing any type of system transformations.

4.3.2 Stationary $\alpha\beta$-Reference Frame Control

A three-phase system can be transformed into a two-phase orthogonal stationary system by means of the Clarke transformation [15]:

$$\begin{bmatrix} \alpha \\ \beta \\ \gamma \end{bmatrix} = \frac{2}{3} \begin{bmatrix} 1 & -\frac{1}{2} & -\frac{1}{2} \\ 0 & \frac{\sqrt{3}}{2} & -\frac{\sqrt{3}}{2} \\ \frac{1}{2} & \frac{1}{2} & \frac{1}{2} \end{bmatrix} \cdot \begin{bmatrix} a \\ b \\ c \end{bmatrix} \tag{4.10}$$

In a balanced three-phase system, the sum of the abc-currents is zero. Considering (4.10) of a balanced system, the contribution of the γ-phase is thus, zero, simplifying the transformation of (4.10) into the following two-phase transformation [16]:

$$\begin{bmatrix} I_\alpha \\ I_\beta \end{bmatrix} = \frac{2}{3} \begin{bmatrix} 1 & -\frac{1}{2} & -\frac{1}{2} \\ 0 & \frac{\sqrt{3}}{2} & -\frac{\sqrt{3}}{2} \end{bmatrix} \cdot \begin{bmatrix} I_a \\ I_b \\ I_c \end{bmatrix} \tag{4.11}$$

The mathematical transformations of (4.10) and (4.11) are also referred to as $\alpha\beta$-*transformations*, with the following inverse transformation from the $\alpha\beta$-reference frame and back to the natural abc-reference frame:

$$\begin{bmatrix} a \\ b \\ c \end{bmatrix} = \begin{bmatrix} 1 & 0 & 1 \\ -\frac{1}{2} & \frac{\sqrt{3}}{2} & 1 \\ -\frac{1}{2} & -\frac{\sqrt{3}}{2} & 1 \end{bmatrix} \cdot \begin{bmatrix} \alpha \\ \beta \\ \gamma \end{bmatrix} \tag{4.12}$$

The most prominent advantage of utilizing the $\alpha\beta$-transformation, compared to the natural abc-natural reference frame, is that the reduction of one phase-variable implies the same reduction in the number of controllers required, and, hence, effectively reduces the computational power demand of the digital signal processors or micro-controllers [17]. Since the $\alpha\beta$-reference frame is a stationary one, whilst the grid-signals are sinusoidal, the control signals of this control structure will be sinusoidal.

The stationary $\alpha\beta$-reference frame is the one considered for controller implementation and simulation in Chapter 7.

4.3.3 Synchronous dq-Reference Frame Control

The *Park transformation*, also referred to as the *dq-transformation*, transforms a stationary system to a rotating orthogonal system, synchronizing it with some system quantity. The transformation to the dq-reference frame from the stationary $\alpha\beta$-frame of 4.3.2, can be performed as indicated in (4.13) [18],

$$\begin{bmatrix} d \\ q \\ 0 \end{bmatrix} = \begin{bmatrix} \cos(\omega t) & \sin(\omega t) & 0 \\ -\sin(\omega t) & \cos(\omega t) & 0 \\ 0 & 0 & 1 \end{bmatrix} \cdot \begin{bmatrix} \alpha \\ \beta \\ \gamma \end{bmatrix} \tag{4.13}$$

with the corresponding inverse transform of (4.14):

$$\begin{bmatrix} \alpha \\ \beta \\ \gamma \end{bmatrix} = \begin{bmatrix} \cos(\omega t) & -\sin(\omega t) & 0 \\ \sin(\omega t) & \cos(\omega t) & 0 \\ 1 & 1 & 1 \end{bmatrix} \cdot \begin{bmatrix} d \\ q \\ 0 \end{bmatrix} \tag{4.14}$$

Park transformation to the synchronous reference frame can also be performed directly from the natural abc-reference frame, using the transformation of (4.15) [19],

$$\begin{bmatrix} d \\ q \\ 0 \end{bmatrix} = \frac{2}{3} \begin{bmatrix} \cos(\omega t) & \cos(\omega t - 120°) & \cos(\omega t + 120°) \\ -\sin(\omega t) & -\sin(\omega t - 120°) & -\sin(\omega t + 120°) \\ \frac{1}{2} & \frac{1}{2} & \frac{1}{2} \end{bmatrix} \cdot \begin{bmatrix} a \\ b \\ c \end{bmatrix}, \tag{4.15}$$

with the inverse transform as indicated in Equation (4.16).

$$\begin{bmatrix} a \\ b \\ c \end{bmatrix} = \begin{bmatrix} \cos(\omega t) & -\sin(\omega t) & 1 \\ \cos(\omega t - 120°) & -\sin(\omega t - 120°) & 1 \\ \cos(\omega t + 120°) & -\sin(\omega t + 120°) & 1 \end{bmatrix} \cdot \begin{bmatrix} d \\ q \\ 0 \end{bmatrix} \tag{4.16}$$

The dq-reference frame can be utilized through the concept of, *synchronous reference frame* (SRF) *control*, in which the dq-axis of Figure 4.4 are synchronized with the grid-frequency. As a result, the steady-state control variables of fundamental frequency of the SRF controllers will be DC values, as apposed to the sinusoidal quantities of the stationary reference frame-based

control systems. This is an important feature of the SRF control, since most stationary reference frame linear controllers will introduce significant stationary phase errors at fundamental, and at harmonic frequencies, when tracking AC components [20].

4.4 Controllers

In the control structure of an AFE converter, several controllers are in operation for ensuring suitable control of the system currents, voltages, active and reactive power, for maintaining satisfactory reference tracking, disturbance rejection, and more. This section provides a review of the functionalities, properties, and block diagrams related to the individual controllers treated in this thesis. The operation of these controllers are based on feedback control, as depicted below in Figure 4.5, and described in Appendix B, in which the input reference signal is compared to the measured output signal. This difference between these quantities corresponds to the error signal, $e(s)$, which is manipulated in the controller with the intention of making the output signal track the reference, thus, forcing the error to zero.

4.4.1 Proportional Controllers

The *proportional* (P) controller is the most basic type of controller. It consists of a simple proportional gain, K_p, adjusting the system band-width, without affecting its phase response [21]. A block diagram illustrating a feedback control loop employing a proportional controller is given in Figure 4.5.

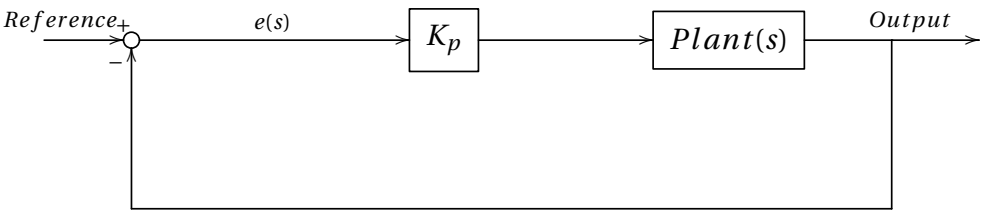

Figure 4.5: Block diagram in the frequency domain displaying a P controller in a generic feedback control loop

4.4.2 Proportional Integral Controllers

Linear *proportional integral* (PI) controllers is a well established controller applied in the industry for reference tracking systems. Its ideal transfer function can in the frequency domain be expressed as in (4.17) [21]:

$$PI(s) = K_p \cdot \frac{1 + T_i s}{T_i s} \tag{4.17}$$

Its operation is depicted below in the block diagram of Figure 4.6.

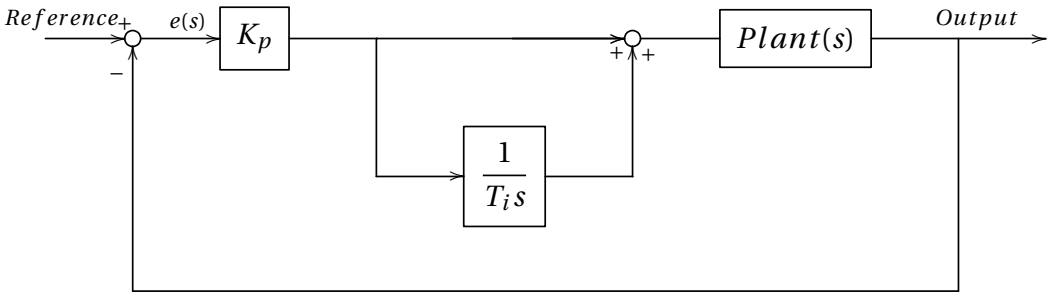

Figure 4.6: Block diagram in the frequency domain displaying an ideal PI controller in a generic feedback control loop

The proportional gain of the controller acts as an adjustable amplifier without affecting the phase of the control loop, while the intention of the integral part is to ensure an infinite gain at the zero-frequency, and perfect reference-tracking. Moreover, this controller provides a negative contribution to the phase of the control loop at low frequencies. Traditionally, proportional-integral controllers have been combined with a grid-voltage feed-forward for controlling the current and voltage of grid-connected inverters. This control scheme is well suited for controlling DC signals, but steady-state amplitude- and phase errors are introduced whenever a PI controller is used for tracking of a sinusoidal reference signal. This error may be mitigated by increasing the controller gain, but this is likely to compromise the system stability due to noise amplification. In an AFE converter control system, the controller gain, K_p, will be limited by the non-damped passive filter at the converter output. Another drawback with this conventional

PI controller solution is its inability to eliminate distortion. Moreover, the use of grid-voltage feed-forward introduces grid-voltage background harmonics in the current waveform, which may result in a poor THD performance of the current [22].

4.4.3 Proportional Integral Derivative Controllers

In many ways, the linear *proportional integral derivative* (PID) controller is similar to that of the PI controller, both in terms of its regulation properties, its applications, as well as its limitations. Some different expressions exist for the ideal transfer function of a PID controller. The *parallel form* PID controller is given in (4.18) [21]:

$$PID(s) = K_c(1 + \frac{1}{T_i s} + T_d s) \tag{4.18}$$

Another possible implementation of the PID controller, is the proportional integral derivative controller with limited derivative action, of (4.19) [21].

$$PID(s) = K_p \frac{(1 + T_i s)(1 + T_d s)}{T_i s(1 + \alpha T_d s)}, \quad \alpha < 1 \tag{4.19}$$

As for the PI controller, the PID controller is used in feedback control to reduce the error signal between the reference and measured output signal, with the operation of an ideal PID controller illustrated in Figure 4.8.

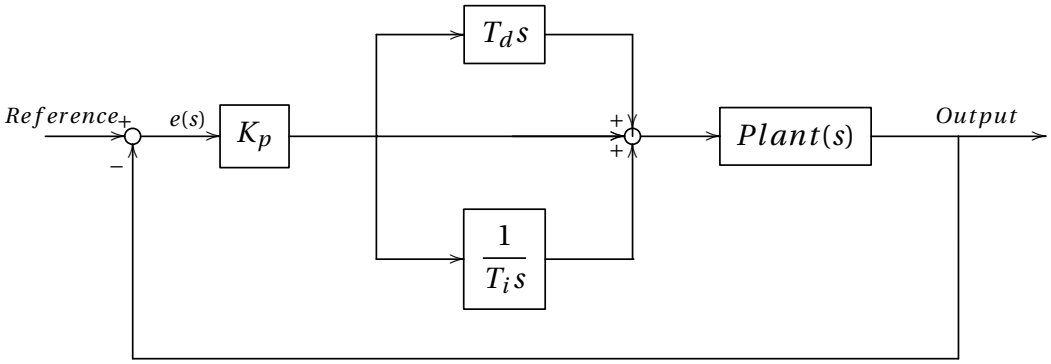

Figure 4.7: Block diagram in the frequency domain displaying an ideal parallel type PID controller in a generic feedback control loop

The derivative term of the PID controller provides a lift of the phase of the control loop at higher frequencies, yielding a higher bandwidth, and, thus, quicker regulation response. Moreover, it contains all the regulation properties that is usually desired, and its three control parameters can be adjusted in a wide range, making it adaptable for several types of systems. For many systems, a PID controller can ensure low stationary deviation. However, when applied in a converter control systems, the PID controller shares the same limitations as those of the PI controller described in Section 4.4.2, the most prominent one, being its inability to ensure perfect tracking of sinusoidal references when implemented in a stationary reference frame [23]. **The implementation of the PID controller with limited derivative action is applied in many practical systems and is also the one implemented in the simulation model of Chapter 7 in this thesis.**

4.4.4 Resonant Controllers

Another possible solution for current and voltage control for grid-tied inverters are the utilization of resonant controllers, also referred to as a *generalized integrators*, that is, an integrator for a sinusoidal signal. In the s-domain, the transfer function of this controller can be expressed as in (4.20) [24]:

$$R(s) = \frac{s}{s^2 + \omega_0^2}, \tag{4.20}$$

with ω_0 being the nominal grid-angular velocity,

$$\omega_0 = 2\pi f_0 \tag{4.21}$$

Due to the inherent shortcomings of PI- and PID controllers in removing the steady-state error of sinusoidal reference signals, resonant controllers have in literature in recent years been put forward as a promising solution for control of AC signals in the stationary reference frame. The most conventional implementation of this type of controller is the *proportional resonant* (PR) controller [25]. In general, PR and PI controller are quite similar, their main difference being the way in which the integration action takes place. In the frequency domain the PR controller, $PR(s)$, can be expressed as in (4.22) [25]:

$$PR(s) = K_P + K_I \frac{s}{s^2 + h^2{\omega_0}^2}, \tag{4.22}$$

its block diagram depicted in Figure 4.8.

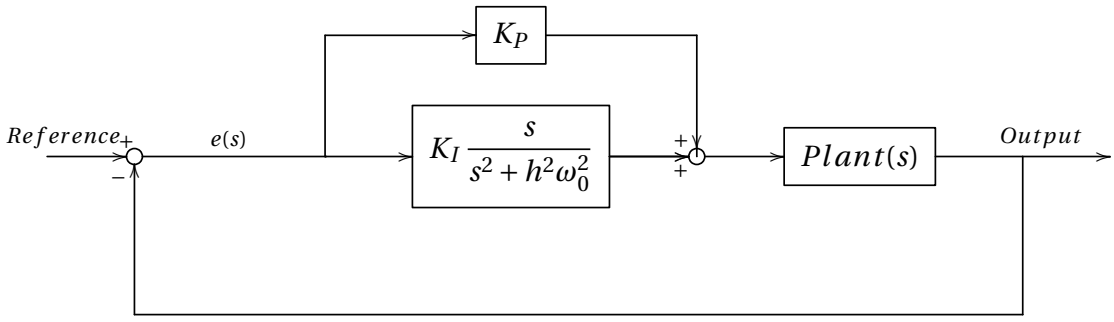

Figure 4.8: Block diagram in the frequency domain displaying an ideal PR controller in a generic feedback control loop

In theory, $PR(s)$ ensures an infinite gain at the resonance frequency, $h\omega_0$, in an open loop system, which corresponds to perfect tracking of systems oscillating at this frequency when implemented in a closed loop system. This property can be utilized by tuning the generalized integrator to the desired reference frequency. Thus, allowing the resonant controller to resonate at the grid-frequency, leads to a removal of the steady-state errors related to the PI- and PID con-

trollers, also when implemented in a stationary reference frame. Perfect reference-tracking can also take place without compromising signal noise and system stability, due to the low bandwidth of the band-pass filter of the generalized integrator [26]. Moreover, lower complexity and computational resources are required due to the lack of Park transformations. A drawback with resonance controllers is their parameter sensitivity, making them prone to tuning and design errors, as well as control variable and system parameter modifications [27].

Multiple generalized integrators can also be embedded in a single controller, employing *resonant harmonic compensation* (RHC). In addition to the resonant controller tracking the fundamental component of the grid, an additional number of generalized integrators can be added, either in series or in parallel, tracking the harmonic components of interest, thus forming a *multiple-resonant controller*. The transfer function of such a controller, designed to attenuate the third, fifth and seventh harmonic components, is given in (4.23) [25], [29]:

$$RHC(s) = \sum_{h=3,5,7} K_{Ih} \frac{s}{s^2 + {\omega_0}^2 h^2}. \tag{4.23}$$

In (4.23), the individual resonant harmonic terms work as band-pass filters tuned to resonate at the desired frequencies.

Resonant-type controllers are not only limited to be combined with proportional type controllers. They can also be combined with other types of controllers, forming the likes of *PIR* controllers, and more [28].

4.5 Discretization

Whenever a physical digital system is to be measured and controlled, sampling time is introduced, and a digital controller implementation is necessary. If system models and controllers already are designed in the continuous time or frequency domain, a discretization of the models can be performed for transformation to the discrete z-domain. In literature, several different discretization strategies are given, with different considerations that should be made, regarding sampling time, tracking, modification of pole-placement, computational load, time delay, and more. In general, when a z-transformation of a system is performed, it changes the distribution of the zeros and poles of the continuous transfer function, thus modifying the system proper-

ties, including its stability. Various types of delay compensation strategies can be implemented for mitigating the effects of the computational delay and compensating for the system modifications [29]. The concept of discretization has been, and still is, the scope of many research projects, with the aim of developing better and more accurate digital controller representations [24], [30]. Next, some of these techniques are studied for digital implementation of a resonant type controller.

4.5.1 Digital Implementation of Resonant Controllers

This section provides some of the alternatives introduced in literature for digital implementation of resonant controllers, in order to select a suitable implementation to be applied in this thesis.

An essential step in the digital implementation of any controller is the discretization process. Due to their infinite gains and narrow bands, resonance controllers are especially sensitive to this process. Even a slight deviation of the resonance poles may cause a loss of the entire resonance effect of the controller. Therefore, it is of great importance to study the various alternatives for the discrete-time implementations of these controllers. This section will consider an implementation of a resonant controller based on two interconnected integrators which is a solution widely employed for achieving frequency adaptation with low resource consumption [30], [31]. Its block diagram is indicated in Figure 4.9, with the parameter, ω_0 appearing as a separate gain that can be adjusted in real time according to the estimated grid-frequency.

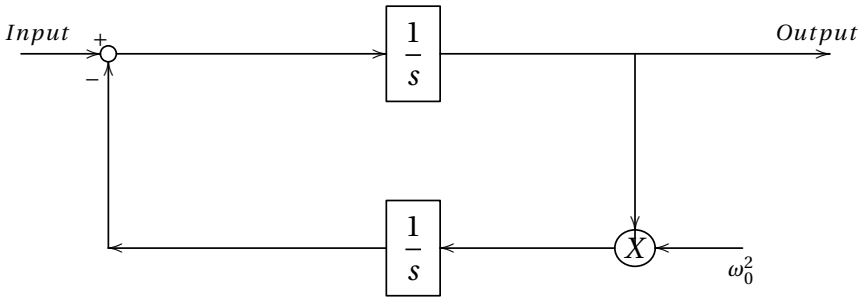

Figure 4.9: Block diagram in the continuous s-domain of a frequency adaptive resonant controller based on two integrators

The discrete-time implementation of these controllers is likely to cause system inaccuracies that can be evaluated according to the following criterion:

1. Modification of resonant poles

2. Modification of zeros: change of system delay

3. Computational burden

The first and most important criteria to consider, is the modification of the resonant poles. Even a small deviation of the resonance frequency may introduce a large error in steady-state when tracking an AC reference. Moreover, the distribution of zeros may be modified in the discretization process, thus changing the system delay as well as the controller gains at frequencies other than the resonance frequency. In any digital implementation of a resonant controller, it should also be taken into account, that as the resonance frequency and sampling time increase, the introduced system delay will affect the performance and, may as well lead to instability. In a converter control system, this delay is mainly due to computation delay, modulation, and the time constant of the passive filter. In order to compensate for this delay, a phase lead, ϕ_h, should be introduced in the vicinity of the resonant frequency of the controller. In this manner, the phase gain parameter can be defined as the difference between the actual phase provided by a resonant controller at frequencies infinitely close to a resonance frequency, $h\omega_0$, and the one

provided by the continuous closed loop controller model [30]. If the phase error is not compensated for, the stability margins will be compromised and anomalous peaks will appear in the closed-loop frequency response. It should be remarked, that a suitable phase lead introduced in the continuous domain may not be adequate in the corresponding digital controller implementation [36].

When selecting the discretization scheme of the controller, there will also be a trade-off between the accuracy of the transformation, and the computational burden of the implementation.

The three aforementioned criterion should all be considered when selecting the discretization method. In Table 4.1, various discretization methods are presented for a continuous two integrator resonant controller, $R(s)$, as in (4.20) [31].

Table 4.1: Discretization Methods For R(s), Adapted From [31]

Discretization method	**Equivalence**	**Notation**
Zero-order hold	$X(z) = (1-z^{-1})Z\{\mathcal{L}^{-1}\{\frac{X(s)}{s}\}\}$	$R_{zoh}(z)$
First-order hold	$X(z) = \frac{(z-1)^2}{zT_s}Z\{\mathcal{L}^{-1}\{\frac{X(s)}{s^2}\}\}$	$R_{foh}(z)$
Forward Euler	$s = \frac{z-1}{T_s}$	$R_f(z)$
Backward Euler	$s = \frac{z-1}{zT_s}$	$R_b(z)$
Trapezoid (Tustin)	$s = \frac{2}{T_s}\frac{z-1}{z+1}$	$R_t(z)$
Tustin with pre-warping	$s = \frac{\omega_0}{\tan(\frac{\omega_0 T_s}{2})}\frac{z-1}{z+1}$	$R_{tp}(z)$
Zero-pole matching	$z = e^{sT_s}$	$R_{zpm}(z)$
Impulse invariant	$X(z) = Z\{\mathcal{L}^{-1}\{\{X(s)\}\}$	$R_{imp}(z)$

The corresponding z-domain representations, $R(z)$, of Table 4.1 are given in Table 4.2 [31].

Table 4.2: Z-Domain Transfer Functions Obtained By Discretizing $R(s)$ With Different Methods, Adapted From [31]

Discretized *R(s)* with different methods
$R_{zoh}(z) = \frac{\sin(\omega_0 T_s)}{\omega_0} \frac{z^{-1}-z^{-2}}{1-2z^{-1}\cos(\omega_0 T_s)+z^{-2}}$
$R_{foh}(z) = \frac{1-\cos(\omega_0 T_s)}{\omega_0^2 T_s} \frac{1-z^{-2}}{1-2z^{-1}\cos(\omega_0 T_s)+z^{-2}}$
$R_f(z) = T_s \frac{z^{-1}-z^{-2}}{1-2z^{-1}+z^{-2}(\omega_0^2 T_s^2+1)}$
$R_b(z) = T_s \frac{1-z^{-1}}{(\omega_0^2 T_s^2+1)-2z^{-1}+z^{-2}}$
$R_t(z) = 2T_s \frac{1-z^{-2}}{(\omega_0^2 T_s^2+4)+z^{-1}(2\omega_0^2 T_s^2-8)+z^{-2}(\omega_0^2 T_s^2+4)}$
$R_{tp}(z) = \frac{\sin(\omega_0 T_s)}{2\omega_0} \frac{1-z^{-2}}{1-2z^{-1}\cos(\omega_0 T_s)+z^{-2}}$
$R_{zpm}(z) = K_d \frac{z^{-1}-z^{-2}}{1-2z^{-1}\cos(\omega_0 T_s)+z^{-2}}$
$R_{imp}(z) = T_s \frac{1-z^{-1}\cos(\omega_0 T_s)}{1-2z^{-1}\cos(\omega_0 T_s)+z^{-2}}$

Correction of Zeros

In [31], the phase lead is introduced in the resonant term of a controller tracking the h-th order harmonic, resulting in the following controller transfer function in the s-domain:

$$R_h^d(s) = \frac{s\cos(\phi_h^*) - h\omega_0 \sin(\phi_h^*)}{s^2 + h^2\omega_0^2}, \tag{4.24}$$

with ϕ_h^* being the target lead angle, that is, the desired value of the target angle, ϕ. The discretization process, however, modifies the system zeros, causing the target lead angle to change, resulting in a case where $\phi \neq \phi_h^*$. A proposed value for the target leading angle of a VSC model with a series LR filter for correcting the phase error, is given in (4.25) [30]:

$$\phi_h^* = \frac{\pi}{2} + \frac{3}{2} h\omega_0 T_s \tag{4.25}$$

Moreover, an accurate phase lead ($\phi = \phi_h^*$), can be ensured for a resonant controller in the z-domain, applying the impulse invariant method of Table 4.1 on (4.24), which yields the following transfer function for a two integrator implementation, given in Equation (4.26), adapted from [30]:

$$R_h^{id}(z) = T_s \frac{\cos(\phi_h^*) - z^{-1}\cos(\phi_h^* - h\omega_0 T_s)}{1 - 2z^{-1}\cos(h\omega_0 T_s) + z^{-1}} \tag{4.26}$$

Still assuring, ($\phi = \phi_h^*$), (4.26) can be modified according to [30], yielding:

$$R_h^{idm}(z) = T_s \frac{z^{-1}\cos(h\omega_0 T_s \phi_h^*) - z^{-2}\cos(\phi_h^*)}{1 - 2z^{-1}\cos(h\omega_0 T_s) + z^{-2}} \tag{4.27}$$

Correction of Poles

In order to obtain perfect tracking, a correct placement of the resonant poles is necessary. In accordance to the infinite gain, their position should be on the unit circumference, which corresponds to a zero damping factor. The complex conjugated poles should, by this argument, be placed at, $e^{jh\omega_0 T_s}$ and $e^{-jh\omega_0 T_s}$, with the product of these terms corresponding to the following denominator of the z-domain resonant controller transfer function: $1 - 2z^{-1}\cos(h\omega_0 T_s) + z^{-2}$ [31]. This expression is obtained, using the following discretization methods of Table 4.2: $R_{zoh}(z)$, $R_{foh}(z)$, $R_{tp}(z)$, $R_{zpm}(z)$, and $R_{imp}(z)$, as well as in the discrete-time resonant controller implementation of (4.27). These implementations should, thus, provide accurate placement of the discrete resonant poles. However, these implementations rely on explicit online calculations of trigonometric functions, implying a greater resource consumption. A way of reducing this computational burden is by means of the following Taylor series approximation for a controller tracking a general harmonic, h [30]:

$$h^2\omega_0^2 \rightarrow C_h = 2\sum_{n=1}^{k/2} \frac{(-1)^{n+1} h^{2n} \omega_0^{2n} T_s^{2n-2}}{(2n)!}, \tag{4.28}$$

in which the order of expansion, k, is an even number. According to the study of [30], a fourth order expansion provides a good accuracy of the resonant poles for a wide range of the harmonic spectrum. Applying (4.28) in the denominator of (4.27), results in the following discrete-time implementation of a resonant controller, employing correction of poles and zeros, both, as well

as the reduced computational burden, following Equation (4.28):

$$R_h^{icd}(z) = T_s \frac{z^{-1}\cos(h\omega_0 T_s + \phi_h^*) - z^{-2}\cos(\phi_h^*)}{1 - 2z^{-1}(1 - C_h\frac{T_s^2}{2}) + z^{-2}} \tag{4.29}$$

The block diagram representation of this controller is depicted in Figure 4.10, adapted from [30].

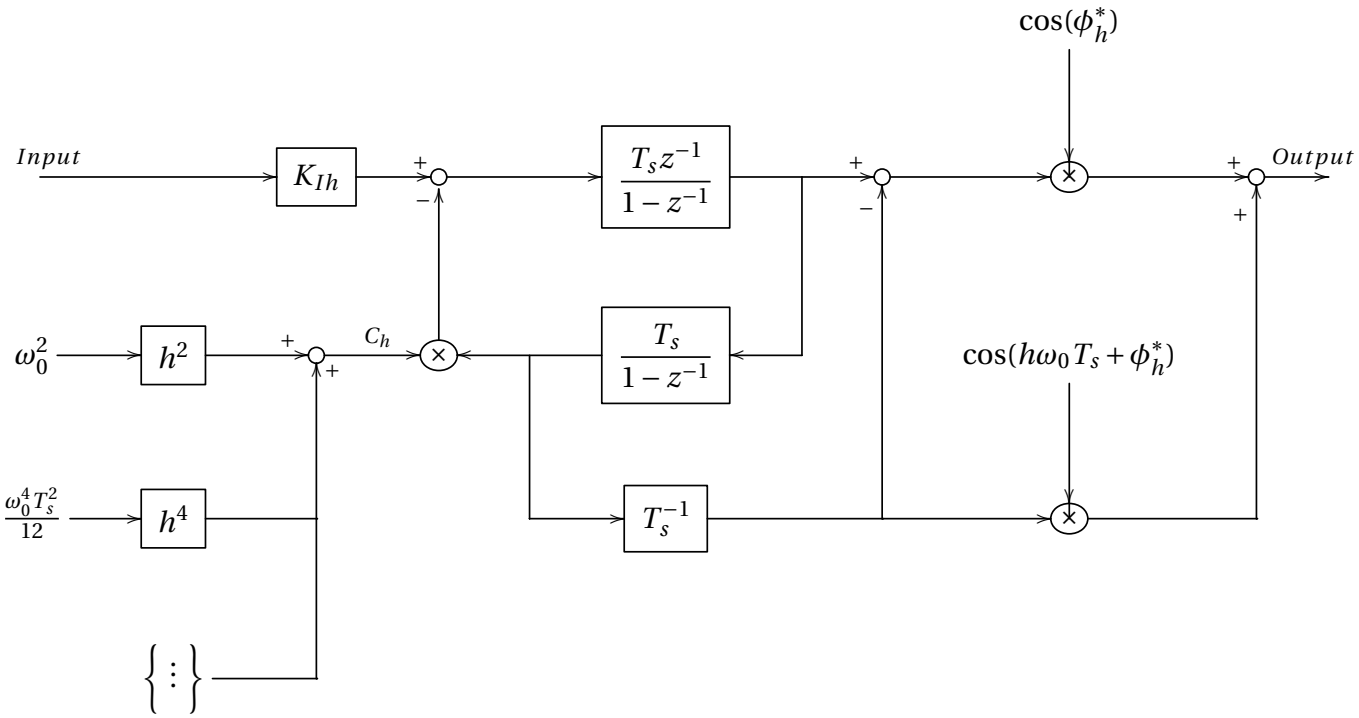

Figure 4.10: Block diagram of discrete-time implementation of a double integrator resonant controller, employing correction of poles and zeros, as well as reduced computational burden, adapted from [30]

The resonant controller above, based on the impulse-invariant discretization method should maintain resonance frequency and poles at the design locations, as well as ensuring a low computational burden, thus, yielding a satisfactory performance in accordance with the three given criterion [24], [30], [31].

4.6 Controller Optimization

Controller design is the procedure in which a certain methodology is applied for tuning of the controller parameters. The controller performance can be measured by considering several different criterion, such as stability, reference tracking, and rejection of measurement noise. Some of these properties may be in conflict with each other, while others are irrelevant for the system of interest. Therefore, the process of control optimization is highly dependent on the system to be controlled, and will, thus involve a trade-off, where the most important control objectives should be emphasized.

Several strategies are presented in the literature for tuning of controllers, two of these, namely, the *modulus optimum* (MO) and the *symmetrical optimum* (SO) methods [32], are briefly introduced here.

4.6.1 Modulus Optimum

The modulus optimum criteria is often used for analytic design of PI and PID controllers with low order plant transfer function due to its simplicity and rapid response [33]. Its objective is to maximize the frequency range in which the modulus (absolute value) of the closed loop system equals unity, or 0 dB, that is, perfect closed-loop tracking is achieved. When the system to be controlled has one minor and one dominant pole, the integral time constant of the PI or PID controller is selected as to cancel out the dominant pole [34].

4.6.2 Symmetrical Optimum

The aim of the symmetrical optimum tuning methodology is to maximize the phase margin of the resulting closed loop system of interest at a given frequency. Usually, an additional tuning parameter is introduced as a part of this procedure for effective selection of the closed-loop system damping factor. The domain of this parameter should be chosen as to provide a reasonable trade-off between performance and the minimum value of the desired phase margin. The resulting controller should ensure good delay tolerance, which is important for system with large time delays, as well as good disturbance rejection capability [35]. Moreover, the SO tuning strategy can, as apposed to MO, be applied for systems containing pure integrators because it does

not rely on pole cancellation.

Cosidering different references, quantitative examples of the SO tuning strategy is given in Chapter 6, where it is applied for design of inner PI and PID current controllers.

4.7 Summary of Chapter

In this chapter, an overview of some of the possible control system implementations for AFE converters has been given. Some of the different modulation strategies, sampling techniques, control signal reference frames, and current- and voltage controllers, described in literature, were presented. Discretization strategies for resonant controllers have been reviewed, and controller optimization was briefly introduced.

Chapter 5

Switching Harmonics and Design of LC Filter

This chapter deals with harmonic distortion, one of the most important characteristics of the AFE converter regarding power quality. A brief summary is given on some of the most important standards for grid-connected converters, and a theoretical background study is presented on the full-bridge diode rectifier, and on LC filter design.

5.1 Switching Harmonics

Harmonic signals are waveforms with a frequency that is a positive integer multiple of the fundamental frequency. A measure of the level of harmonic distortion is the *total harmonic distortion* (THD), which for a general signal, y is given by the following definition [37]:

$$THD_y = \frac{\sqrt{\sum_{n=1}^{\infty} y_n^2}}{y_1}, \tag{5.1}$$

in which y_n represents the distorted signal in its complete form, while y_1 is the signal fundamental component.

Linear loads draw sinusoidal currents and voltages close to unity power factor. When a *nonlinear* load, on the other hand, is supplied by a sinusoidal voltage, a non-sinusoidal, distorted current is drawn from the utility, containing harmonics. Being nonlinear devices, the switching

operations of power electronic converters, thus, give rise to switching type harmonic signals. The resulting harmonic currents, flowing through the system, cause voltage distortions at the *point of common coupling* (PCC), that is, the common connection point between the local loads and the utility. The distorted voltage is distributed to the loads further downstream, where they can cause power quality issues. Some of the problems related to harmonics are [38]:

- Overheating of equipment such as transformers and wires
- Malfunctioning of relays
- Incorrect meter readings
- Increased utility current requirement
- Increased eddy current losses in transformer lamination
- Interference in communication systems
- Tripping of sensitive equipment

For quantification of the harmonic power, (H), the term, *total harmonic power* (A) can be introduced in addition to the *apparent power* (S), given by the relations,

$$S = \sqrt{P^2 + Q^2}, \tag{5.2}$$

and,

$$A = \sqrt{S^2 + H^2}, \tag{5.3}$$

respectively. The relation of the individual power phasors are illustrated in the power cube of Figure 5.1, adapted from [39].

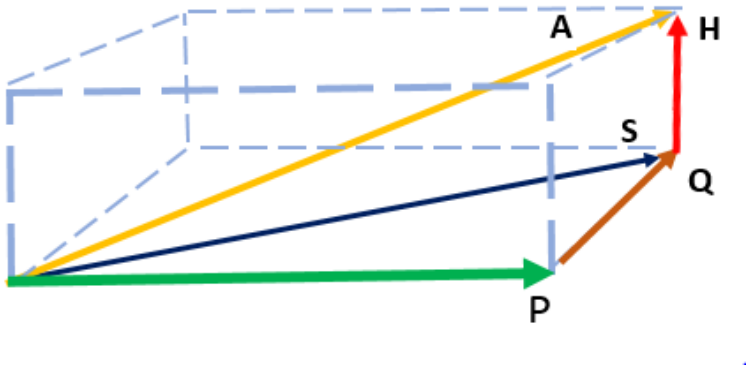

Figure 5.1: Power cube illustrating the relation between the harmonic power (H) and apparent power (S), adapted from [39]

The green, brown and dark blue arrow represent the active, reactive and apparent power, respectively. These phasors are located in the bottom horizontal plane of the power box, representing the fundamental frequency. Whereas, the red and yellow phasors of the harmonic and total harmonic power are displaced vertically, above the plane of the fundamental frequency. In order to limit the extent of harmonics in the electrical grid, standards and regulations have been developed including performance criteria for the harmonic content of non-linear loads.

5.2 Standards for Harmonic Limits

This section briefly presents the IEEE std. 519, which was introduced for providing directions and limits on harmonics caused by the operation of static power converters and other non-linear loads.

5.2.1 IEEE Standard 519 Voltage Harmonic Limits

The voltage harmonic limits of IEEE std. 519 applied at the PCC are summarized in Table 5.1, adapted from [42], with limits depending on the system classification of interest.

Table 5.1: Voltage System Classification And Distortion Limits THD[%] Of IEEE Standard 519, Tables 10.2 And 11.1, Adapted From [42]

System nominal voltage	Special application[1]	General system	Dedicated system[2]
120-600 V	3.0	5.0	10.0
69 kV and below	-	5.0	-
69 kV to 161 kV	-	2.5	-
161 kV and above	-	1.5	-

[1] Special applications include hospitals and airports
[2] A dedicated system is exclusively dedicated to the converter load

The values of Table 5.1 represent worst-case operating conditions. Therefore, higher distortion limits can be tolerated for short amounts of time, for instance at application start-up. Considering an AFE converter, the "69 kV and below"-row, indicating a voltage distortion limit of 5% is the one of interest since the nominal voltage of these systems seldom reaches more than a few kilo volts. In general, special applications such as computer equipment at hospitals and airports are more critical and sensitive to harmonics, and demand stricter regulations, rather than general and dedicated systems. It should be noted, that even though the limits of Table 5.1 are met at the PCC, the voltage harmonic distortion will always be higher downstream where the system impedance is at its highest, and the harmonic currents causing the voltage harmonics are generated [43].

5.2.2 IEEE Standard 519 Current Harmonic Limits

The current harmonic limits of IEEE std. 519 for power systems with voltage levels between 120 V and 69 kV are shown in Table 5.2. It provides both total demand distortion (TDD) currents limits as well as individual harmonic current limits. These limits are defined, using the short-circuit ratio, I_{sc}/I_L, in which, I_{sc} is the maximum short-circuit current at PCC, while I_L corresponds to the maximum demand load current (fundamental frequency) at the PCC. In general, voltage distortion is more likely to develop from current harmonics consumed at a point of common coupling of a higher impedance system with a low short-circuit ratio. For this reason, the harmonic limits are increasingly stricter with decreasing system short-circuit ratio.

Table 5.2: Current Distortion Limits For General Distribution Systems, From IEEE Std. 519, [42]

$\mathbf{I_{sc}/I_L}$	**h<11**	**11 ≤ h < 17**	**17 ≤ h < 23**	**23 ≤ h < 35**	**35 ≤ h**	**TDD**[%]
<20	4.0	2.0	1.5	0.6	0.3	5.0
20<50	7.0	3.5	2.5	1.0	0.5	8.0
50<100	10.0	4.5	4.0	1.5	0.7	12.0
100<1000	12.0	5.5	5.0	2.0	1.0	15.0
>1000	15.0	7.0	6.0	2.5	1.4	20.0

h - Individual harmonic current limit, I_{sc} - Maximum short-circuit current at PCC, I_L - Maximum demand load current (fundamental frequency) at PCC, TDD - Total demand distortion

There are several types of non-linear loads that can cause harmonics, one of these being diode rectifiers.

5.3 Six-Pulse Full-Bridge Diode Rectifier

The three-phase, six-pulse, full-bridge diode rectifier, shown in Figure 5.2 is a commonly used circuit arrangement for rectification of three-phase AC voltages. A filter capacitor, C_b and an ideal current source, I_{dc} is connected to the DC side of the rectifier.

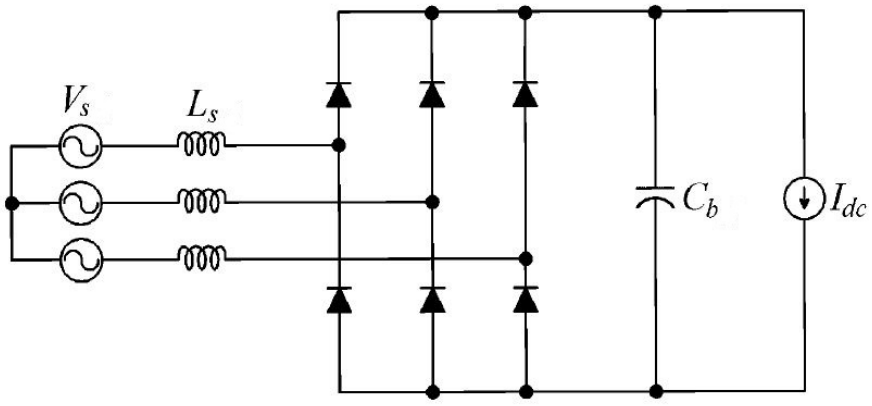

Figure 5.2: Three-phase six-pulse full-bridge diode rectifier connected to an ideal current source, adapted from [40]

Assuming ideal conditions and neglecting the source inductance ($L_s = 0$), the line current, i_s, the voltage, v_s and the fundamental current component, i_{s1}, of the rectifier bridge will be, as depicted in Figure 5.3.

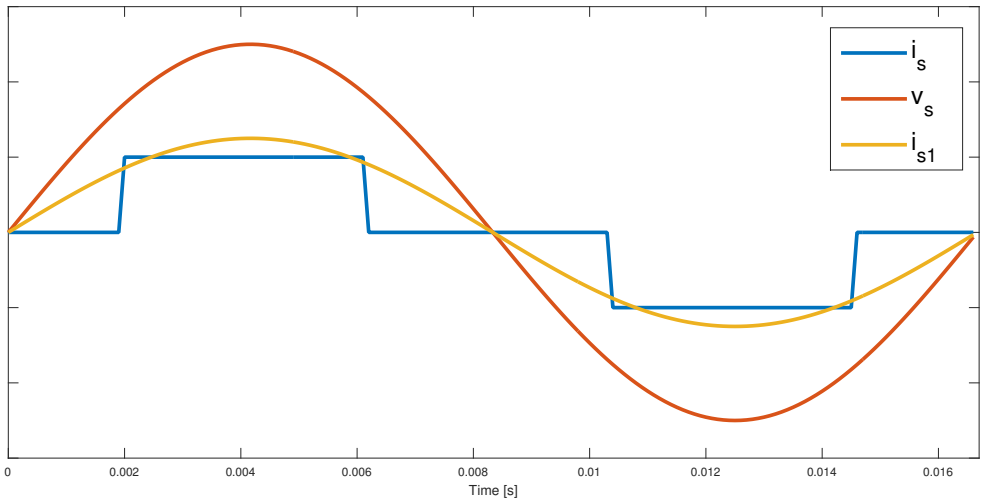

Figure 5.3: Line current in a three-phase rectifier with Ls = 0 and constant DC current

In this ideal configuration, it can be proved, that the individual rectifier harmonic components, I_{sh}, can be expressed in terms of the fundamental-frequency component according to (5.4), [41]:

$$I_{sh} = \frac{I_{s1}}{h} \tag{5.4}$$

The effect of connecting such a diode rectifier bridge to the load-side of the AFE converter system is examined in a simulation environment in Chapter 7.

5.4 Design of LC Filter

As described in the previous chapter, modulation strategies are one way of obtaining a sinusoidal output voltage of the three-phase converter. As a result of the transistor switching operations, harmonic distortion will be present in the converter output signals. In order to mitigate these harmonics, a suitable harmonic filter can be utilized between the converter and the utility grid. Shunt passive LC filters, often called harmonic trap filters, have traditionally been used to attenuate inverter switching harmonics, and hence reduce the flow of harmonic currents into the utility grid. This solutions is simple, low cost, and with high efficiency. Their performance is, however, strongly dependent upon the source impedance and can lead to unwanted

parallel or series resonance with the network [44]. Being highly susceptible to utility line interactions, inverter output LC filters normally require additional active or passive damping [20]. Several precautions have to be taken in the process of LC filter design. First of all, the filter performance with respect to its output voltage is determined by the filter resonance frequency, following Equation (5.5).

$$f_r = \frac{1}{2\pi\sqrt{L_1 C}}, \tag{5.5}$$

with L_1, and C being the LC filter parameters to be determined. In order to obtain a smooth sinusoidal output voltage, the resonance frequency of the filter should be well *below* the lowest switching harmonic of the converter resulting from the PWM operation. Furthermore, the resonance frequency should be designed to be well *above* the fundamental of the converter output voltage in order to prevent undesired resonance suppressing control. A rule of thumb from control theory for ensuring a satisfactory trade-off between these effects is to let the difference of the frequencies in such a configuration be at least a factor of 10. For a converter operating with a fundamental frequency of 60 Hz, this corresponds to having a resonance frequency higher than 600 Hz, and a converter switching frequency of at least 6000 Hz.
The filter parameter values are elaborated based on the rated values of the converter, predetermined limits of current ripples, and for reducing the risk of local network resonances. It should be noted, that in this design process, the stray resistance of the filter inductance can be assumed negligible compared to the inductive reactance at nominal switching frequency [4].

The objective of the filter capacitor, C, is to ensure a smooth sinusoidal output voltage. Considering cost, this component is less expensive than the inductor, meaning that selecting a high capacitor value is a more cost effective way of reducing the resonance frequency. Its upper parameter limit should be considered with the intention of limiting the capacitor current and thus, the ratings required of the converter. In this thesis, as a starting point, the filter capacitor is dimensioned to draw 10% of the fundamental output converter current at rated conditions. This corresponds to the parameter value:

$$C = 0.1 \cdot \frac{I_n}{V_n \omega_0} \tag{5.6}$$

The converter parasitic resistance, R_1 is selected according to values for AFE converter equivalent resistances from the industry.

The filter inductance L_1 is to be selected as to limit the ripple of the converter output current due to its switching operations. A higher inductor value reduces the ripple. However, the inductor is an expensive component. Its value should therefore be selected as to provide a satisfactory trade-off between system cost and inductive voltage drop on one side, and the tolerated current ripple on the other. As a starting point in this project, the filter inductor is designed as to limit the rated voltage drop to 10%. This corresponds to a parameter value given by:

$$L_1 = 0.1 \cdot Z_{base} = 0.1 \cdot \frac{V_n}{\sqrt{3} I_n} \tag{5.7}$$

The location of the output LC filter in the AFE converter configuration is indicated in Figure 6.1.

Chapter 6

Active Front End Converter Control System Design

This chapter enlightens the procedure in which the AFE converter and corresponding control system models are elaborated and designed for simulation purposes. An overview of the system and its parameters is given in Figure 6.1, adapted from [8].

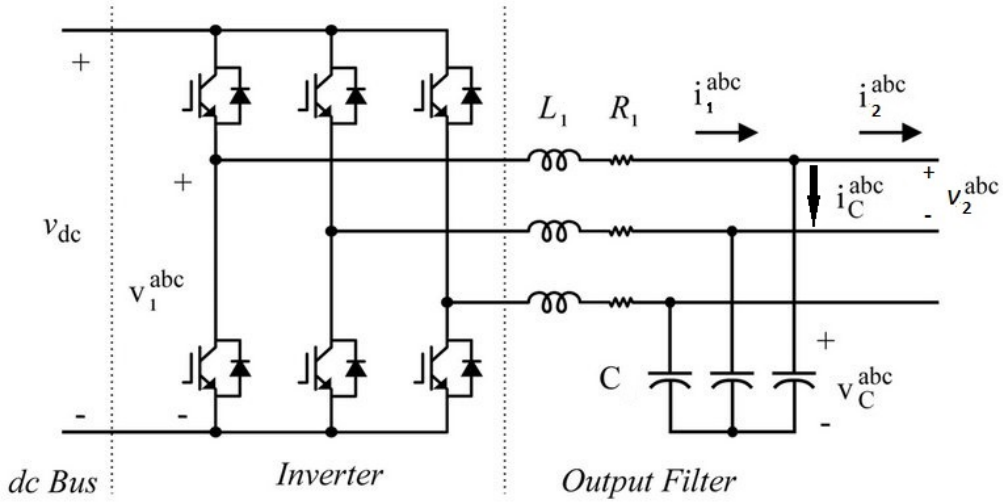

Figure 6.1: System overview

First, the system transfer functions are derived and the different controllers are designed and optimized. An inner current control loop is first considered, then an outer voltage control loop. Consequently, the AFE control system is to be a double cascaded one, consisting of an outer filter capacitor voltage loop and an inner inductor current feedback loop. This control paradigm

has been considered in many researches due to its fast dynamic response and possibility of harmonic compensation [27]. Moreover, the control system is to be implemented in the stationary $\alpha\beta$-reference frame. Different types of controllers are compared and their performance evaluated in the end of the chapter.
The following list reviews the different types of controllers considered in this chapter:

- P controller
- PI controller
- PID controller
- Double PI controller
- P+R controller
- PI+R controller
- PID+R controller
- Double PI+R controller

Several factors have to be considered in the analysis and design of these controllers. Some of these requirements are listed below:

- Stability
- Reference tracking ability
- Disturbance rejection ability
- Rejection of measurement noise
- Model uncertainties

All results presented in this chapter and throughout, are made, using the system parameter values presented in Table 6.1, with notation according to Figure 6.1.

Table 6.1: AFE Converter System Ratings

Parameter	Symbol	Nominal Value
Converter voltage	v_1	690 V
DC bus voltage	V_{dc}	1050 V
Converter current	i_1	800 A
Grid-frequency	f_0	60 Hz
Line angular velocity	ω_0	376.99 rad/s
PWM switching time period	T_{sw}	0.167 ms
Filter inductance	L_1	0.1 mH
Converter side parasitic resistance	R_1	7 mΩ
Filter capacitance	C	1mF
Grid side parasitic resistance[1]	R_c	0.2 mΩ
Processor time delay	T_{dsp}	0.167 ms
Anti-aliasing time delay[2]	T_f	0 s

[1]The location of R_c is not indicated in Figure 6.1 as it is disregarded in this chapter. It is included later in the simulation model of Chapter 7, connected in series with C.
[2] Assumed negligible for a simulation environment

The LC filter parameters are selected in accordance to the criteria and rule of thumb of Section 5.4. As is the case for the converter switching frequency.

To design a control system that applies per-unit values, transformations of the system ratings of Table 6.1 are carried out according to Appendix A. A list of the resulting per-unit filter quantities, applied for controller design and optimization, is given in Table 6.2.

Table 6.2: AFE Converter LC Filter Per-Unit Ratings

Parameter	Symbol	Per-Unit Value
Filter capacitive reactance	x_c	7.10
Filter inductive reactance	x_l	0.076
Filter resistance	r_1	0.014

An overview of the control system employed in the stationary $\alpha\beta$-reference frame is given in Figure 6.2, adapted from [39]:

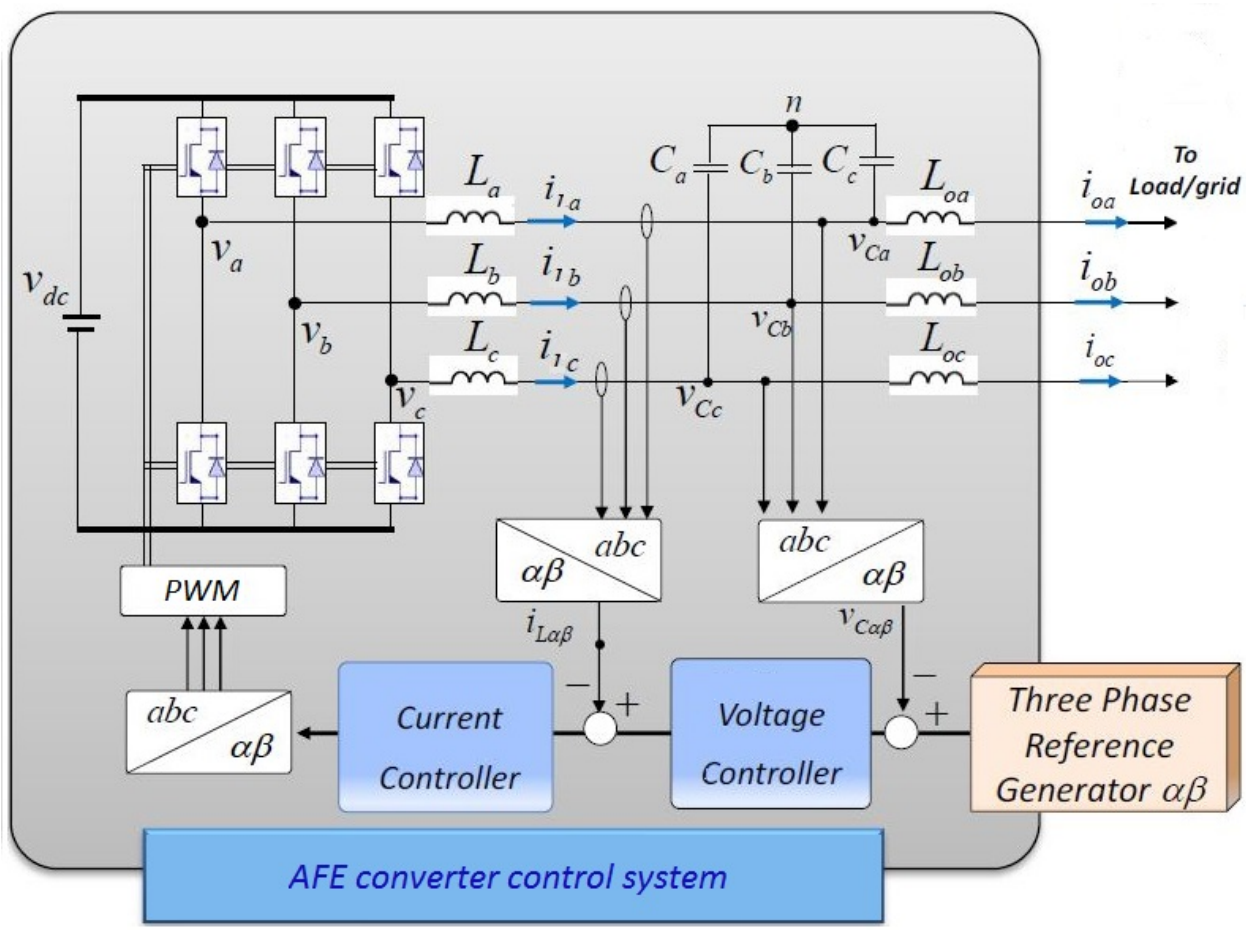

Figure 6.2: Control system in stationary $\alpha\beta$-reference frame, adapted from [39]

6.1 Inner Current Control Loop

Based on the overview of the system of Figure 6.1, the inner current control loop structure can be designed and its controllers tuned. The current that is to be measured and controlled is the converter output current i_1, as illustrated in the Figure 6.2. With respect to this figure, the transfer function of i_1 can be derived by considering the following two circuit equations in the frequency domain:

$$i_1(s) = \frac{v_1(s) - v_c(s)}{R_1 + L_1 s} \tag{6.1}$$

$$Cs \cdot v_c(s) = i_1(s) - i_2(s) \tag{6.2}$$

By substituting $v_c(s)$ in (6.1) with the expression of (6.2), the following transfer function for i_1 is obtained:

$$i_1(s) = \frac{Cs}{L_1Cs^2 + R_1Cs + 1} \cdot v_1(s) + \frac{1}{L_1Cs^2 + R_1Cs + 1} \cdot i_2(s) \tag{6.3}$$

Based on the transfer function of (6.3), and the remaining system blocks, the following simplified block diagram can be derived, to model the AFE converter and its inner current control loop:

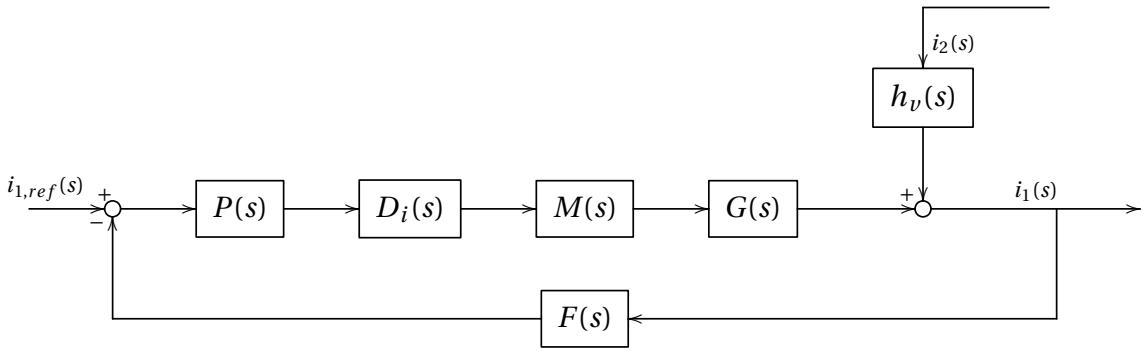

Figure 6.3: Simplified block diagram of AFE converter and inner current control loop

Considering the block diagram above, a list of the respective blocks and their transfer functions is presented next:

- The block $P(s)$ represents the time delay caused by the processor and current measurements and is modeled as follows:

$$P(s) = \frac{1}{1 + T_{dps}} \tag{6.4}$$

- $D_i(s)$ is the regulator block of the current controller with transfer function depending on the selected controller type.

- M(s) is the modulator block given by:

$$M(s) = \frac{1}{1 + T_{pwm}s}, \tag{6.5}$$

where the time constant T_{PWM} can be modeled as half of the switching period, T_{sw}, [32], that is:

$$T_{pwm} = \frac{1}{2}T_{sw} \tag{6.6}$$

- The block $G(s)$ represents the plant transfer function of $i_1(s)$:

$$G(s) = \frac{Cs}{L_1Cs^2 + R_1Cs + 1}, \tag{6.7}$$

with the plant time constant T_1 given by the relation:

$$T_1 = \frac{L_1}{R_1} \tag{6.8}$$

- The anti-aliasing filter block, $F(s)$ is characterized by the transfer function:

$$F(s) = \frac{1}{1 + T_f s} \tag{6.9}$$

- Finally, the disturbance $h_v(s)$ from i_2 to i_1 in 6.3 is represented by the following transfer function:

$$h_v(s) = \frac{1}{L_1Cs^2 + R_1Cs + 1} \tag{6.10}$$

By defining an equivalent system time constant, T_{sum},

$$T_{sum} = T_f + T_{pwm} + T_{dsp}, \tag{6.11}$$

a further simplification of the block diagram of the current control loop can be done, according to Figure 6.4:

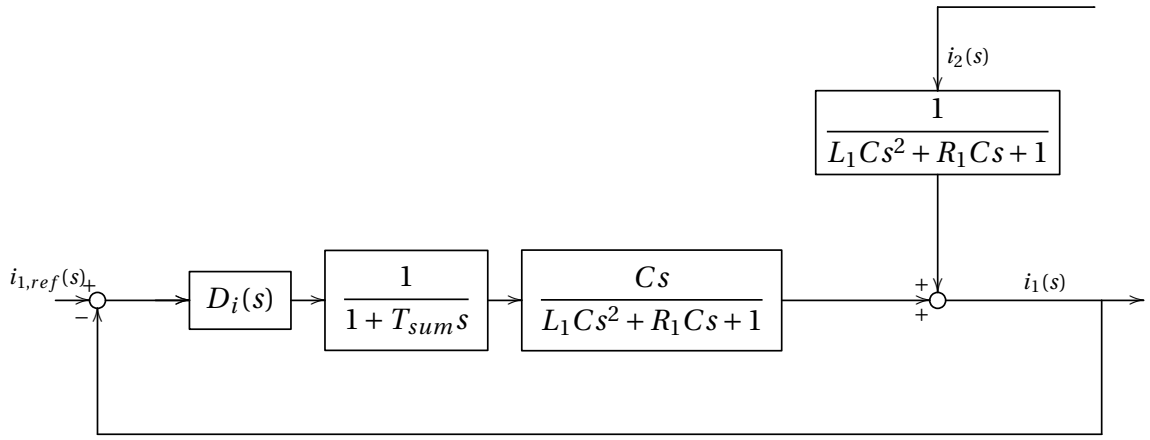

Figure 6.4: Block diagram model of the AFE converter and inner current control loop with a general current controller, $D_i(s)$.

Considering the block diagram of 6.4 and the block transfer functions of (6.4) - (6.10), the transfer function, h_{0i}, can be derived, modeling the open current control loop, by neglecting the disturbance from $i_2(s)$:

$$h_{0i} = D(s)\frac{Cs}{(1+T_{sum}s)(L_1Cs^2+R_1Cs+1)} = D(s)\frac{Cs}{T_{sum}L_1Cs^3+(L_1C+T_{sum}R_1C)s^2+(R_1C+T_{sum})s+1} \tag{6.12}$$

By applying the per-unit transformation as described in A, the open loop transfer function can be expressed as indicated in (6.13), using per-unit values:

$$h_{0i,pu} = D(s)\frac{s}{\omega_0 x_c(\frac{x_l}{\omega_0^2 x_c}s^2+\frac{r_1}{\omega_0 x_c}s+1)(1+T_{sum}s)} \tag{6.13}$$

The AFE converter block diagram representation of Figure 6.4 along with the open loop transfer functions of (6.12)-(6.13) will form the basis for the controller tuning and design to be elaborated in this section. Throughout, two different system representations will be considered, one "complete", and one "simplified", their difference being in the plant transfer function employed. The open loop transfer functions of (6.12), (6.13), employing the complete plant transfer function of (6.7), will in the following, be referred to as *the "complete" system transfer function model.* Replacing the open loop system transfer function of (6.12)

with the simplified plant transfer function of (6.15), results in the open loop transfer function representation that is referred to as *the "simplified" system transfer function model.* This simplification is utilized in some references for controller tuning and design, and is therefore included in this thesis, in order to study and evaluate its validity compared to the more detailed system representation.

A comparison of the frequency responses of the simple plant transfer function of (6.15), and the complete plant of (6.7) is given in the bode diagram of Figure 6.5

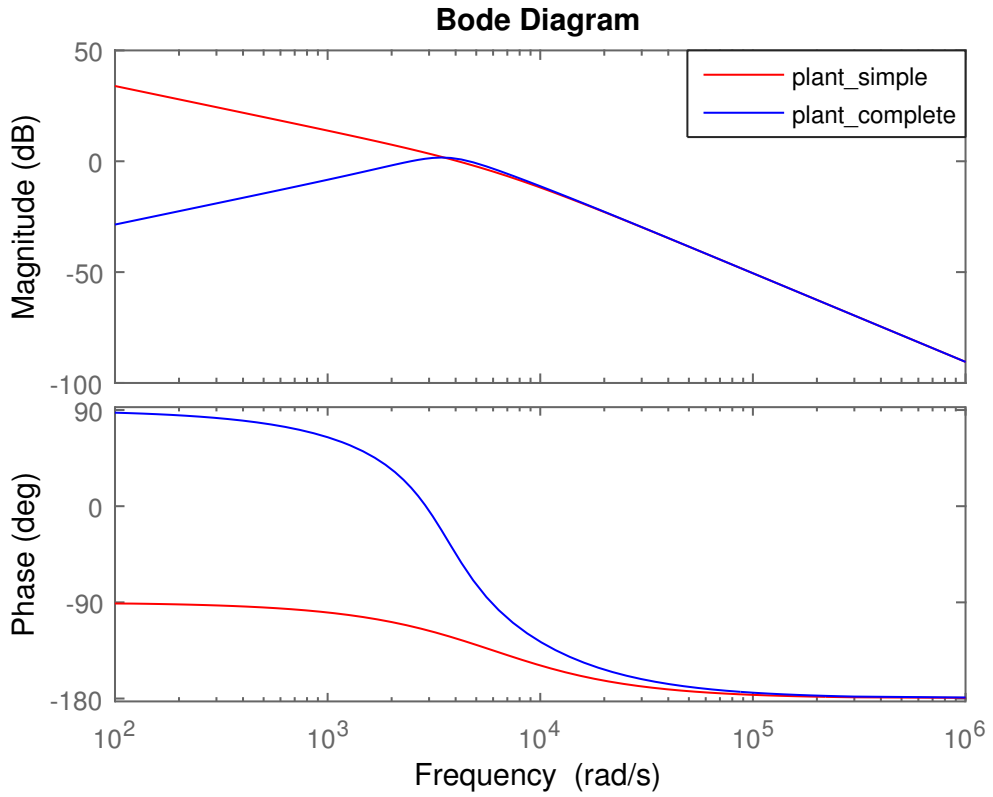

Figure 6.5: Bode plots comparing the response of the simplified and complete plant transfer functions

Considering Figure 6.5, it can be seen that the two plant representations show similar responses at higher frequencies, that is, at frequencies $> 10^4$ rad/s.

6.1.1 Proportional Current Controller

Below, the frequency- and current step responses are presented in Figures 6.6-6.8, of the simplified and complete current control transfer function models, respectively, employing a proportional controller. The controller is tuned in order to obtain satisfactory stability margins, in accordance to Appendix B.

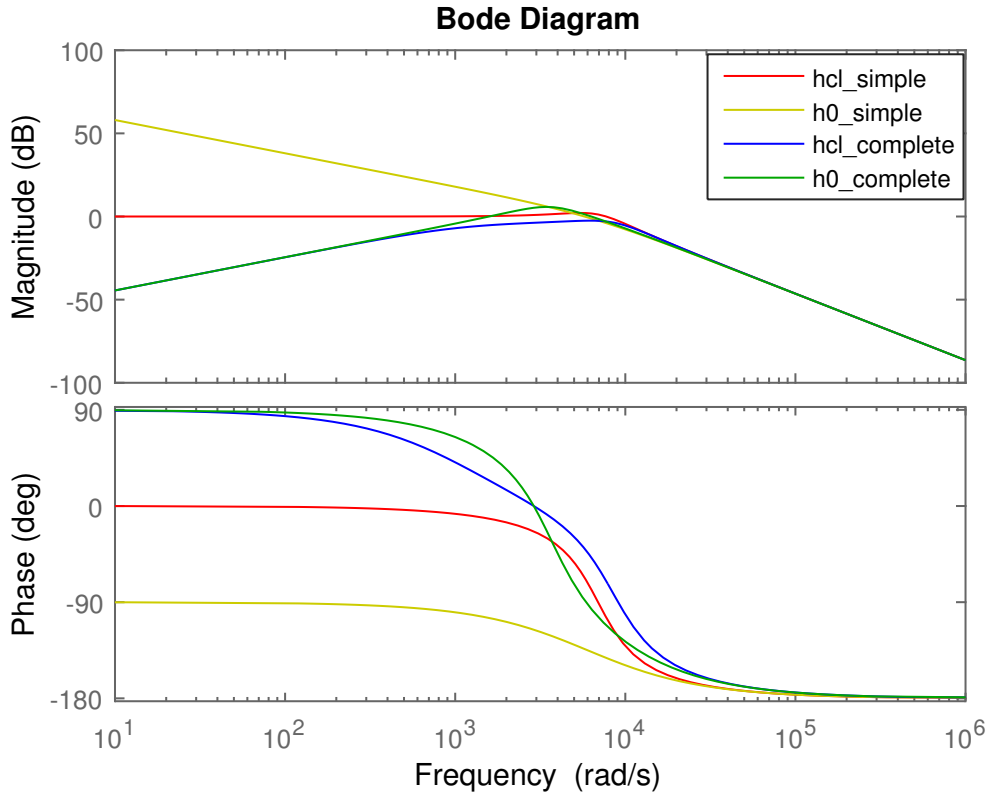

Figure 6.6: Bode plots comparing the response of the simplified and complete transfer function models employing P controller

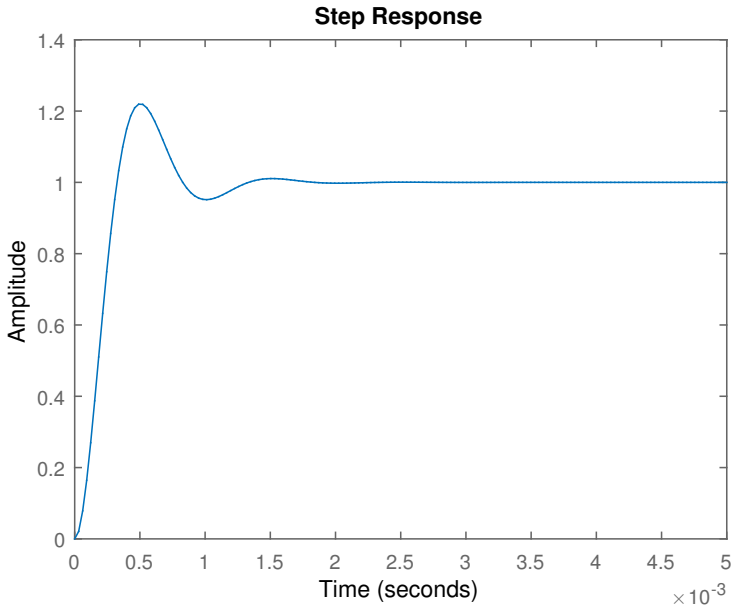

Figure 6.7: Unity step response of the current employing a P current controller and the simplified system model

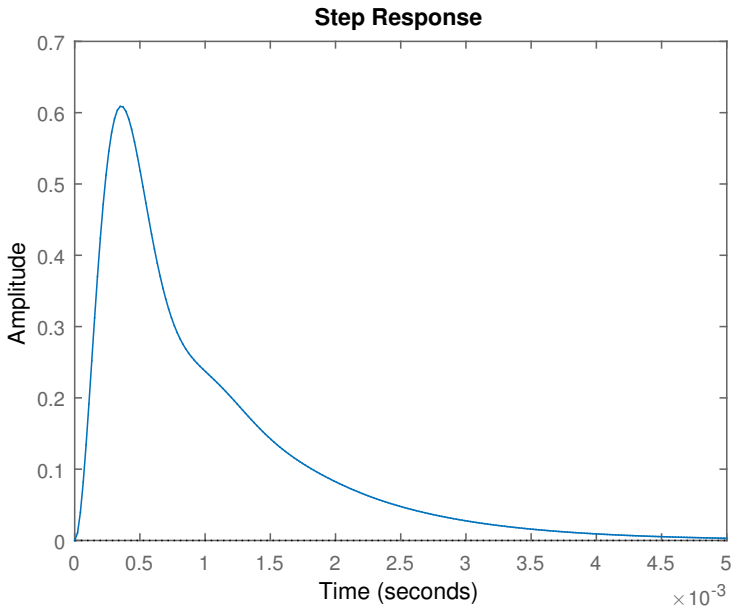

Figure 6.8: Unity step response of the current employing a P current controller and the complete system model

Figure 6.8 shows that the P controller is unable to track a step reference when the complete plant model is included.

6.1.2 Tuning of PI Current Controller Using Symmetrical Optimum

In order to obtain a suitable current control response, the control parameters, K_i and T_i of the PI current controller transfer function in Equation (4.17), must be tuned. The literature provides several different strategies for the tuning of these parameters, yielding different properties in terms of control speed, overshoot with step input, and rejection of disturbances. This section describes the tuning of the inner current controller of the AFE converter using the symmetrical optimum (SO) technique, which results in a controller with fast response to changes in the reference as well as disturbance rejection, compared to the conventional modulus optimum tuning strategy. However, the system needs to be able to tolerate a relatively high overshoot. Employing PI current controllers, the inner control loop of the AFE-controller can be represented as indicated in Figure 6.9 and in the open loop transfer function of (6.14).

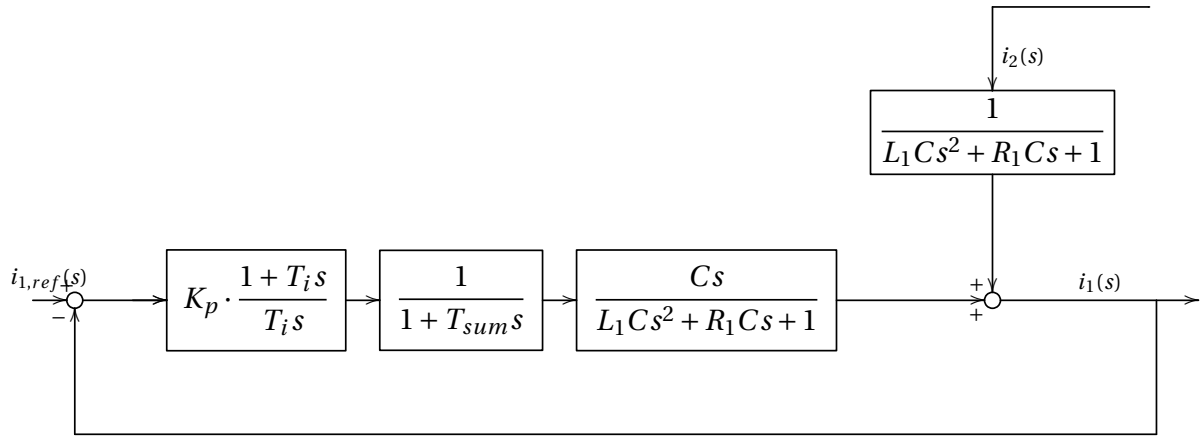

Figure 6.9: Block diagram model of AFE converter inner current control loop with PI controller

$$h_{0,i} = \frac{K_p(1+T_is)Cs}{T_is(1+T_{sum}s)(L_1Cs^2+R_1Cs+1)} = \frac{K_p(1+T_is)C}{T_i(T_{sum}L_1Cs^3+(L_1C+T_{sum}R_1C)s^2+(R_1C+T_{sum})s+1)} \tag{6.14}$$

The tuning procedure of the PI current controllers is elaborated here, using the symmetrical optimum criterion, as described in [9] for a three-phase voltage-source converter with an LC output filter. For simplification of the tuning procedure, the plant transfer function is in this

reference reduced to a single inductor with a pure integrator under the assumption of a large plant time constant T_1, that is:

$$G(s) \approx \frac{1}{L_1 s} \tag{6.15}$$

By comparing the simplified plant transfer function of Equation (6.15) to the complete one of (6.7), it can be noticed that this simplification corresponds to a case where a high frequency component is applied to the plant, allowing for the low order terms to be neglected. This relation can be observed in the bode diagram comparison of the two plant representations i Figure 6.5. The validity of using this particular simplification for the system of interest in this thesis, is later evaluated in Chapter 7. The open loop transfer function of (6.12) can in this case be expressed, as in (6.16):

$$h_{0i}(s) \approx \frac{K_p(1 + T_i s)}{T_i s(1 + T_{sum} s) s L_1} \tag{6.16}$$

With this simplified open loop transfer function, the PI-controller parameters can be obtained by the symmetrical optimum criterion, using the two relations below:

$$K_p = \frac{L_1}{a T_{sum}} \tag{6.17}$$

and,

$$T_i = a T_{sum} \tag{6.18}$$

in which, the factor $a > 1$, links the control parameters to the desired open loop phase margin ψ, (see Appendix B), through (6.19):

$$a = \frac{\cos(\psi)}{1 + \sin(\psi)} \tag{6.19}$$

Based on [9], a phase margin of $\psi = 45°$, corresponding to a value of $a = 1+\sqrt{2}$, results in a current controller with good disturbance rejection, but a high overshoot when applying a step reference. Following the tuning procedure described above, the bode plot of the open loop system is to be symmetrical around the cross frequency ω_c, providing a maximum phase margin, thus the name "symmetrical optimum". A comparison of the open- and closed loop transfer function frequency responses of the the simplified transfer function model of (6.16) and the complete

transfer function model of (6.12) is presented in the bode diagram of Figure 6.10.

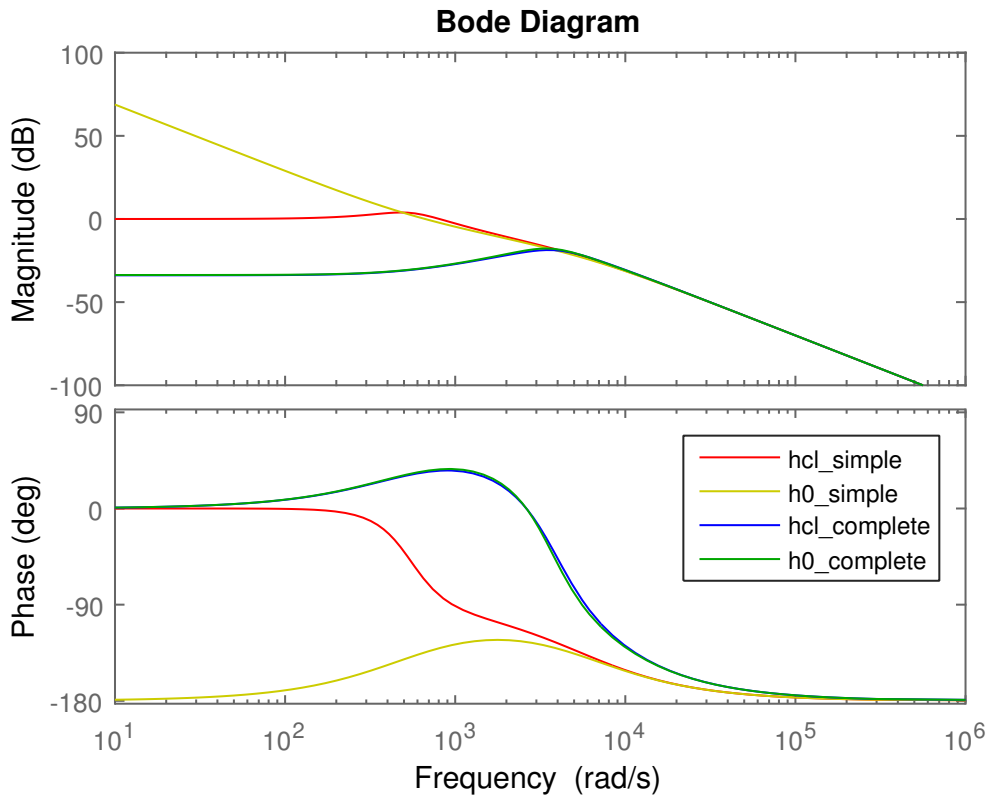

Figure 6.10: Bode diagrams of open- and closed loop transfer functions with PI current controllers employing the simplified transfer function model of (6.16) compared to the complete transfer function model of (6.12)

In the bode plot of Figure 6.10, the PI controller parameters of the simplified transfer function are tuned according to the symmetrical optimum procedure described in this section. The same control parameters are applied for the PI controller of the complete transfer function model of the current control loop. As can be seen from the yellow line of the bode diagram, the phase margin of the closed loop simplified model is a bit higher than 45°, which should yield sufficient stability margins, in line with [9], and the control theory described in Appendix B.

Figures 6.11, and 6.12 show the unity step responses of the closed loop simplified and complete systems, respectively tuned after the symmetrical optimum criterion, as described above.

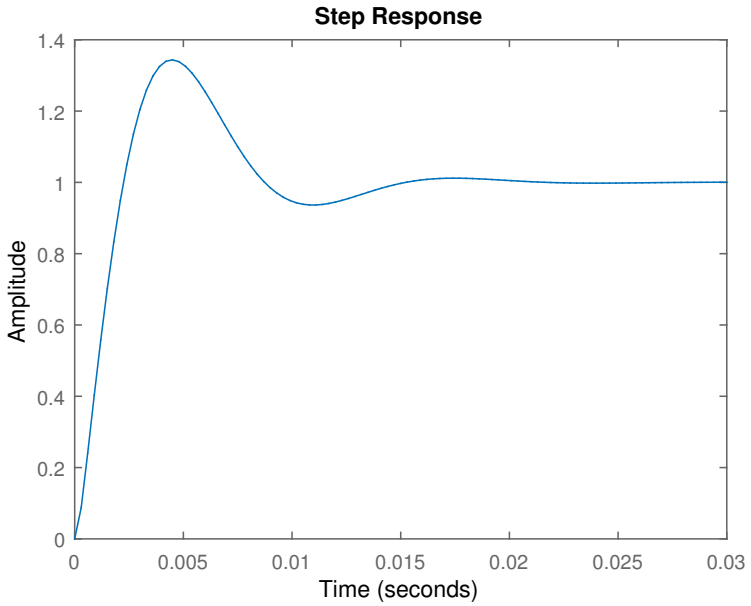

Figure 6.11: Unity step response of the current employing the simplified system of (6.16)

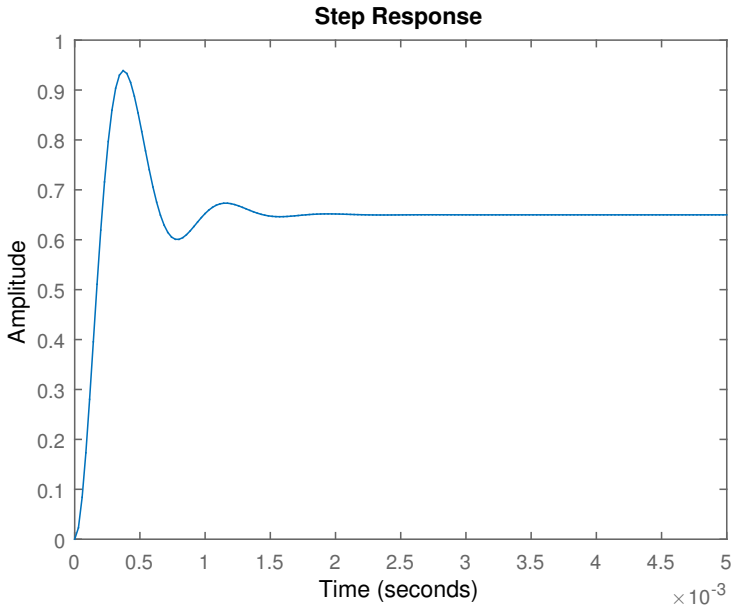

Figure 6.12: Unity step response of the current employing the complete system of 6.14

When comparing the two responses plotted in Figures 6.11, and 6.12, it can be seen that the controller tuned for the complete system transfer function model is much quicker than that of the simplified system model. However, the output of the complete system is not able to perfectly

track the reference, resulting in a stationary deviation.

6.1.3 Tuning of PID Current Controller Using Symmetrical Optimum

Another option for implementation of the inner current control of the AFE converter is by means of PID controllers. This section describes and compares how the symmetrical optimum criteria can be used for tuning of two different types of PID controllers in the frequency domain, namely the parallel type PID controller, and the PID controller with limited derivative action. Their difference lie in the number of associated control parameters, and the way in which they are implemented.

Tuning of Parallel Type PID Current Controller

The first PID controller to be tuned is a *parallel form* controller, given by the transfer function:

$$D_i(s) = K_c(1 + \frac{1}{T_i s} + T_d s) \tag{6.20}$$

Replacing the PI controller of Figure 6.4, with the PID controller of (6.20), the resulting AFE inner control loop will become as is indicated in the block diagram of Figure 6.13.

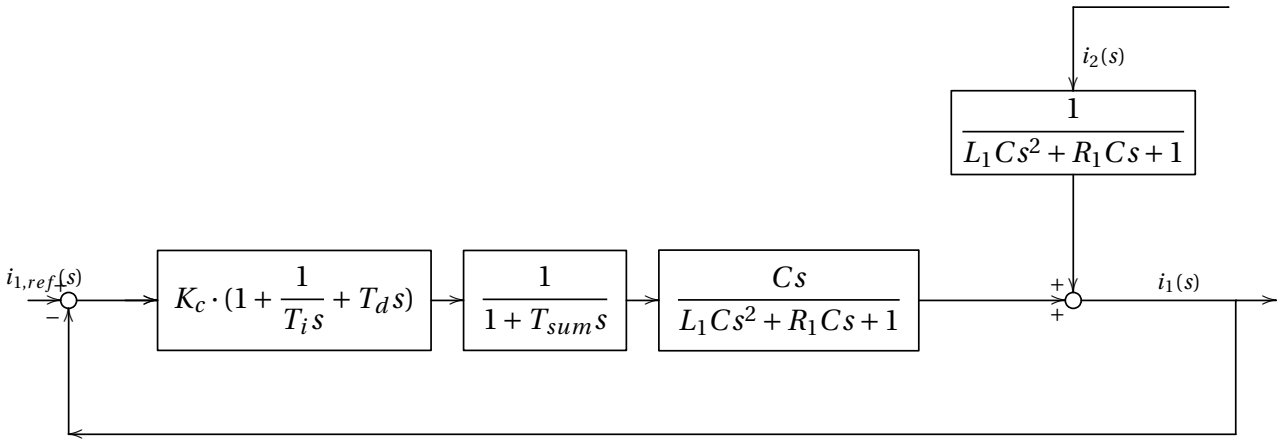

Figure 6.13: Block diagram of AFE converter and inner current control loop with parallel type PID controller.

As for the PI current controller, the PID controller parameters, K_c, T_i, and T_d can be tuned by the symmetrical optimum technique for obtaining a suitable current control response. Using the general strategy presented in [45], this can be achieved by considering the bode diagram of the open loop system *without* a controller. This corresponds to considering the open loop transfer function of (6.12) *without* the controller, $D_i(s)$ for the complete system model. In the same way, the open loop transfer function:

$$h_{0i,nc}(s) = \frac{1}{L_1 s(1 + T_{sum} s)}, \tag{6.21}$$

is considered in the case where the simplified plant model is included. Considering the frequency response of the controller-less open loop system of interest, the PID controller parameters can be tuned by applying the following general relations (using the same notation as in [45]):

$$K_c = \frac{B(4+B)}{8\sqrt{2}\, K_{135}}, \tag{6.22}$$

$$T_i = \frac{4+B}{B\omega_{135}}, \tag{6.23}$$

and,

$$T_d = \frac{B}{(4+B)\omega_{135}}, \tag{6.24}$$

in which K_{135}, and ω_{135} are the gain and angular frequency corresponding to the system phase angle of $-135°$, while $B \in [1,2]$ is an acceleration factor.

In Figure 6.14, bode plots are presented, comparing the frequency responses of the open- and closed loop transfer functions associated with the simplified model of (6.21) employing the PID controller of (6.20), to the complete transfer function model of (6.12). Their parallel type PID controllers tuned according to the procedure described above.

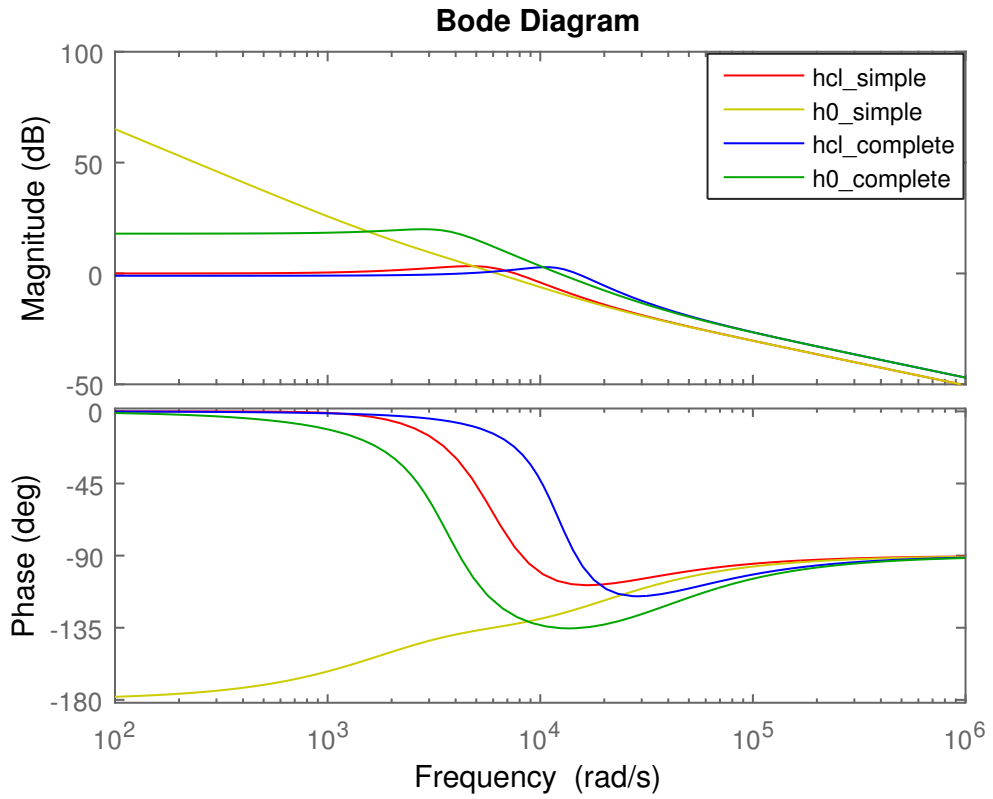

Figure 6.14: Bode plot of open- and closed loop transfer functions with parallel type PID current controllers

The current step responses of the simplified and complete system models associated with the bode diagram of Figure 6.14, are displayed in Figures 6.15 and 6.16. Their responses are plotted for three different values of the acceleration factor B.

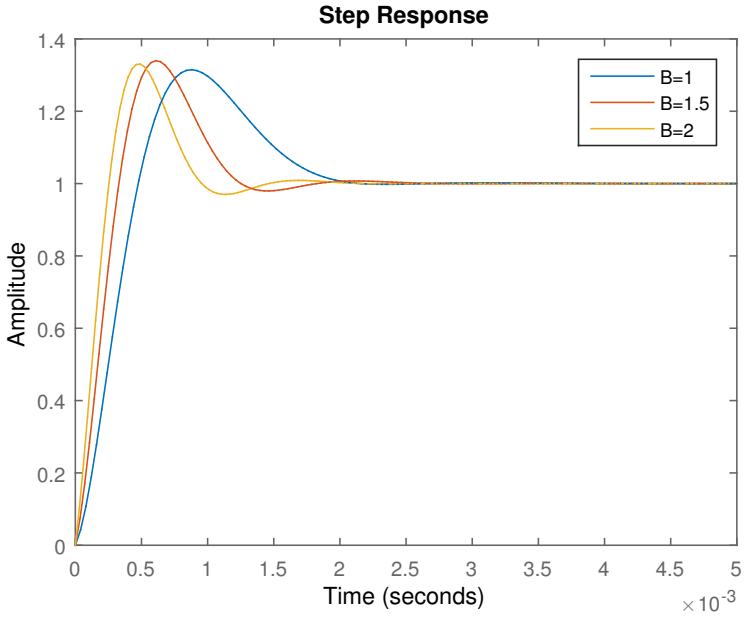

Figure 6.15: Unity step response of the current, employing the simplified system model of (6.21) with the parallel type PID controller of (6.20)

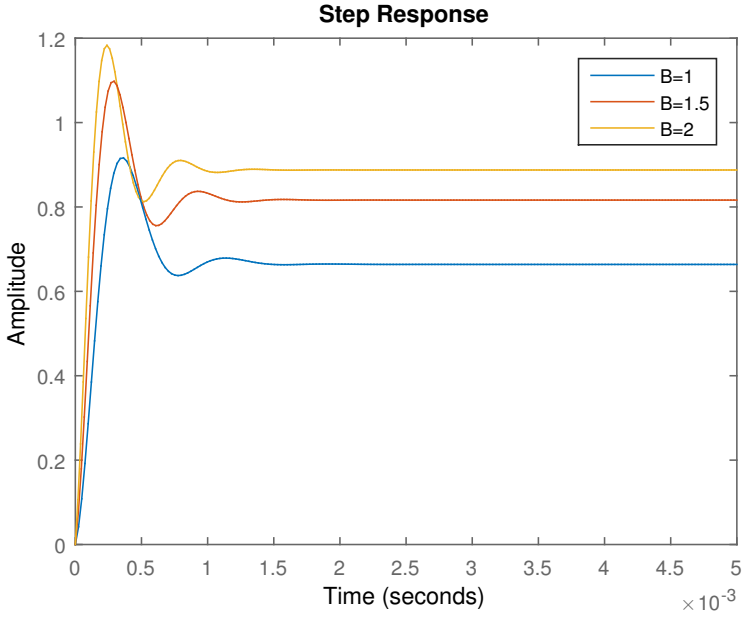

Figure 6.16: Unity step response of the current with the complete model of Figure 6.13

Compared to the step responses of the PI controller of Figure 6.11, and 6.12, the system step responses with the parallel PID controller show the same trend, being that the closed loop sys-

tem of the system is unable to track the reference resulting in a stationary deviation. As can be observed in Figure 6.12, this deviation is reduced by increasing the acceleration factor, B, and thus an increase the controller gain, K_c. This, however results in an unwanted increase of the response overshoot.

Tuning of PID Current Controller with Limited Derivative Action

The second PID controller to be tuned, using the symmetrical optimum criteria, is represented by the following transfer function, using the notation and procedure of [46]:

$$D_i(s) = \frac{(1+sT_n)(1+sT_v)}{sT_i(1+sT_{\sum c})}, \tag{6.25}$$

The controller of (6.25) is quite similar to the parallel form controller of (6.20), their difference being the PI+limited derivative action, described in 4.4.3. The procedure of [46] describes the control of the general integrating plant transfer function:

$$G(s) = \frac{1}{sT_m(1+sT_{p1})(1+sT_{\sum p})}. \tag{6.26}$$

By defining a new time constant according to (6.27),

$$T_{\sum} = T_{\sum c} + T_{\sum p}, \tag{6.27}$$

the PID-control parameters of the AFE converter in this thesis can be tuned as indicated in (6.28) by comparing the general plant transfer function of (6.26) to the simplified and complete ones of (6.7) and (6.15), to meet the symmetrical optimum criterion [46], [47].

$$T_v = T_{p1}, \quad T_i = 8K_pK_h\frac{T_{\sum}^2}{T_m}, \quad T_n = 4T_{\sum}, \tag{6.28}$$

K_p and K_h are the open- and closed loop gains, respectively. By replacing the controller block of the AFE converter system of Figure 6.13 with the PID controller of (6.25), the system properties with this controller can be tested. The corresponding bode plots of the complete and simplified system model are displayed in Figure 6.17.

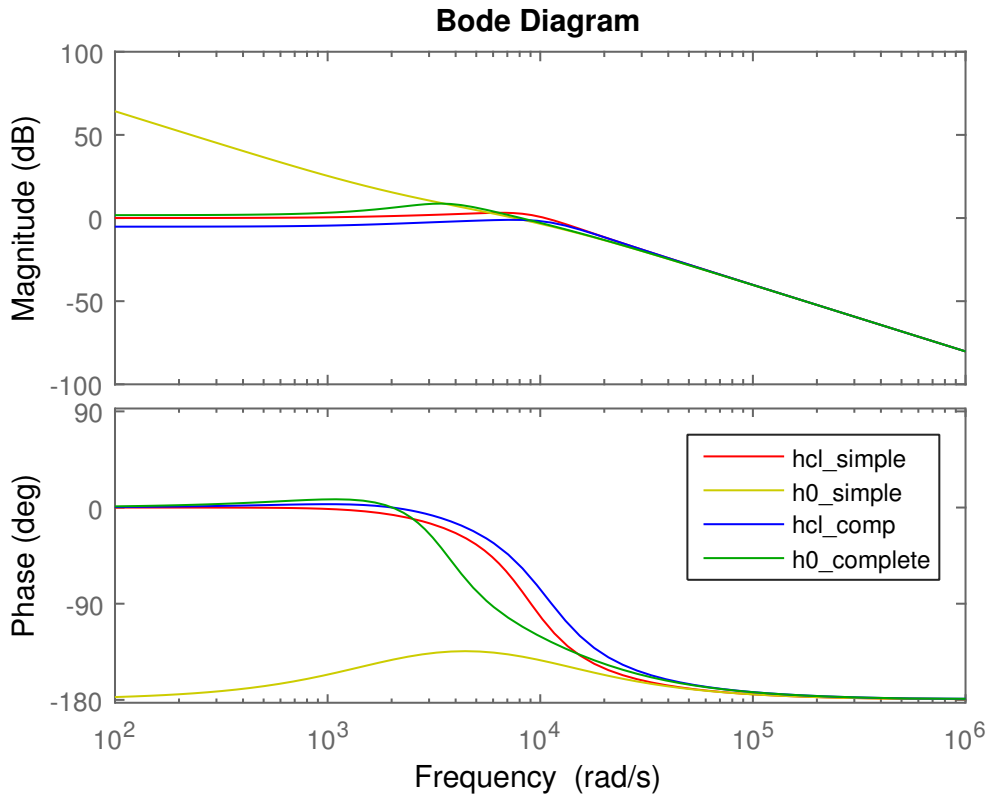

Figure 6.17: Bode plot of open- and closed loop transfer functions with PID current controller with limited derivative action

The effect of the limited derivative controller action can be seen, resulting in a frequency response more similar to that of the PI controller in Figure 6.10 rather than the one of the ideal parallel type PID controller of Figure 6.14. The step responses of the complete and simplified system representation can be seen in Figures 6.18 and 6.19, showing a similar behavior as for the parallel type PID controller with a stationary deviation in the current output with the complete plant model.

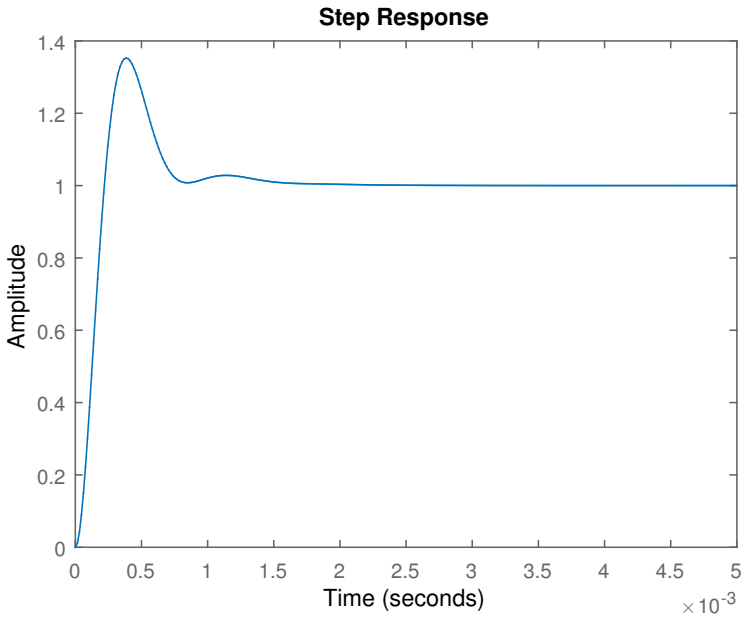

Figure 6.18: Unity step response of the current, employing the simplified system model of (6.21)

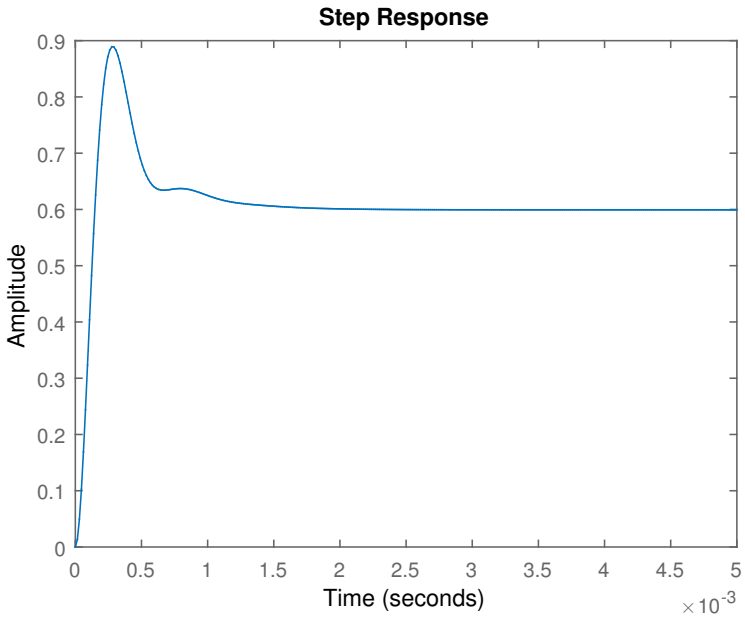

Figure 6.19: Unity step response of the current, employing the complete system model

6.1.4 Double PI Controller

Current control using double PI controllers is a solution that is not commonly applied in the industry. This section, however, is aimed to investigate the effect of applying such a controller for the AFE converter system of interest, and exploring how the utilization of two pure integrators in the control paradigm affects the system properties. By introducing an additional controller time constant, T_{i2}, the double PI controller to be treated in this section is in fact the squared of the ideal PI controller of (4.17), yielding the following controller transfer function:

$$D_i(s) = K_p \cdot \frac{(1 + T_i s)(1 + T_{i2} s)}{T_i T_{i2} s^2} \tag{6.29}$$

The results provided in this section are, hence, to introduce and motivate the use of the more established resonant controllers for current control in the stationary $\alpha\beta$-reference frame. Using trial-and error, the double PI controller is tuned for the AFE current control model. The results are shown below, both for the complete- and simplified transfer function models. It should however be noted, that the given results are obtained with the objective of achieving suitable behavior for the *complete* system model, that is, the tuning was carried out with the aim of reaching satisfactory stability margins and dynamic responses for the complete system model.

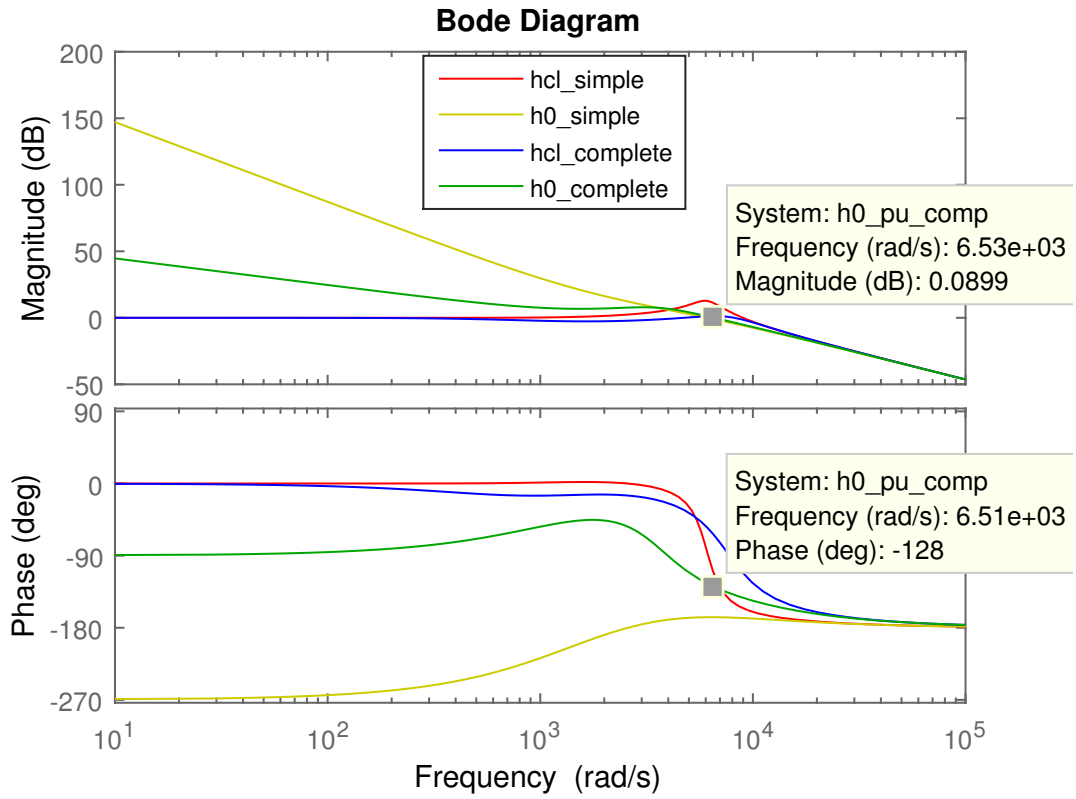

Figure 6.20: Bode plots of open- and closed loop system transfer functions with double PI current controller.

What is interesting to observe in the bode plots of Figure 6.20 is that satisfactory stability margins are obtained for the open loop transfer functions of the complete system. Moreover, this open loop frequency response has a magnitude higher than zero as opposed to what is observed in the cases with single PI- and PID controllers. Also, the closed loop transfer functions of the complete and simplified models show better tracking abilities of the zero-phase angle at higher frequencies than what is observed in the previous cases. This corresponds to having a controller that makes the system better suited for tracking of sinusoidal reference signals, also at higher frequencies, as described in Appendix B. There is, however, a slight deviation at the fundamental frequency, meaning that some phase lag of the current can be expected compared to the reference. For the simplified system, these control parameter values result in a bit lower stability margins, which is evident when studying the unit step response below:

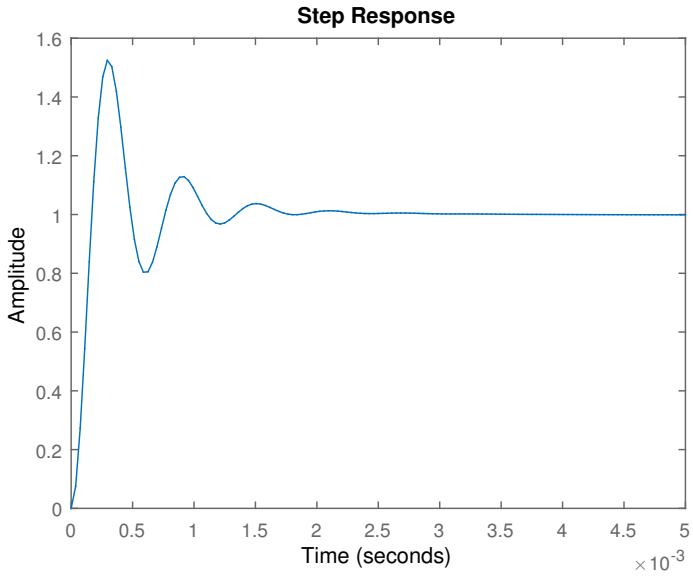

Figure 6.21: Unity step response of the current in the simplified system model, employing double PI controller

With the selected control parameters for the double PI controller, the response of the simple model is quicker, but more oscillatory than in the previous cases, reflecting the lower stability margin.

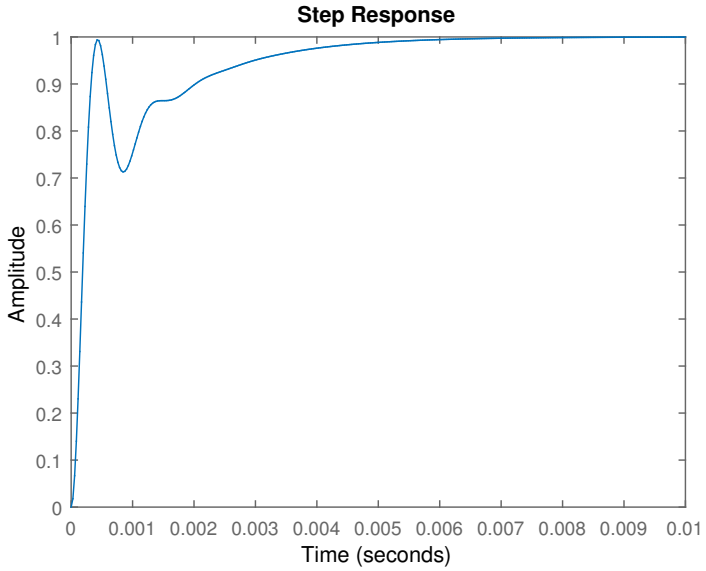

Figure 6.22: Unity step response of the current in the complete system model, employing double PI controller

When comparing the step response of Figure 6.22 with the responses of the previous complete models, it can be seen that in the first millisecond, the trajectory is quite similar to what has been observed earlier. But, as opposed to the previous controllers, the double PI controller eventually manages to lift the output response so that it equals the reference, and hence, completely removes the stationary deviation.

6.1.5 Resonant Current Controllers

This section investigates the effect of including a resonant controller tuned at the fundamental frequency along with the current controllers already reviewed in this chapter. This is done in order to verify the properties of resonant controllers, described in Section 4.4.4, as well as for providing a basis for selecting one of these controllers for further study in a simulation model of the AFE converter system. Below, the bode diagrams of the closed and open loop system transfer functions are provided, with the following four types of current controllers:

1. Proportional + Resonant (PR)
2. Proportional Integral + Resonant (PIR)
3. Proportional Integral Derivative + Resonant (PIDR)
4. Double PI + Resonant

Again, both the simplified and complete transfer function models are plotted, in order to obtain the best basis possible for comparison with the controllers without the resonant terms:

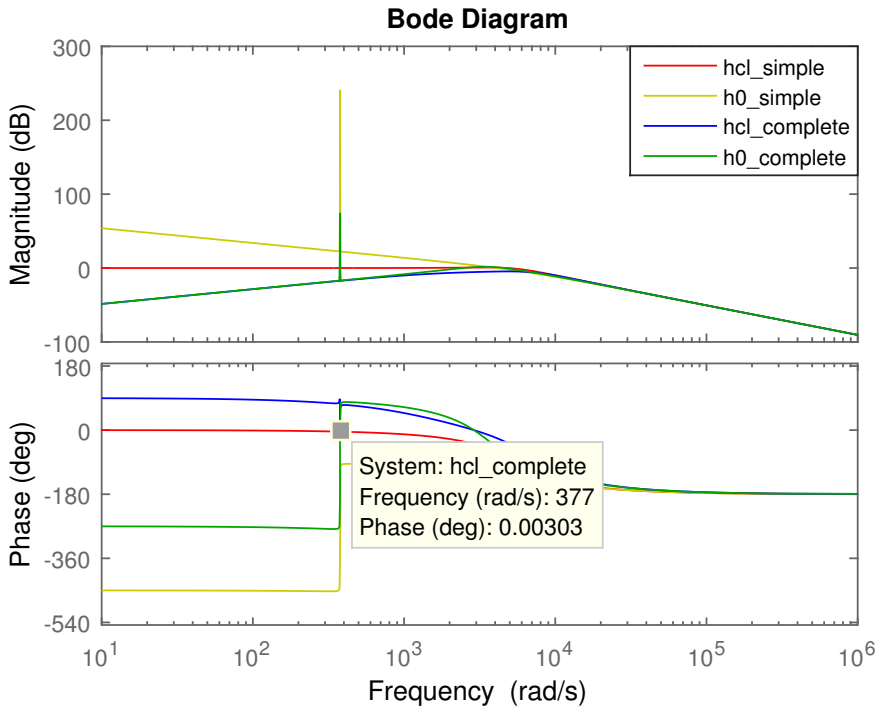

Figure 6.23: Bode plots of open- and closed loop system transfer functions with P+R current controller

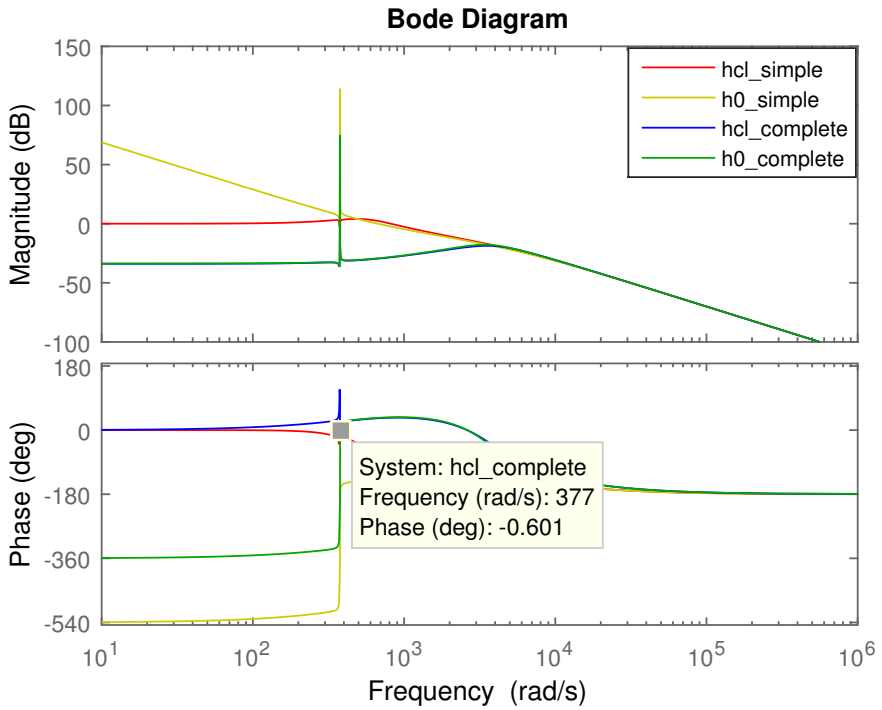

Figure 6.24: Bode plots of open- and closed loop system transfer functions with PI+R current controller

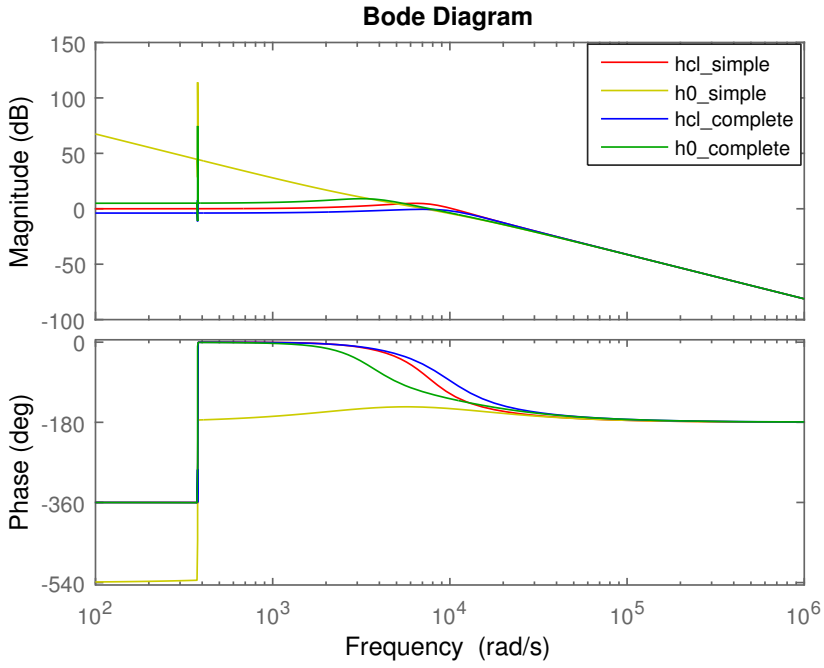

Figure 6.25: Bode plots of open- and closed loop system transfer functions with PID+R current controller

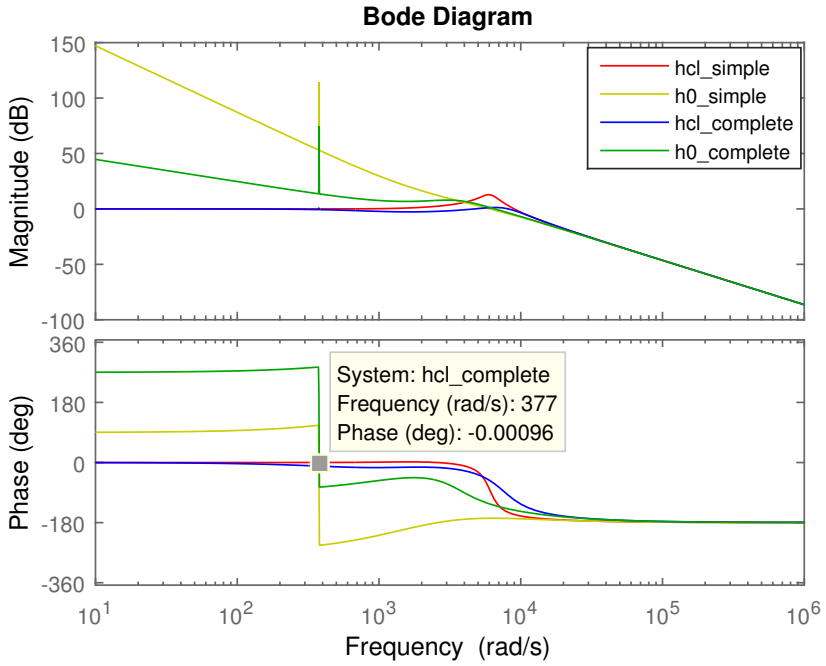

Figure 6.26: Bode plots of open- and closed loop system transfer functions with double PI+R current controller

Out of the two types of PID controllers reviewed in this chapter, only the one with the limited derivative action is considered here, due to this being the one later to be implemented in the simulation model of Chapter 7.

With respect to the theory of resonance controllers provided in Section 4.4.4, the properties described can be seen when considering the bode diagrams of Figures 6.23-6.26. The resonant part, being tuned at the fundamental frequency of ω_0 = 377 rad/s, is evident when studying these diagrams. As described in theory, the open loop gains can be approximated as infinite at the resonance frequency. These peaks are, however limited by the damping property of the physical system. In theory, this should correspond to a unity closed loop gain at the resonance frequency. Again, it can be seen that this is evident as an approximation for the frequency responses above. However, in all of the four cases, the resonance term provides a closed loop phase angle of zero at the resonance frequency, corresponding to a perfect tracking of a sinusoidal reference signal of the fundamental frequency.

Out of the four resonant controllers considered here, the PI+R is selected to be studied further in a complete simulation model of an AFE converter, including outer voltage control loop

with harmonic compensation.

Due to the resonant controllers being tuned at the fundamental frequency, the unity step responses of the controllers without the resonant terms remained unchanged. These plots are therefore omitted in this part.
This analysis has been carried out, considering the continuous system transfer functions, only. According to the the theory regarding discretization in Section 4.5, an analysis of the discrete system model should also be conducted, in order to study modification of the system properties due to the transformation to the digital z-domain. Next, an analysis is therefore given of the discrete AFE converter current control system, employing PIR controllers including harmonic cancellation.

6.1.6 Discretization of PIR Current Controller

The discrete-time PIR controller implementation studied in this section is a combination of the resonant controller presented in Section 4.5.1 with addition of a digital PI controller, $D_{PI}(z)$, in the controller output, as indicated in equation (6.30)

$$D_{i,PIR}(z) = D_{PI}(z) + T_s \frac{z^{-1}\cos(h\omega_0 T_s + \phi_h^*) - z^{-2}\cos(\phi_h^*)}{1 - 2z^{-1}(1 - C_h\frac{T_s^2}{2}) + z^{-2}} \tag{6.30}$$

The corresponding block diagram of $D_{i,PIR}(z)$ is depicted in Figure 6.27.

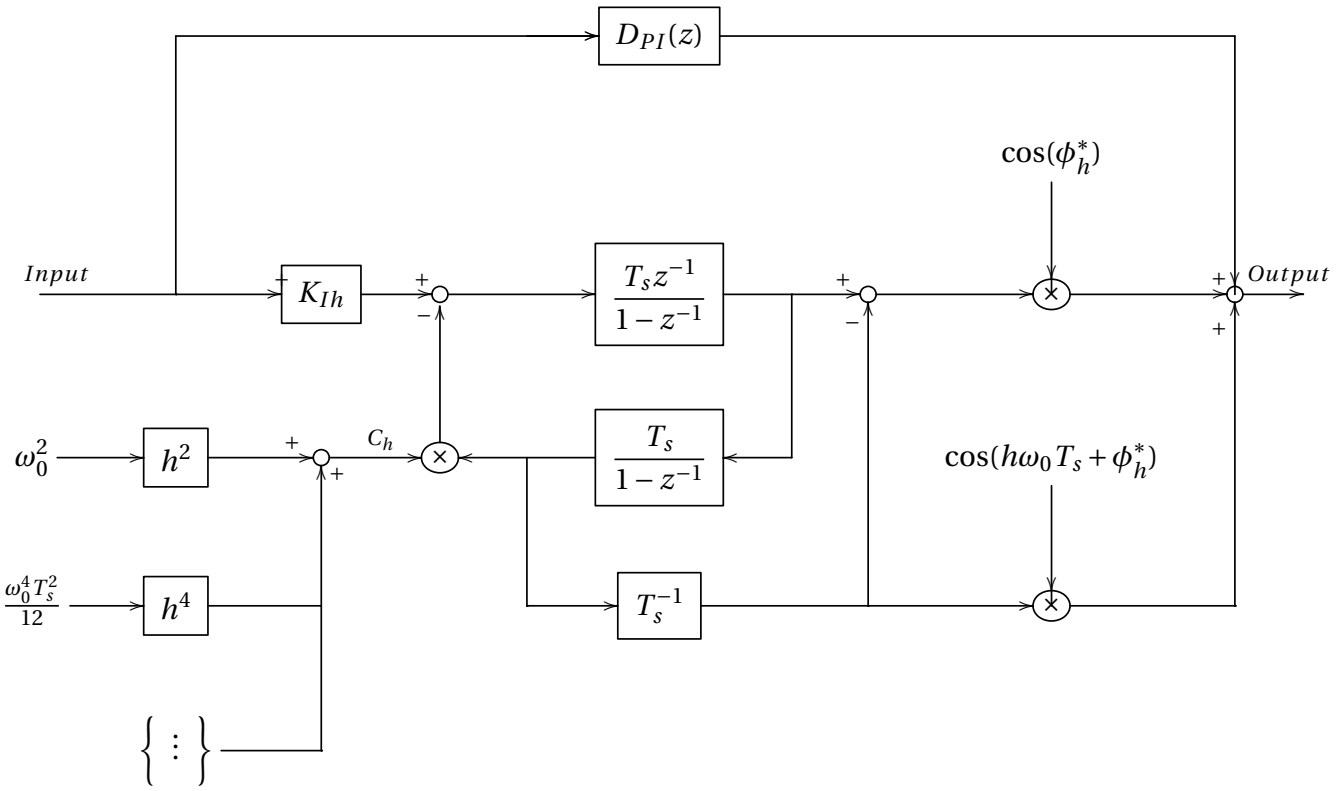

Figure 6.27: Block diagram of discrete-time implementation of a PIR controller, employing resonant terms with correction of poles and zeros, as well as reduced computational burden

A transfer function analysis was conducted for this current controller in the discrete z-domain. Below, bode diagrams are presented of the current control loop employing the controller of Equation (6.30) with tracking of the fundamental, as well as the 3rd, 5th, and 7th harmonic component. Due to the sensitivity of the controller, only the bode diagrams employing the complete plant transfer function is provided in this section.

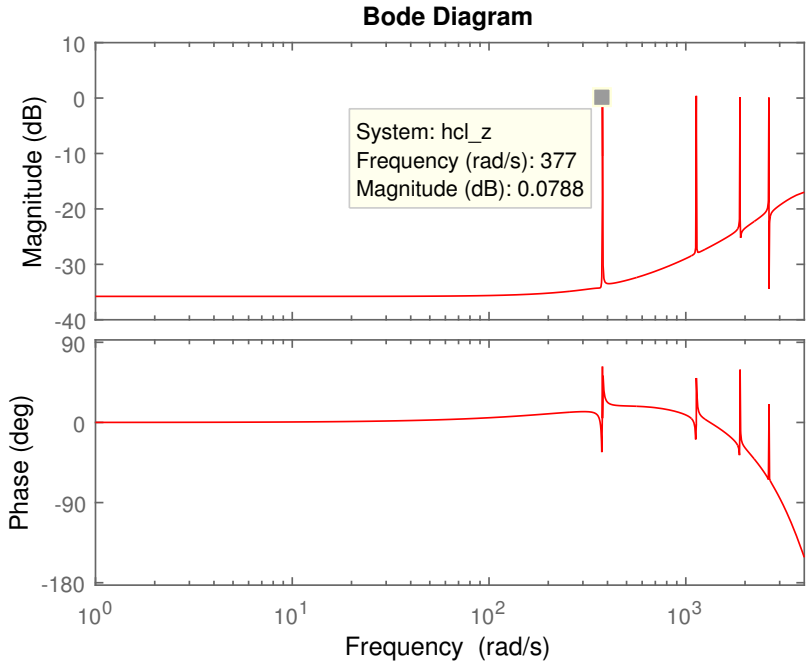

Figure 6.28: Bode plot of discrete closed loop system transfer functions with PIR current controller with tracking of h = 1, 3, 5, and 7

In the analysis of Figure 6.28, a sixth order Taylor approximation has been utilized for the pole correction term, C_h, using (4.28). For correction of zeros for the individual harmonic components, the target lead angle ϕ_h^* was selected according to (4.25). This bode plot verifies the infinite gains of the resonant terms as according to literature and indicates perfect tracking of the harmonic components of interest.

6.2 Outer Voltage Control Loop

In addition to the inner current control loop, an outer capacitor voltage loop is to be designed and implemented. Consequently, the AFE control system is to be a double cascaded one, composed of an outer filter capacitor voltage and inner inductor current feedback loop. By reducing the block diagram of the closed loop inner current controller of Figure 6.4 to a single transfer function, $h_{i,cl}(s)$, a system representation can be given as in Figure 6.29, in which $D_v(s)$ is a generic voltage controller.

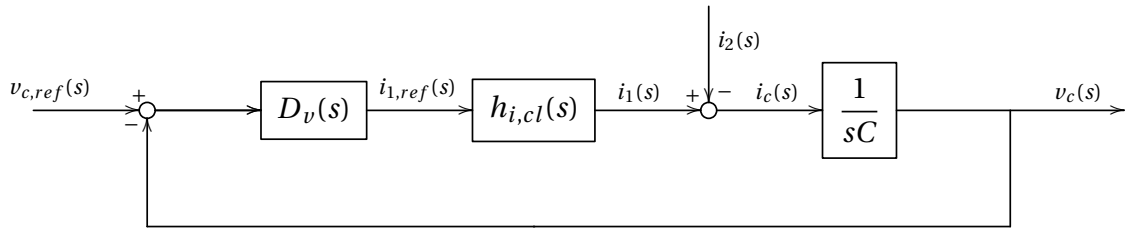

Figure 6.29: Simplified block diagram with closed loop capacitor voltage control

The controller selected for further study and implementation of outer voltage control is of type PIR multi-resonant with four band-pass filters for tracking of fundamental frequency component and with harmonic compensation of $h = 3,5,7$. This controller is selected due to its proven abilities for tracking of sinusoidal references in the stationary reference frame, as well as for providing a good design trade-off between harmonic attenuation and control processing load. It must be noted that the 3rd order harmonic compensation may be omitted by using delta connected filter capacitors which ensures effective cancellation of this component [25]. A complete overview of this control structure employed in the stationary $\alpha\beta$-reference frame is given in Figure 6.30, adapted from [39]. A bode diagram of the closed loop frequency response of the discretized $\frac{V_{c,ref}}{V_c}(z)$ is given in Figure 6.31, adapted from [39]. As for the PIR current controller of Figure 6.28, only the complete plant mode is regarded, due to parameter sensitivity.

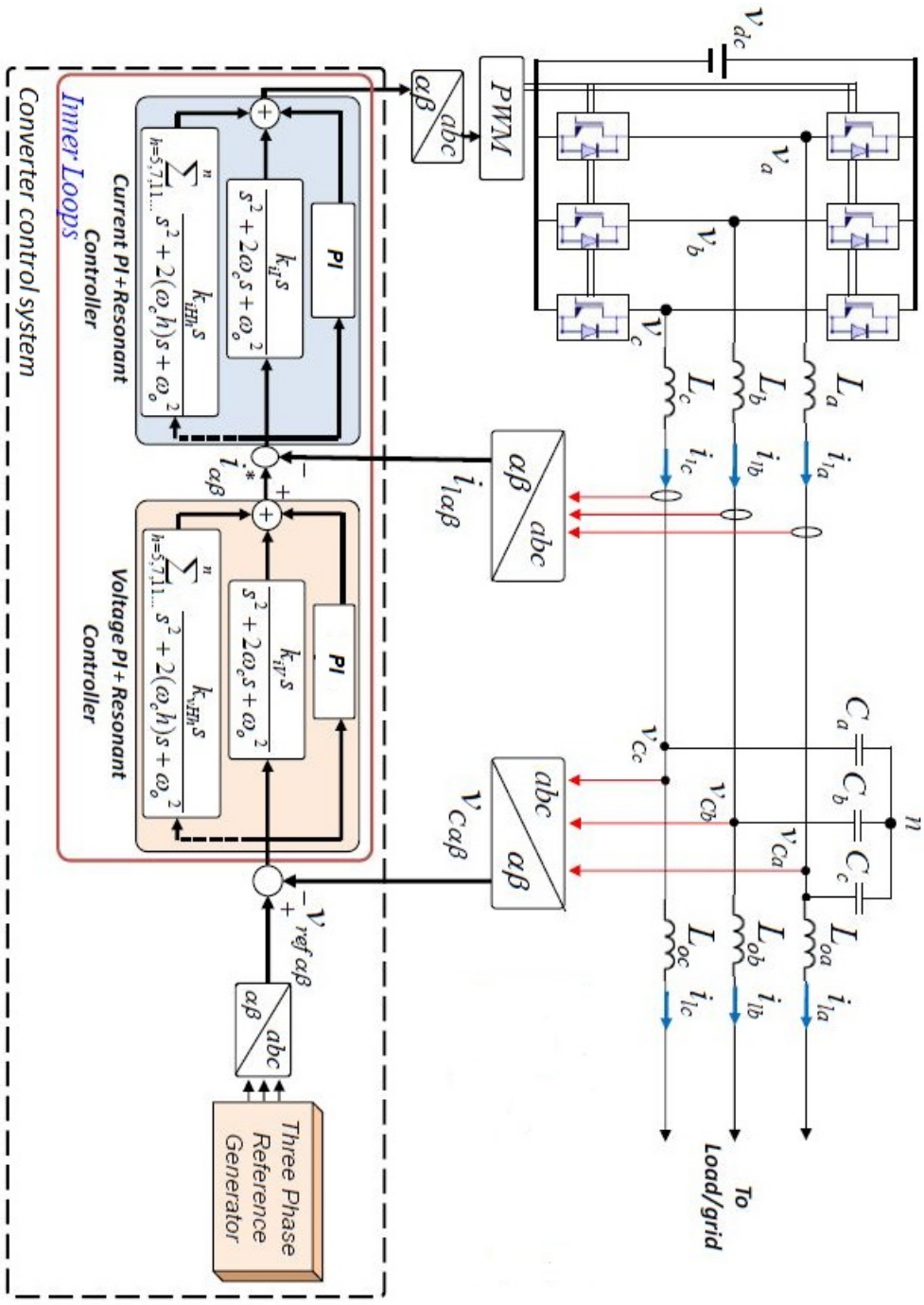

Figure 6.30: Double cascaded control system with PIR voltage- and current controllers with harmonic compensation, adapted from [39]

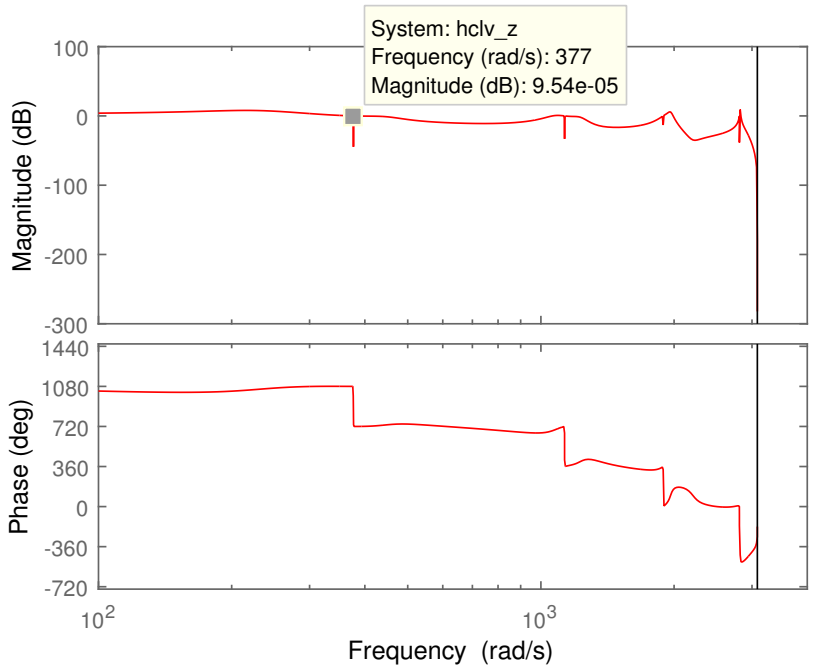

Figure 6.31: Frequency response of double cascaded control system with PIR multi-resonant voltage- and current controllers with tracking of h=1, 3, 5, 7

Figure 6.31 indicates resonance peaks at desired frequencies and satisfactory stability margins.

6.3 Summary of Chapter

In this chapter, a description has been provided of the procedure in which the AFE converter system is modeled and its associated control system designed, for simulation purposes. A block diagram system representation has been elaborated and different controllers have been designed based on tuning rules and transfer function analysis. Also, a discretized transfer function model employing PIR controllers haven been studied. In this work, two different system plant models have been considered, one *simple* and one *complete*. The controller performances have been evaluated and compared by studying their respective frequency and step responses. Based on the results presented throughout this chapter, an evaluation of the expected controller performance is summarized in Table 6.3. This evaluation is to compare the tracking abilities of the controllers with a sinusoidal reference of fundamental angular velocity of 377 rad/s. This anal-

ysis is performed in order to evaluate the precision and usability of the system transfer function representation related to the simulation results obtained later in Chapter 7. It must be remarked that, the general term, *perfect tracking*, that is used in Table 6.3, in this thesis refers to a tracking action of a sinusoidal reference without inherent phase and amplitude errors as well as a minimum noise amplification.

Table 6.3: Controller Tracking Performance With Fundamental Frequency Sinusoidal Reference Based On Transfer Function Analysis

Controller	Plant model	Associated bode plot Fig. no.	Sufficient closed loop stability margins, B	Amplitude error	Phase error	Perfect tracking
P	Simple	6.6	Yes	No	No	Yes
P	Complete	6.6	Yes	Yes	Yes	No
PI	Simple	6.10	Yes	No	No	Yes
PI	Complete	6.10	Yes	Yes	Yes	No
Parallel type PID	Simple	6.14	Yes	No	No	Yes
Parallel type PID	Complete	6.14	Yes	Yes	No	No
PID with limited derivative action	Simple	6.17	Yes	No	No	Yes
PID with limited derivative action	Complete	6.17	Yes	Yes	No	No
Double PI	Simple	6.20	Yes	No	No	Yes
Double PI	Complete	6.20	Yes	No	Minor	No
PR	Simple	6.23	Yes	No	No	Yes
PR	Complete	6.23	Yes	No	No	Yes
PIR	Simple	6.24	Yes	No	No	Yes
PIR	Complete	6.24	Yes	No	No	Yes
PIDR	Simple	6.25	Yes	No	No	Yes
PIDR	Complete	6.25	Yes	No	No	Yes
Double PI + R	Simple	6.26	Yes	No	No	Yes
Double PI + R	Complete	6.26	Yes	No	No	Yes
Discretized PIR with harmonic tracking of h=1,3,5,7	Complete	6.28	Yes	No	No	Yes
Double cascaded discretized PIR voltage- and current controllers with tracking of h=1,3,5,7	Complete	6.31	Yes	No	No	Yes

Chapter 7

Simulation Results

This Chapter presents the results obtained from simulations of a discretized three phase two-level AFE converter model with an output LC filter, the basis of the model indicated in Figure 7.1

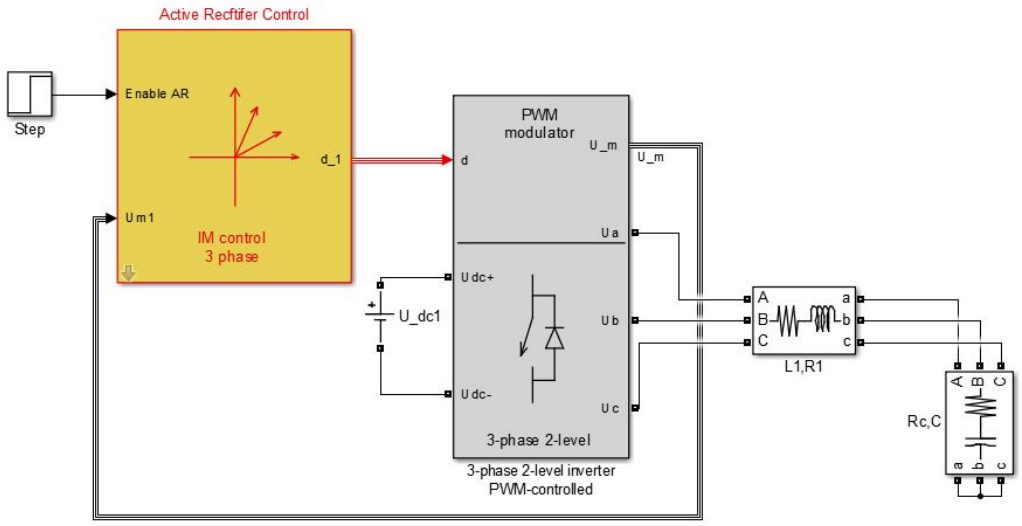

Figure 7.1: AFE rectifier simulation model

The transistors applied in the model are of type *metal–oxide–semiconductor field-effect transistor* (MOSFET), with anti-parallel diodes. The associated modulator is a sinusoidal PWM with third harmonic injection employing asymmetrical sampling.

Out of the controllers designed and studied in the transfer function analysis of Chapter 6, five of these are to be implemented in a simulation environment for further testing and study. In total,

seven cases are presented in this chapter for testing of these controllers in the stationary $\alpha\beta$-reference frame. The first five cases are considering current controllers, only, while in the last two, an outer voltage control loop is added, resulting in a double-loop cascaded control system. Out of these seven cases, the first four are mainly due to test the individual controller performances for tracking a sinusoidal reference signal of the fundamental frequency. However, in Cases 5 and 6, the ability of the multi-resonant controller for tracking of higher order harmonics is tested, as well. In Cases 6 and 7, a double-loop cascaded multi-resonant control system is examined, with Case 7 also including connection to a nonlinear load for testing of the harmonic compensation ability of this controller. In all cases, except for Case 7, the amplitude of the sinusoidal current reference is increased up to a value corresponding to approximately 0.1 pu. The tracking performances of the seven cases are reviewed, before a summary is provided in the end of the chapter, including a comparison of the simulation results to those of the controller design of Chapter 6.

It must be remarked, that the simulation results presented in this chapter are obtained by modifying a simulation model already containing the following basic system blocks, adapted from [48]:

- Converter block
- Task manager
- Repeating integrator
- Digital PI controller
- Digital PID controller
- THIPWM block, with corresponding Matlab s-function, simulating leg of the pwm-module, including nonlinear effects, such as blanking time and minimum turn-off time

7.1 Case 1: Proportional Current Controller

The first current controller to be implemented and tested in a simulation environment is the P type controller. The current control loop is depicted in Figure 7.2, displaying the current refer-

ence generator, the current measurement block, general $\alpha\beta$-current controllers, the THIPWM block, and the interrupt controller (task manager), this model being the "Active Rectifier Control" subsystem of Figure 7.1.

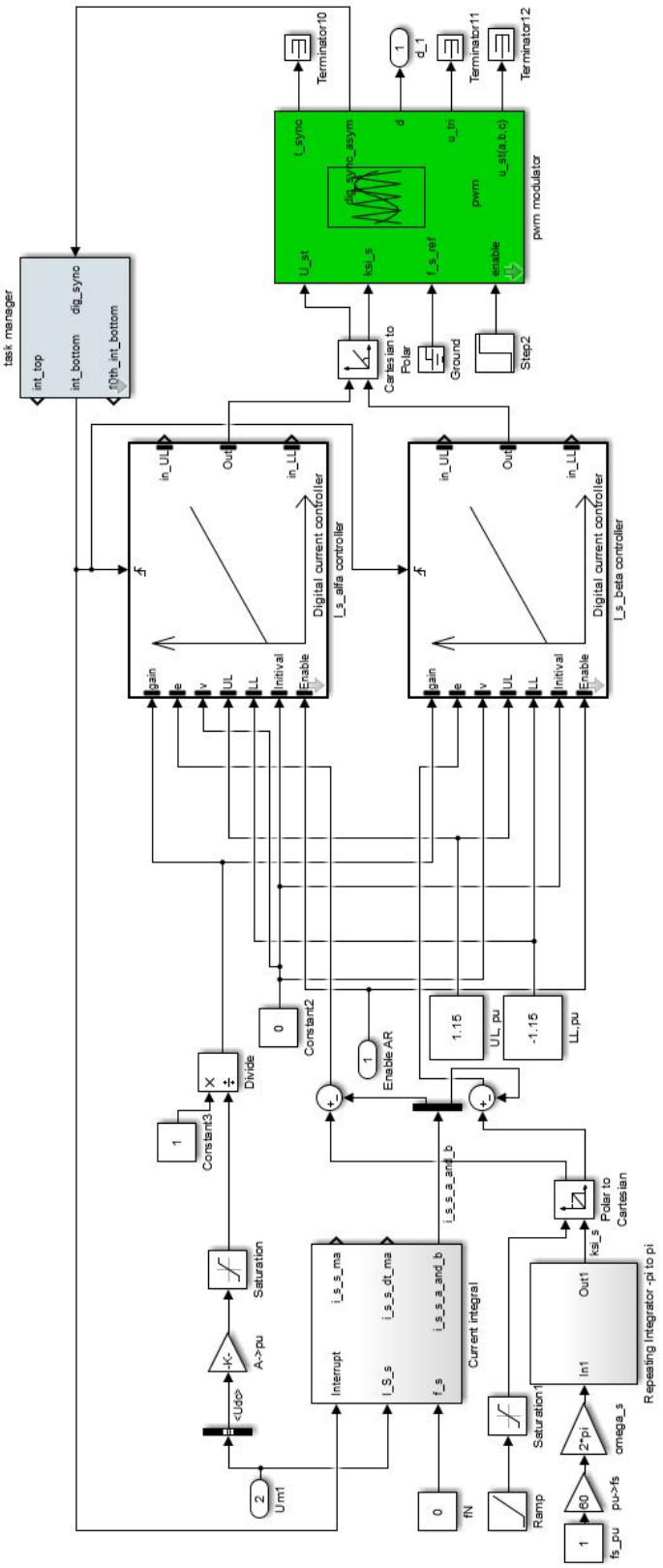

Figure 7.2: Simulation model of inner current control loop

The simulation result of the alpha current tracking performance of the proportional current controller is displayed in Figure 7.3.

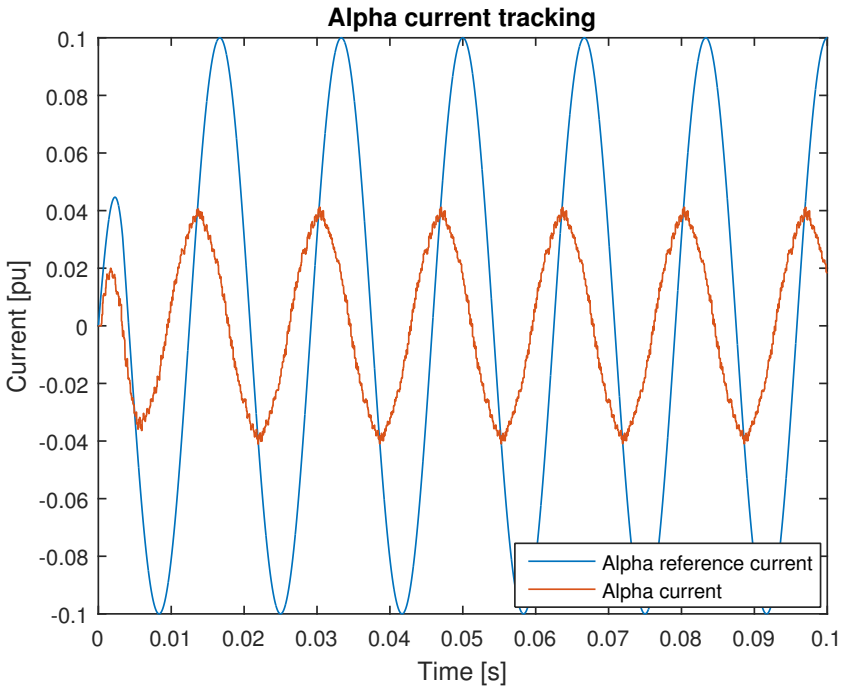

Figure 7.3: Tracking performance of P current controller

7.2 Case 2: PI Current Controller

The simulation result of the alpha current tracking performance of the proportional integral current controller is showed in Figure 7.4.

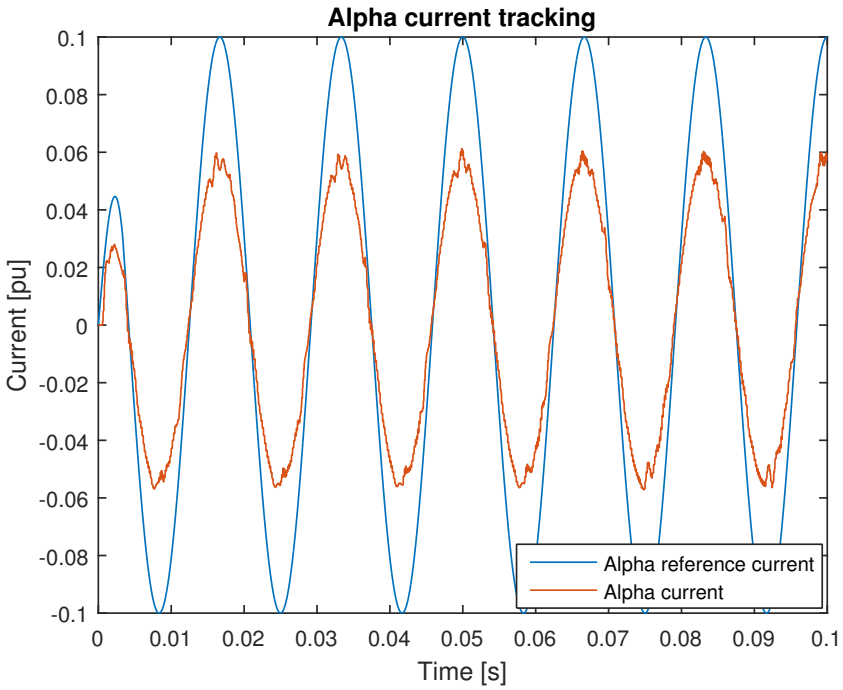

Figure 7.4: Tracking performance of PI current controller

The observed noise amplification quickly rises with an increase of the controller proportional gain. A further increase of the gain compromises stability, and eventually results in uncontrolled oscillations.

7.2.1 PI Current Controller with Feed-Forward Compensation

A simulation model is also developed for investigating the effect of including a capacitor voltage feed-forward compensation scheme along with the PI current controller. Considering Equation (6.1), of the passive LC filter, this corresponds to reducing the transfer function of the converter output into that of a simple RL circuit. The simulation results of the alpha current tracking performance of the proportional integral current controller with capacitor voltage feed-forward compensation is shown in Figure 7.5.

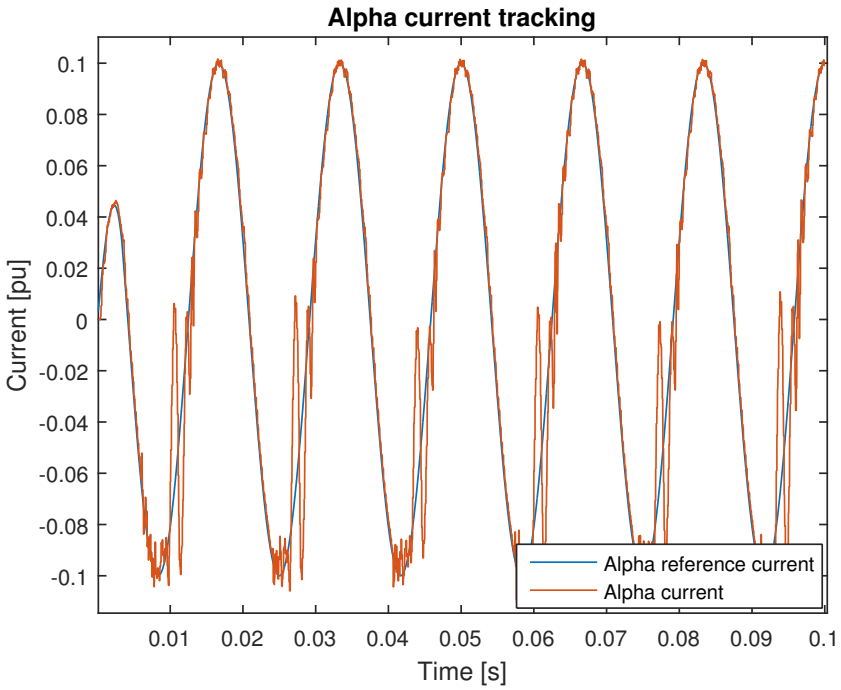

Figure 7.5: Tracking performance of PI current controller with capacitor voltage feed-forward

Compared to the case without capacitor voltage feed-forward, Figure 7.5 shows that the proportional gain can be increased to such a level that the amplitude error is removed without compromising stability. However, a periodic noise amplification can be observed, this being due to a higher order voltage frequency component that is amplified through the feed-forward gain.

7.3 Case 3: PID Current Controller with Limited Derivative Action

The simulation result of the alpha current tracking performance of the proportional integral current controller with limited derivative action is indicated in Figure 7.6.

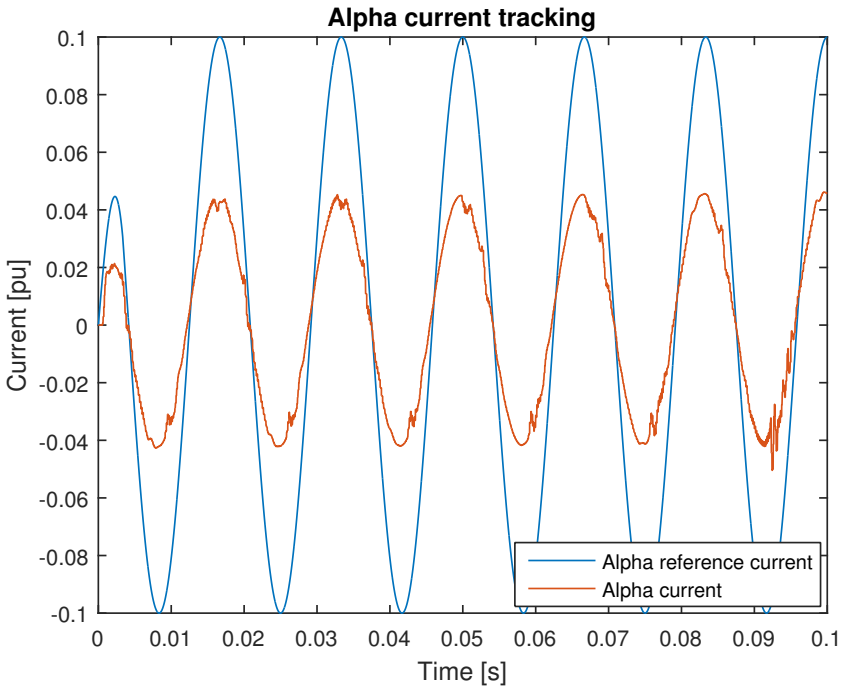

Figure 7.6: Tracking performance of PID current controller

Figure 7.6 indicates an amplitude error of about 50 %. The proportional gain of the PID controller must be limited in order to avoid noise amplifications, compromising the system stability.

7.3.1 PID Current Controller with Feed-Forward Compensation

The simulation results of the current tracking performance of the proportional integral derivative current controller with the addition of voltage feed-forward, is indicated in Figure 7.7.

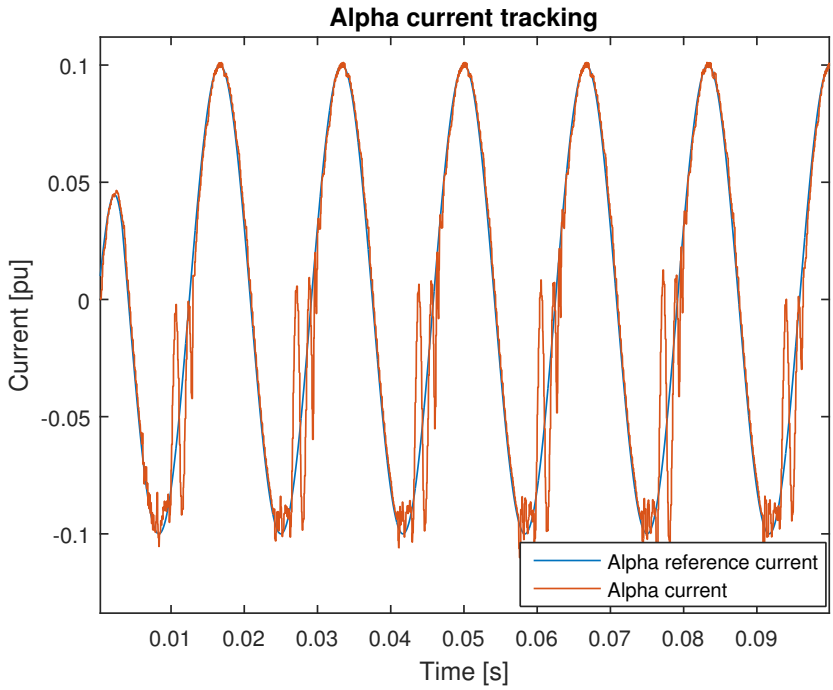

Figure 7.7: Tracking performance of a PID current controller with capacitor voltage feed-forward compensation

Compared to the case without capacitor voltage feed-forward of Figure 7.6, Figure 7.7 shows that the proportional gain can be increased to such a level that the amplitude error is removed without compromising stability. These trends are similar to those observed in Case 2 for the PI current controller with, and without voltage feed-forward compensation.

Another result to notice from the simulations where voltage feed-forward is utilized, is the DC-offset that is present in the converter output voltage. This result is shown in Figure 7.8.

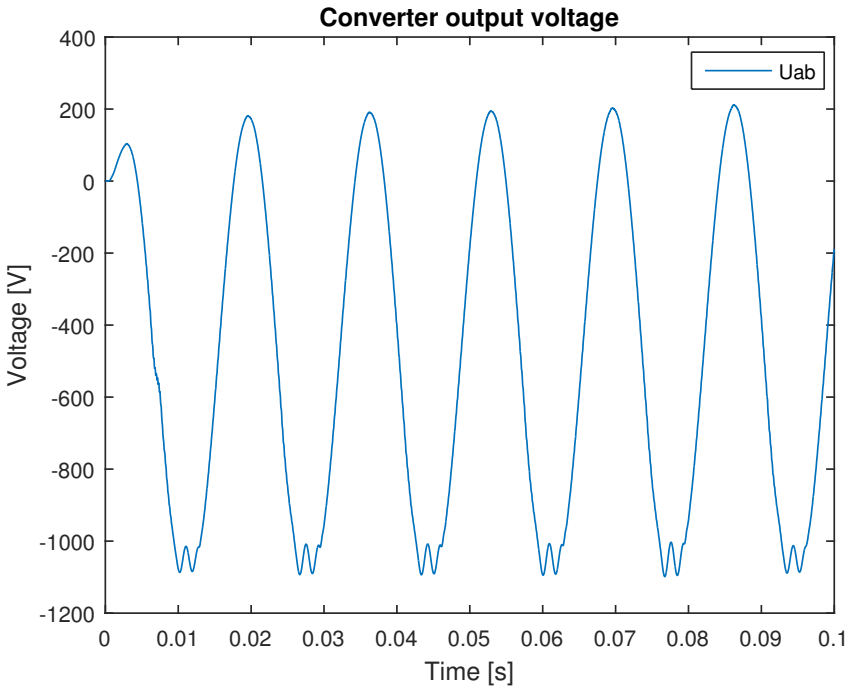

Figure 7.8: Converter output voltage employing PID current controller with capacitor voltage feed-forward compensation

7.4 Case 4: Double PI Current Controller

Figure 7.9 shows the simulation results of the alpha current tracking performance of the double proportional integral controller. The digital controller implementation is equivalent to the one given by 6.29 in the continuous frequency domain, with two integral time constants, and a single proportional gain.

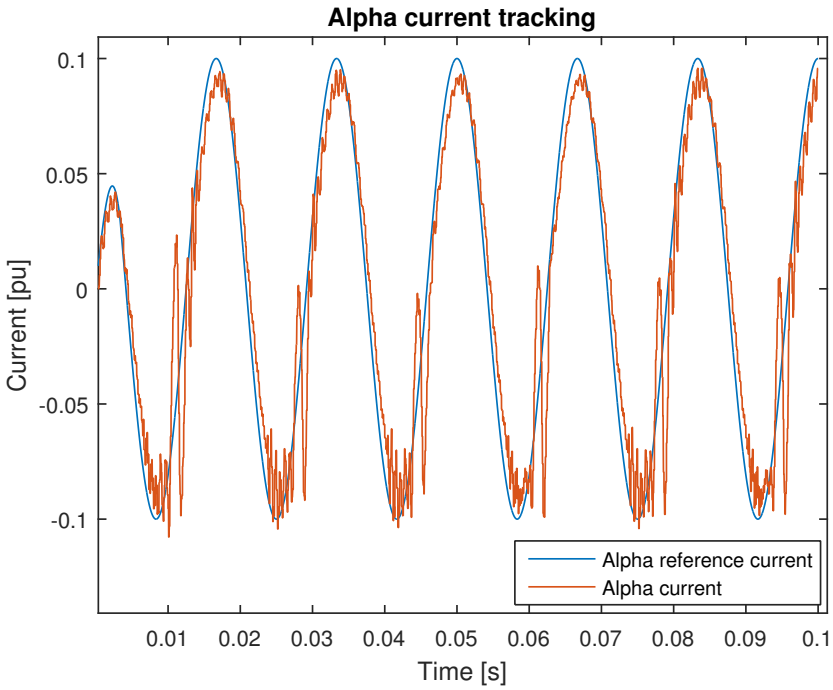

Figure 7.9: Tracking performance of a double PI current controller

This result indicates minor phase and amplitude errors as well as noise amplification due to a relatively high proportional gain. Overall, a better tracking performance is observed with the double PI controller compared to those of the PI and PID current controllers without voltage feed-forward compensation.

7.5 Case 5: PI + (Multi)-Resonant Current Controller

Figure 7.10 shows the simulation results of the fundamental alpha current tracking performance of the proportional integral + multi-resonant current controller with compensation of, $h = 3, 5, 7$. The controller implementation is the discrete one given by Equation (6.30) and the block diagram of Figure 6.27.

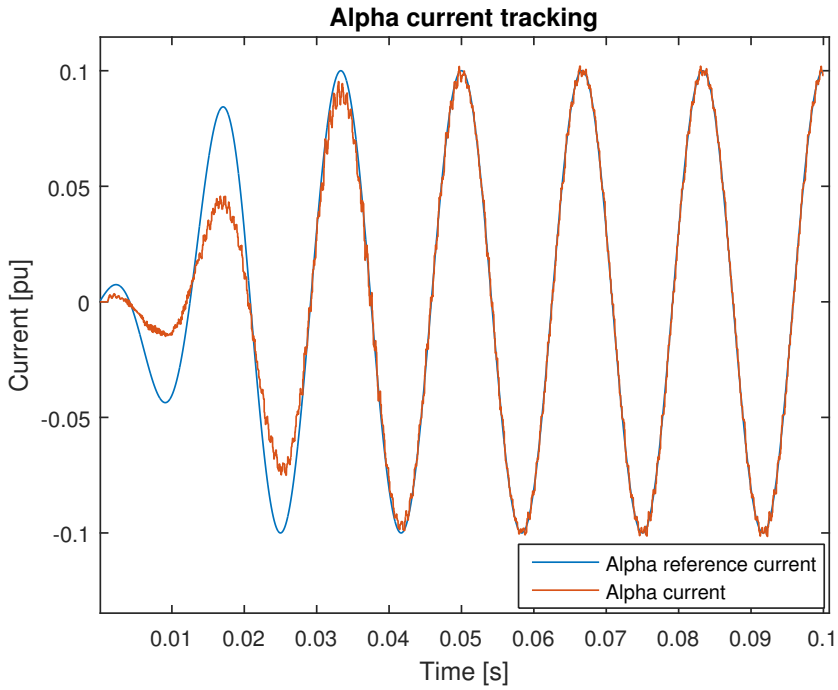

Figure 7.10: Tracking performance of a PIR current controller with harmonic compensation of h=3, 5, 7

Also, the effects on the individual harmonic components of the inductor current and the capacitor voltage are displayed in Tables 7.1-7.2, with and without compensation, respectively.

Table 7.1: Harmonic Performance Of Relevant Components Without Harmonic Compensation

	h = 3	**h = 5**	**h = 7**	**THD [%]**
Current magnitude (% of fundamental)	0.006	0.6	0.9	39.08
Voltage magnitude (% of fundamental)	0.007	0.12	0.13	0.31

Table 7.2: Harmonic Performance Of Relevant Components With Compensation Of h = 3, 5, 7

	h = 3	**h = 5**	**h = 7**	**THD [%]**
Current magnitude (% of fundamental)	0.01	0.18	0.03	39.06
Voltage magnitude (% of fundamental)	0.006	0.035	0.003	0.25

Tables 7.1-7.2 indicate that the compensation scheme of $h = 5$ and $h = 7$ effectively reduces the harmonic content of these components, while $h = 3$ is less affected. However, the THD is less affected, meaning that the harmonic compensation results in an increased content of higher order harmonics. This can be observed by considering the complete harmonic spectrum, provided in Appendix C.1. Moreover, these results imply that the capacitor voltage complies with the IEEE standard 519 with and without harmonic compensation, while the current does not, in any of the two cases.

In order to further investigate the effect of the harmonic compensation scheme, simulations were performed to examine the tracking properties of the components to be compensated for. Results of the tracking of a sinusoidal reference with frequency corresponding to the 7th harmonic component, ($f = 420$ Hz) is given in Figure 7.11.

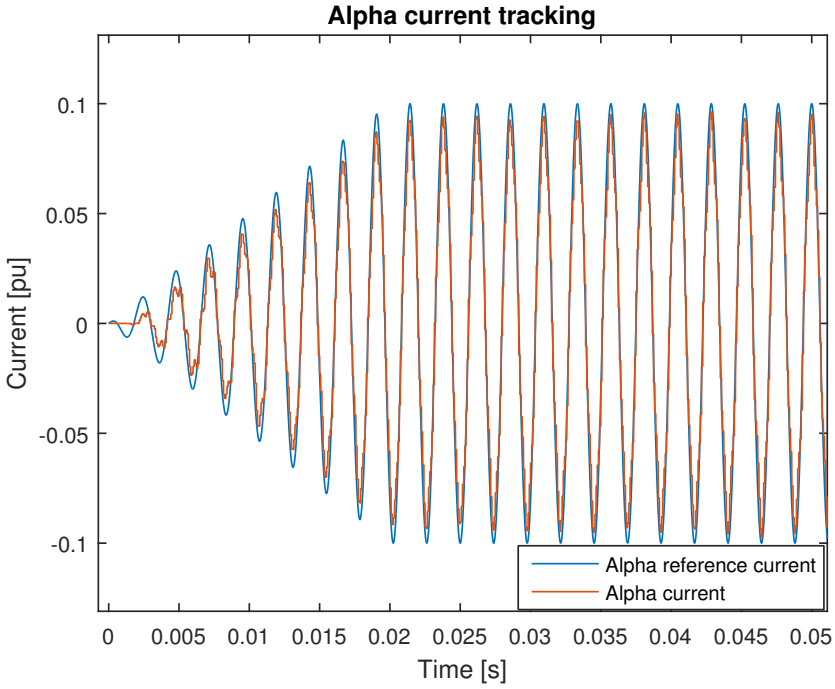

Figure 7.11: Tracking performance of a PI + multi resonant current controller following a sinusoidal reference with frequency of 420 Hz

Figure 7.11 verifies the tracking ability of the additional resonant terms. The small amplitude error that can be seen is eventually removed. Considering the harmonic performance of this simulation, it is found to be very similar to the one observed in Case 5 with the single loop control system, with detailed spectrum of the inductor current and capacitor voltage provided

in Appendix C.2.

7.6 Case 6: Double Loop PI + Multi-Resonant Control

This case examines the effect of including an outer PI + multi-resonant voltage control loop in addition to the inner current control loop of Case 5. The control implementation is in accordance to the double loop cascaded structure described in Section 6.2, Figure 6.30, with simulation model shown in Appendix C.2.

The resulting simulation tracking performance of the fundamental alpha components of the current and voltage controllers are presented in Figures 7.12-7.13, respectively.

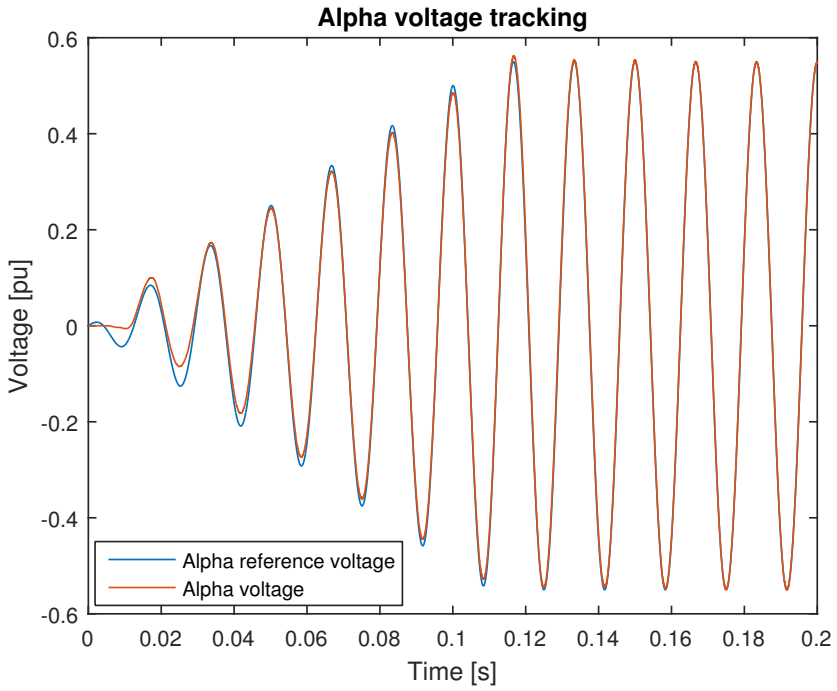

Figure 7.12: Performance of outer PI + multi-resonant voltage controller tracking a sinusoidal fundamental frequency reference

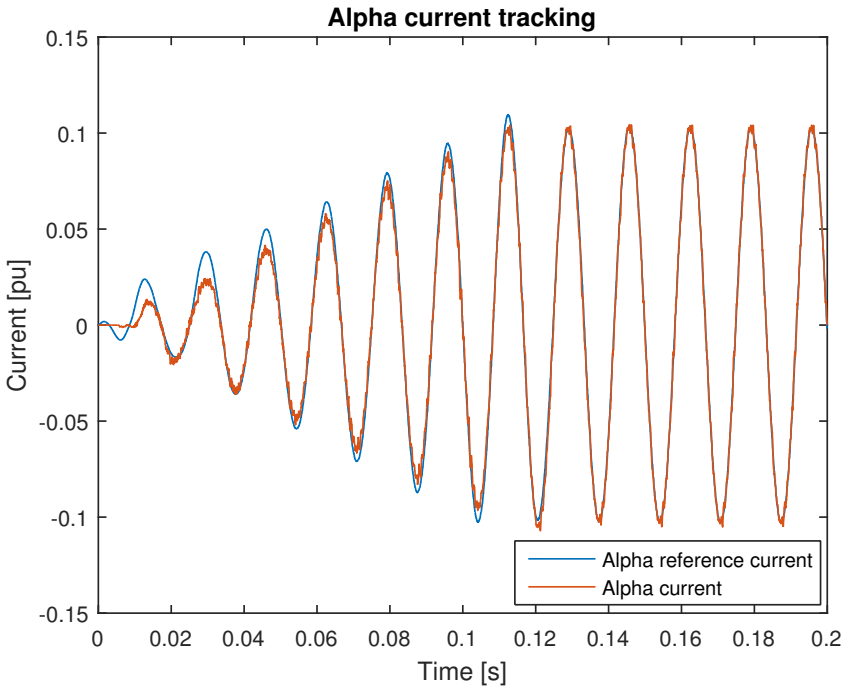

Figure 7.13: Tracking performance of inner PI + multi-resonant current controller

These figures indicate a settling time for both controllers of about 0.12 seconds before perfect tracking is obtained.

7.7 Case 7: Double Loop PI + Multi-Resonant Control with Diode Rectifier Bridge

In this case, the AFE converter is connected to a nonlinear load to test the ability of the controllers to compensate for the generated harmonics. The selected nonlinear load is the three-phase six-pulse diode rectifier bridge, described in Section 5.3. The diode rectifier is connected to an ideal current source, as indicated in Figure 7.14, displaying the load model of the simulation. The load is connected through an inductor on the output of the LC filter as indicated in Figure 6.30.

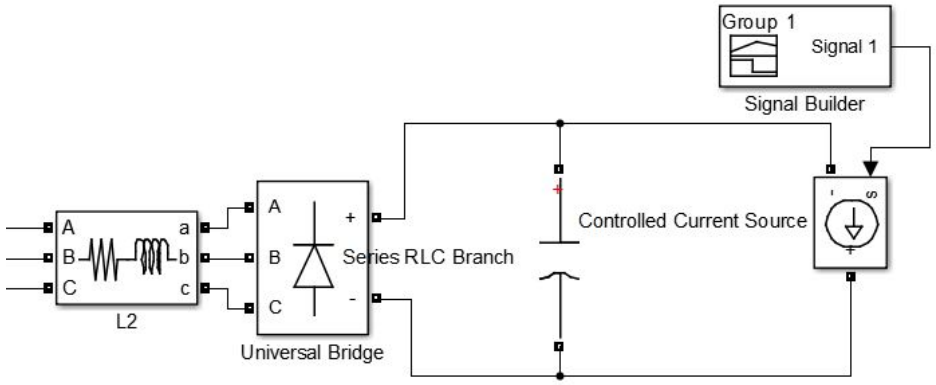

Figure 7.14: Simulation diode rectifier load model

This load will hence test the controllers to see if they are able to maintain a sinusoidal capacitor voltage. The trajectory of the ideal current source set by the signal builder block, is to be sloped up after 0.1 seconds to a value of 400 A, as indicated in Figure 7.15

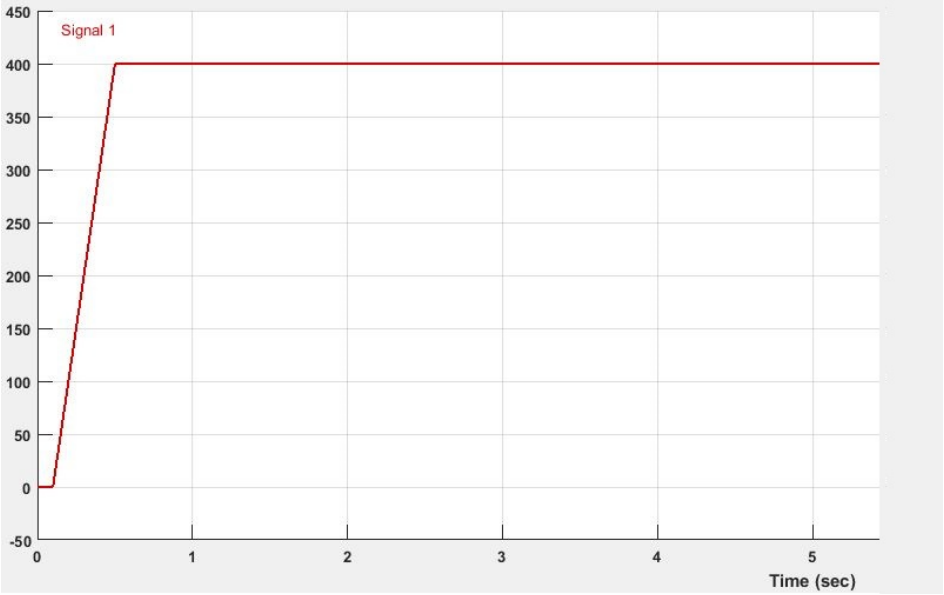

Figure 7.15: Trajectory of ideal current source

Applying this load to the AFE converter system, simulations were carried out of 4 seconds to test the compensation properties of the multi-resonant controllers. The results of the responses, as well as the detailed tracking performances as steady-state is reached, are showed in Figures 7.16 - 7.19, for the current-, and voltage controllers, respectively.

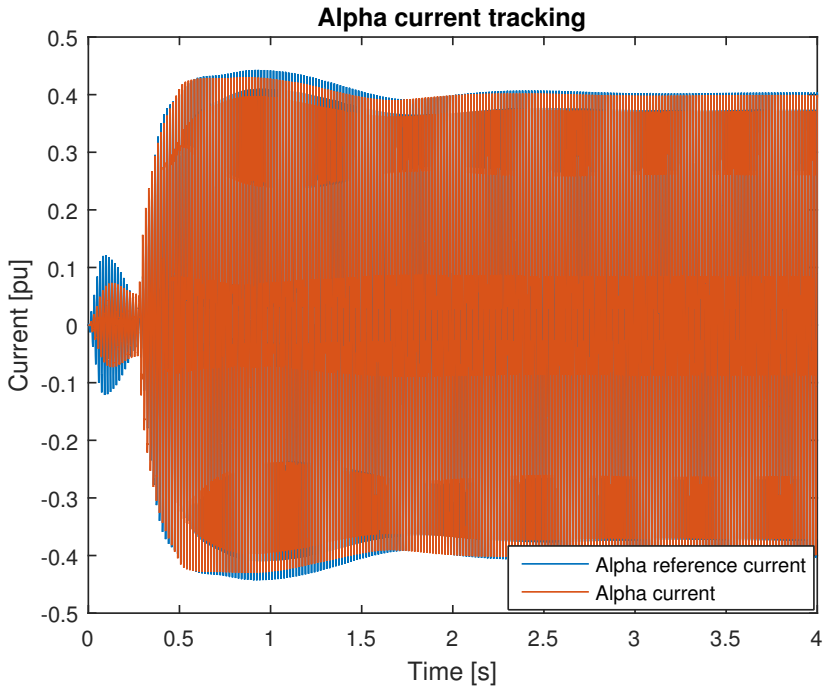

Figure 7.16: Tracking performance of inner PI + multi-resonant current controller with diode rectifier-load

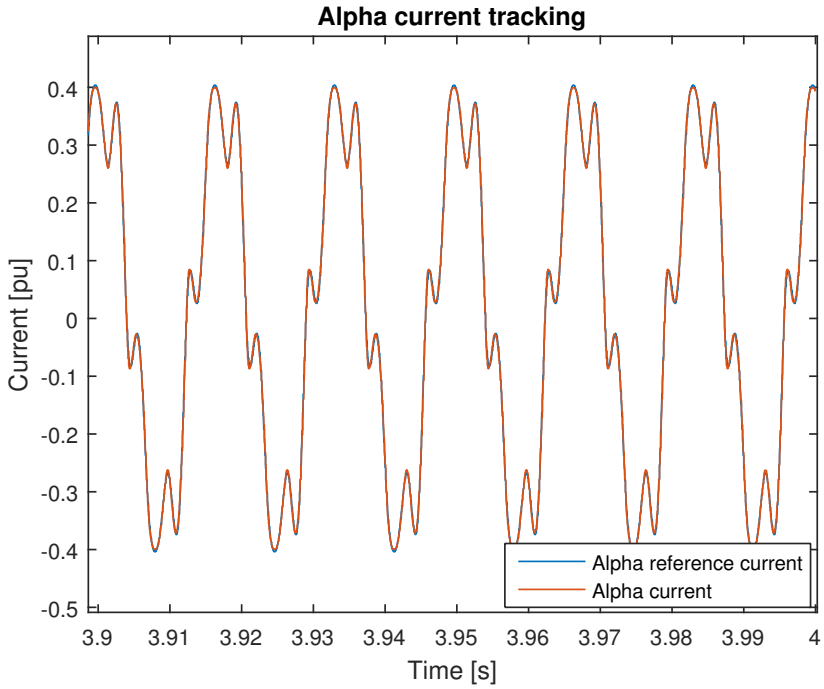

Figure 7.17: Detailed tracking performance of inner PI + multi-resonant current controller with diode rectifier-load

Considering the current controller performance, Figure 7.16 clearly indicates the contribution from the diode bridge as it is sloped up, starting from 0.1 second. Figure 7.17 indicates that after the system is stabilized, perfect current reference tracking is obtained, even with the distorted contribution of the nonlinear load.

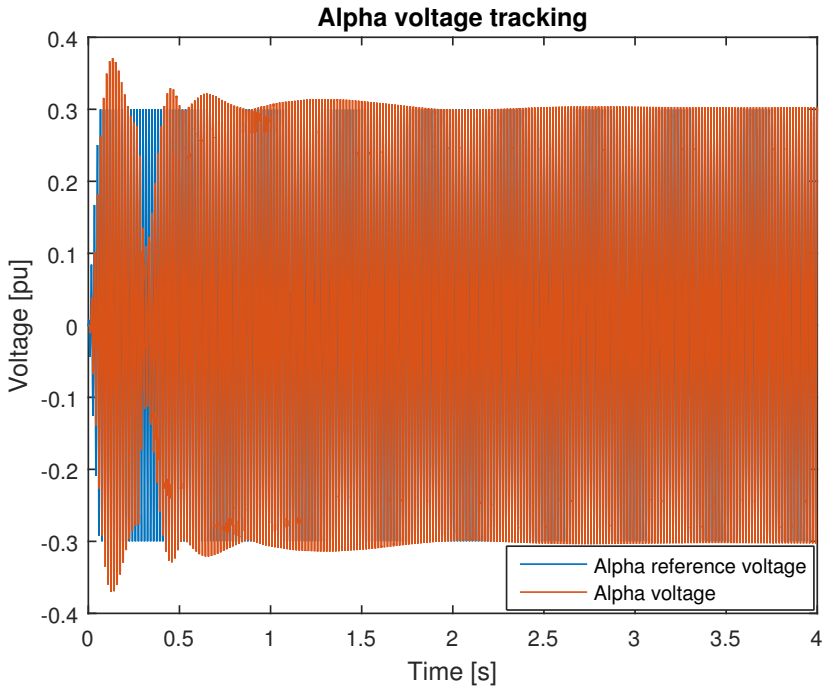

Figure 7.18: Tracking performance of outer PI + multi-resonant voltage controller with diode rectifier-load

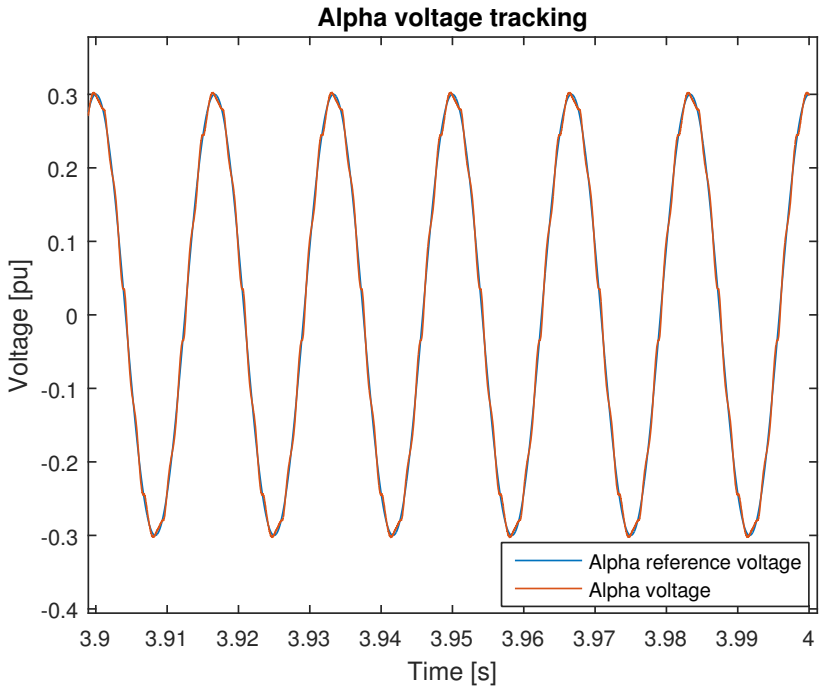

Figure 7.19: Tracking performance of outer PI + multi-resonant voltage controller with diode rectifier-load

When studying the performance of the voltage controller of Figures 7.18-7.19, a similar trend can be seen as for the current. The detailed voltage tracking of Figure 7.19, not only indicates perfect tracking, but also indicates that a fairly sinusoidal capacitor voltage is maintained, even with the addition of the diode-rectifier bridge. This is also verified through the FFT analysis, whose results given in Table 7.3, where the voltage is kept within the harmonic limits of IEEE std. 519, while the converter output current is not.

Table 7.3: Harmonic Performance Of Relevant Components With Harmonic Compensation And Noninear Load

	h = 3	**h = 5**	**h = 7**	**THD [%]**
Current magnitude (% of fundamental)	0	25	8.4	27.3
Voltage magnitude (% of fundamental)	0.005	0.025	0.030	3.69

7.8 Summary of Chapter

In the same manner as in Chapter 6, a summary is given of the tracking performance of the individual controllers based on the simulation results provided throughout this chapter. Table 7.4 evaluates the controller tracking performances observed in this chapter. Table 7.5 compares these simulation results with the results of the controller design and transfer function analysis, of Chapter 6, summarized in Table 6.3. The simulation results of this chapter are compared to both the results of the complete-, and the simplified plant models of Chapter 6, in order to evaluate their individual model accuracies.

Table 7.4: Controller Tracking Performance With Fundamental Frequency Sinusoidal Reference Based On Simulation Results

Controller	Case	Fig. no.	Noise amplification	Amplitude error	Phase error	Perfect tracking
P	1	7.3	No	Yes	Yes	No
PI	2	7.4	Yes	Yes	No	No
PI with feed-forward	2	7.5	Yes	No	No	No
PID with limited derivative action	3	7.6	Yes	Yes	No	No
PID with feed-forward	3	7.7	Yes	No	No	No
Double PI	4	7.9	Yes	Minor	Minor	No
PIR with tracking of h=1,3,5,7	5	7.10	No	No	No	Yes
Double cascaded PIR voltage- and current controllers with tracking of h=1,3,5,7	6	7.12-7.13	No	No	No	Yes
Double cascaded PIR voltage- and current control with tracking of h=1,3,5,7 with a non-linear load	7	7.16-7.19	No	No	No	Yes

Based on the results summarized in Table 7.4, perfect tracking is obtained for Cases 5-7, employing resonant controllers. The tracking properties are fairly good for the PI-, and PID current controllers with voltage feed-forward compensation, of Cases 2-3, but a considerable noise amplification is observed. Only minor errors, as well as some noise amplification is observed for the double PI controller of Case 4.

Table 7.5: Comparison Of Observed Simulation Tracking Performance And Expected Performance Based On Controller Design And Transfer Function Analysis Of Table 6.3

Controller	**Case**	**Fig. no.**	**Same simulation tracking results as in transfer function analysis with *simplified* plant model**	**Same simulation tracking results as in transfer function analysis with *complete* plant model**
P	1	7.3	No	Yes
PI	2	7.4	No	Yes
PID with limited derivative action	3	7.6	No	Yes
Double PI	4	7.9	No	No, due to minor simulation amplitude error
PIR with tracking of h=1,3,5,7	5	7.10	Yes	Yes
Double cascaded PIR voltage- and current controllers with tracking of h=1,3,5,7	6	7.12-7.13	Yes	Yes
Double cascaded PIR voltage- and current control with tracking of h=1,3,5,7 with a non-linear load[1]	7	7.16-7.19	-	-

[1]Case 7 was not examined in the transfer function analysis

Considering Table 7.5, and the validity of the two plant models from Chapter 6, it can be

observed, that the controller design results based on the *complete* transfer function model, coincides with the tracking properties obtained through the simulation cases. Only, a minor inconsistency is obtained with the double PI current controller.

The controller design based on the *simplified* plant transfer function model, on the other hand, anticipates perfect tracking for all simulation cases, which only coincides with the simulation results for Cases 5 and 6 were resonant controllers are utilized.

Chapter 8

Summary and Further Work

In this final chapter, a summary is given on the findings and results obtained throughout this thesis. The results are evaluated and discussed, and recommendations for further work are provided.

8.1 Summary and Conclusions

In this thesis, literature has been considered for investigating the operation and possible system implementations of an active front end converter along with its control system. The state-of-art for this type of power electronic system was first presented in Chapter 2, in accordance to the first of the four objectives of this thesis, given in Section 1.2. The second objective was met in Chapters 3, and 4, considering the background theory of the converter operation and modeling, and possible control system implementations, respectively. Background theory on harmonics as well as design of the output passive LC filter was provided in Chapter 5. In Chapter 6, a system model was developed in the continuous frequency domain. Two different plant transfer function representations were considered, one complete and one simplified. Eight different current controllers were further studied and designed considering these models. Out of these controllers, a discretized model of the proportional integral + multi-resonant controller was derived, and a double loop cascaded control system has been considered, employing this controller. Hence, the third objective of Section 1.2 was met in Chapter 6. Furthermore, in Chapter 7, a discretized simulation model was developed for controller evaluation and to aid controller

design. In total, seven cases have been implemented and examined in a simulation environment. The inherent shortcomings of P, PI, and PID controllers for tracking of sinusoidal references in the stationary $\alpha\beta$-reference frame have been tested and verified, according to findings in literature. Better tracking results, without steady-state phase or amplitude deviations, were obtained when applying capacitor voltage feed-forward compensation together with the PI and PID current controllers. Undesired amplification of voltage harmonics could, however, be observed with the implementation of this scheme. A similar tracking performance was observed with the double PI current controller, however, also including a minor phase error. Successful tracking performance was achieved using a single loop PI (+ multi-resonant) current control system, and with a double loop cascaded control system including voltage control, also employing this type of controller. Moreover, the ability of resonant harmonic compensation has been verified in the simulation environment, using PI + multi-resonant controllers, with successful tracking of sinusoidal references of higher order relevant harmonic frequencies, as well as with the compensation of a nonlinear diode rectifier-bridge load. The preliminary results of this thesis, thus show a significantly better performance on frequency tracking, utilizing resonant controllers, as opposed to conventional linear PI and PID controllers when employed in the stationary $\alpha\beta$-reference frame. Based on the results obtained from the controller design and simulation process, the complete transfer function model proved to a be a good system representation, its results coinciding with all but one of the relevant cases tested in the simulation model. The simplified transfer function model proved not to be a good model approximation in these cases where tracking performance of the fundamental frequency component was emphasized. With these results in mind, the fourth and final objective regarding controller evaluation in a simulation environment was achieved.

8.2 Discussion

Here, some of the findings of this report are discussed in order to evaluate their validity, strengths, and limitations.

One of the topics that is natural to discuss of this report, is the validity of the controller de-

sign performed in Chapter 6. In this regard, a question that is relevant to ask, is: "Is it sufficient to tune these controllers according to low frequencies, or should higher frequencies be considered as well?" Being a system containing small time constants, the current control needs to be quick in order to damp out the oscillations of the RL components. This is certainly not an easy control task, its challenge may be illustrated by means of a simple analogy, considering the equivalence between a motor drive and the control of the system treated in this thesis. In this analogy, the capacitor voltage of the LC filter can be treated as equivalent to the self-induced voltage of an electrical machine. The mechanical motor contains a rotating mass, and, thus, possesses inertial properties, making it naturally suitable for handling transients. The AFE converter, on the other hand, lacks this physical inertia, making it more prone to fast oscillations, that in turn needs to be taken care of by its associated control system. With this in mind, stable operations and frequency being paramount in the electric system, controllers of this converter system should undoubtedly also be able to handle higher order disturbances. However, the controller tracking properties have been those emphasized in this study, and regarding reference tracking ability, the most important feature of the voltage and current controllers, is deemed to be their ability to track the lower grid-fundamental frequency sinusoidal component. This seems evident, especially considering the design process of Chapter 6, in which the simplified plant model was considered. The described simplification was seen in several references for controller tuning purposes, in which tuning strategies such as the modulus, and symmetrical optimum were applied. It is therefore of interest to investigate the validity of this simplification. As discussed in Chapter 6, and seen in Figure 6.5, the two plant representations indicate similar responses at higher frequencies, more specifically, at frequencies $> 10^4$ rad/s. This behavior of the two system representations is later verified through the open- and closed loop frequency responses shown in the bode diagrams of the individual current controllers. Moreover, the unity step responses of the P, PI, and PID current controllers indicate deviant results for the two system representations, again verifying the limited application of the simplified one regarding reference tracking performance. Finally, in the comparison of the results of Chapter 7 and 6, the tracking performance observed in the simulation environment almost perfectly coincided with those based on the design process using the complete transfer function model. Based on the controller design using the simplified model, perfect tracking were anticipated for

all the simulation cases, which proved only to coincide with the cases employing resonant control. With these results, it appears that the simplified system representation at best can be used as a starting point in controller tuning for fundamental frequency-reference tracking purposes. However, the validity of the simplification is to increase with increased frequencies, and may form a satisfactory basis for controllers to be tuned for tracking of higher order harmonics, as well as for higher order disturbance rejection purposes.

In the Cases 2 and 3 of Chapter 7, examining the effect of feed-forward compensation of the converter capacitor voltage, the results of this control scheme yield better reference tracking properties compared to the cases without voltage feed-forward. These two cases, however, gives rise to another challenge, as line-voltage distortions are amplified in the feed-forward, causing increased oscillations observed in the converter output currents. These harmonics are observed along with a DC-offset of the converter output voltage, indicated in Figures 7.8, as the modulator reaches a state of saturation. Two possible ways that could have been tested for removal of the observed DC-offset, is by means of, either a DC-offset controller, or the outer voltage control loop.

Regarding Case 7, dealing with harmonic compensation of a nonlinear load, the ability of the resonant controllers were tested, and the results appear to verify the properties as described in literature. These results indicate a significant improvement of the system harmonic components to be compensated for. Considering the total harmonic distortion, on the other hand, this is kept more or less unchanged, indicating that the compensation scheme forces the harmonic content higher up in the frequency spectrum. It would therefore be of interest to study the harmonic performance that could be achieved by a further extension of the control system, integrating virtual impedance and active damping functionality in addition to the compensation.

The preliminary results of this thesis show a significantly better performance on frequency tracking, utilizing resonant controllers, as opposed to conventional linear PI and PID controllers

employed in the stationary reference frame. However, it must be emphasized that this is just an initial study, with many simplifications, which may lead to inaccuracies and anomalies when implemented in a real case. Some of the most prominent sources of inaccuracies, include those of human errors and simplifications of the real-world that are due to occur when working in a simulation environment. Other possible mathematical errors include the likes of discretization, round-off, and blanking time, and nonlinear behavior of the transistor switching operations.

8.3 Recommendations for Further Work

Here, recommendations are given to possible extensions of the work presented in this report. The recommendations are classified as:

- **Short-term:** Extending the simulation model by adding virtual impedance and active damping functionalities and study the effect on the system's harmonic performance when connected to a nonlinear load. Implementation of PIR controller in a laboratory environment for verification of the results obtained through the simulations of this thesis, is also recommended.
- **Medium-term:** Small-scale implementation of the converter system employing PI + multi-resonant controller in a laboratory environment for testing of its harmonic compensation capability. Testing of active damping and virtual inertia functionality is also encouraged, with the connection of a nonlinear load.
- **Long-term:** Testing of the harmonic compensation capability of a full-scale, grid-connected AFE inverter system employing multi-resonant current- and voltage controllers, active damping and virtual inertia functionalities. Coordination of several system of this type should also be implemented and tested.

Bibliography

[1] R. P. Burgos, E. P. Wiechmann, and J. Holtz, "Complex State-Space Modeling and Nonlinear Control of Active Front-End Converters", in *IEEE Transactions on Industry Applications*, vol. 52, no. 2, April 2005.

[2] Z. Song, Y. Tian, W. Chen, Z. Zou, and Z. Chen, "Predictive Duty Cycle Control of Three-Phase Active-Front-End Rectifiers", in *IEEE Transactions on Industry Applications*, vol. 31, no. 1, January 2016.

[3] W. Gullvik, "Modeling, Analysis and Control of Active Front End (AFE) Converter", Philosophiae doctor, Department of Electric Power Engineering, Norwegian University of Science and Technology, 2007.

[4] K. Jalili and S. Bernet, "Design of LCL Filters of Active-Front-End Two-Level Voltage-Source Converters", in *IEEE Transactions on Industrial Electronics*, vol. 56, no. 5, pp. 1674-1689, May 2009.

[5] Y. Chen, R. Hesse, D. Turschner and H. P. Beck, "Investigation of the Virtual Synchronous Machine in the Island Mode", in *2012 3rd IEEE PES Innovative Smart Grid Technologies Europe (ISGT Europe)*, Berlin, pp. 1-6, 2012.

[6] F. Hernàndez, L. Moràn, J. Espinoza, and J. Dixon, "A Multilevel Active Front-End Rectifier With Current Harmonic Compensation Capability", in *The 30th Annual Conference of the IEEE Industrial Electronics Society*, November 2-6, 2004, Busan, Korea.

[7] C. Liu, F. Zhao, G. Cai, N. Huang, J. Wang, and M. Wang, "Novel individual voltage balancing control scheme for multilevel cascade active-front-end rectifier", in *IET Power Electronics*, Vol. 7, Iss. 1, pp. 50–59, 2013

[8] M. Torres, and L. Lopes "Inverter-Based Diesel Generator Emulator for the Study of Frequency Variations in a Laboratory-Scale Autonomous Power System", in *Energy and Power Engineering*, vol. 5 No. 3, pp. 274-283, 2013.

[9] V. Blasko, and V. Kaura, "A Novel Control to Actively Damp Resonance in Input LC Filter of a Three-Phase Voltage Source Converter", *IEEE Transactions on Industry Applications*, vol. 33, no. 2, pp. 542-550, March/April, 1997.

[10] P. A. Dahono, Y. Sato and T. Kataoka, "Analysis and minimization of ripple components of input current and voltage of PWM inverters", in *IEEE Transactions on Industry Applications*, vol. 32, no. 4, pp. 945-950, Jul/Aug 1996.

[11] K. Taniguchi, Y. Ogino, and H. Irie, "PWM Technique for Power MOSFET Inverter", in *IEEE transactions on power electronics*, vol 3. no 3. July 1988.

[12] A. M. Massoud, S. J. Finney and B. W. Williams, "Control techniques for multilevel voltage source inverters", in *Power Electronics Specialist Conference, 2003. PESC '03. 2003 IEEE 34th Annual*, 2003, pp. 171-176 vol. 1.

[13] A. Iqbal, E. Levi, M. Jones, S. N. Vukosavic, "Generalised Sinusoidal PWM with Harmonic Injection for Multi-Phase VSIs", in *Power Electronics Specialists Conference, 2006. PESC '06. 37th IEEE*, Jeju, pp. 1-7, 2006.

[14] J. T. Boys and S. J. Walton, "A loss minimised sinusoidal PWM inverter", in *IEE Proceedings B - Electric Power Applications*, vol. 132, no. 5, pp. 260-268, September 1985.

[15] W. C. Duesterhoeft, M. W. Schulz and E. Clarke "Determination of Instantaneous Currents and Voltages by Means of Alpha, Beta, and Zero Components", in *Transactions of the American Institute of Electrical Engineers*, vol. 70, no. 2, pp. 1248-1255, July 1951.

[16] P. Rodriguez, R. Teodorescu, I. Candela, A. V. Timbus, M. Liserre, and F. Blaabjerg "New positive-sequence voltage detector for grid synchronization of power converters under faulty grid conditions", in *Power Electronics Specialists Conference, 2006. PESC'06. 37th IEEE*, pp. 1-7, 2006.

[17] A. Timbus "Grid monitoring and advanced control of distributed power generation systems", Phd. Aalborg University, May 2007.

[18] U. A. Miranda, L. G. B. Rolim and M. Aredes, "A DQ Synchronous Reference Frame Current Control for Single-Phase Converters", in *Power Electronics Specialists Conference, 2005. PESC '05. IEEE 36th*, Recife, 2005, pp. 1377-1381.

[19] C. Cai, L. Wang and G. Yin, "A three-phase active power filter based on park transformation", in *Computer Science and Education, 2009. ICCSE '09. 4th International Conference on*, Nanning, pp. 1221-1224, 2009.

[20] S. Bhattacharya and D. Divan, "Synchronous frame based controller implementation for a hybrid series active filter system", in *Industry Applications Conference, 1995. Thirtieth IAS Annual Meeting, IAS '95., Conference Record of the 1995 IEEE*, Orlando, FL, pp. 2531-2540, vol.3, 1995.

[21] J. G. Balchen, T. Andresen, and B. A. Foss (2003). *"Reguleringsteknikk"*. Institutt for teknisk kybernetikk, NTNU, Trondheim, 5th edition.

[22] G. Shen, D. Xu, L. Cao, and X. Zhu, "An Improved Control Strategy for Grid-Connected Voltage Source Inverters With an LCL Filter", in *IEEE Transactions on Power Electronics*, vol. 23, no. 4, pp. 1899-1906, July 2008.

[23] M. S. El Moursi, W. Xiao and J. L. Kirtley, "Fault ride through capability for grid interfacing large scale PV power plants", in *IET Generation, Transmission & Distribution*, vol. 7, no. 9, pp. 1027-1036, Sept. 2013.

[24] A. G. Yepes, F. D. Freijedo, J. Doval-Gandoy, O. Lopez, J. Malvar and P. Fernandez-Comesaña, "On the discrete-time implementation of resonant controllers for active power filters,", in *Industrial Electronics, 2009. IECON '09. 35th Annual Conference of IEEE*, Porto, 2009, pp. 3686-3691.

[25] M. Castilla, J. Miret, J. Matas, L. G. de Vicuña, and J. M. Guerrero, "Linear Current Control Scheme With Series Resonant Harmonic Compensator for Single-Phase Grid-Connected Photovoltaic Inverters", in *IEEE transaction on industrial electronics*, vol. 55, no. 7, July 2008.

[26] X. Yuan, W. Merk, H. Stemmler, and J. Allmeling, "Stationary-frame generalized integrators for current control of active power filters with zero steady-state error for current harmonics of concern under unbalanced and distorted operating conditions", in *IEEE Trans. Ind. Appl., vol. 38, no. 2, pp. 523–532, Mar./Apr. 2002.*

[27] K. Lim, J. Choi, J. Jang, S. Moon and J. Kim "Output voltage regulation based on P plus resonant control in islanded mode of microgrids", in *Power Electronics and Motion Control Conference and Exposition (PEMC), 2014 16th International,* Antalya, 2014, pp. 365-370.

[28] J. Hu, Y. He, L. Xu, and B. W. Williams, "Improved Control of DFIG Systems During Network Unbalance Using PI–R Current Regulators", in *IEEE Transactions on Industrial Electronics*, vol. 56, no. 2, pp. 439-451, Feb. 2009.

[29] A. S. Holter "Power Electronic Converter for Hybrid Power System with Smart Grid Functionality", *Specialization Project, NTNU*, Des. 2015.

[30] A. G. Yepes, F. D. Freijedo, Ó Lopez, and J. Doval-Gandoy, "High-Performance Digital Resonant Controllers Implemented With Two Integrators", in *IEEE Transactions on Power Electronics*, vol. 26, no. 2, pp. 563-576, Feb. 2011.

[31] A. G. Yepes, F. D. Freijedo, J. Doval-Gandoy, O. Lopez, J. Malvar, and P. Fernandez-Comesana, "Effects of discretization methods on the performance of resonant controllers", in *IEEE Transactions on Power Electronics*, vol. 25, no. 7, pp. 1692–1712, Jul. 2010.

[32] R. Nilsen, *Electric Drives*, NTNU, Department of Electric Power Engineering, 2016.

[33] S. Babaei, B. Fardanesh and S. Bhattacharya, "High-Power VSC-Based Simultaneous Positive- and Negative-Sequence Voltage Regulator", in *IEEE Transactions on Power Delivery* , vol. 29, no. 5, pp. 2124-2135, Oct. 2014.

[34] N. Jelani and M. Molinas, "Asymmetrical Fault Ride Through as Ancillary Service by Constant Power Loads in Grid-Connected Wind Farm", in *IEEE Transactions on Power Electronics* , vol. 30, no. 3, pp. 1704-1713, March 2015.

[35] M. Machaba, and M. Braae, "Explicit damping factor specification in symmetrical optimum tuning of PI controller", AFCON December 2003

[36] R. Bojoi, L. Limongi, F. Profumo, D. Roiu, and A. Tenconi, "Analysis of current controllers for active power filters using selective harmonic compensation schemes", in *IEEJ Trans. Electr. Electron. Eng.*, vol. 4, no. 2, pp. 139–157, 2009.

[37] IEC, "Electromagnetic compatibility (EMC) - Part 2-2: Environment - Compatibility levels for low-frequency conducted disturbances and signaling in public low-voltage power supply systems", in *IEC 61000-2-2*, 2002.

[38] H. P. A. P. W. Amarajeewa, L. H. P. N. Gunawardena, B. C. Harshani, M. A. S. N. Madurawala, and D. P. Chandima "Effective Current Harmonics Mitigation at Point of Common Coupling Using Multilevel Active Front End Converter", in *Information and Automation for Sustainability (ICIAfS), 2014 7th International Conference*, Colombo, pp. 1-6, 2014.

[39] J. M. Guerrero, "Tutorial Microgrids Connecting Renewable Energy Sources into the Smartgrid", in *14th European Conference on Power Electronics and Applications*, pp. 78, June, 2011.

[40] C. Rech and J. R. Pinheiro, "Line current harmonics reduction in multipulse connection of asymmetrically loaded rectifiers", in, *IEEE Transactions on Industrial Electronics*, vol. 52, no. 3, pp. 640-652, June 2005.

[41] T. M. Undeland, N. Mohan, and W. P. Robbins, *Power Electronics Converters, Applications and Design*, 3rd Edition: John Wiley & Sons, Inc., 2003.

[42] T. Hoevenaars, K. LeDoux and M. Colosino, "Interpreting IEEE STD 519 and meeting its harmonic limits in VFD applications", *Petroleum and Chemical Industry Conference, 2003. Record of Conference Papers. IEEE Industry Applications Society 50th Annual*, 2003, pp. 145-150.

[43] A. H. Hoevenaars, "The Answer to Harmonics: Is it Mitigation or a Robust Transformer?", *CEE News–The Power Quality Advisor*, 2000.

[44] R. I. Bojoi, G. Griva, V. Bostan, M. Guerriero, F. Farina and F. Profumo, "Current control strategy for power conditioners using sinusoidal signal integrators in synchronous reference frame", in *IEEE Transactions on Power Electronics*, vol. 20, no. 6, pp. 1402-1412, Nov. 2005.

[45] G. P. Liu, and S. Daley, "Optimal-tuning PID controller design in the frequency domain with application to a rotary hydraulic system", *Control Engineering Practice*, vol. 7, issue 7, pp. 821-830, July, 1999.

[46] K. G. Papadopoulos, N. D. Tselepis, and N. I. Margaris, "Analytical Tuning Rules of Digital PID Controllers for Integrating Processes via the Symmetrical Optimum Criterion", in *20th Mediterranean Conference on Control and Automation (MED)*, pp. 188-193, July, 2012.

[47] J. W. Umland, and M. Safiuddin, "Magnitude and symmetric optimum criterion for the design of linear control systems: what is it and how does it compare with the others?", in *Industry Applications, IEEE Transactions* pp. 489-497, March, 1990.

[48] R. Nilsen, L. E. Norum, "TET4120 - Electrical Drives", course held at *Norwegian University of Science and Technology, Department of Electrical Power Engineering*, 2016.

Appendix A

The Per-Unit System

In electrical systems as well as in control theory it is common to transform the physical system based on SI-parameters to into the per-unit system. This allows for a more standardized system description, making it more comparable to similar systems. A per-unit transformation of an arbitrary parameter, is carried out by dividing the physical value by a predefined system base-value.

A.1 Per-Unit Transformations of the Active Front End Converter System

The per-unit transformations applied in this thesis are listed below, with physical parameters written in uppercase letters, and per-unit quantities in lowercase letters. The base values are derived as follows:

- Phase voltage: $V_{base} = \sqrt{\frac{2}{3}} V_n$
- Phase current: $I_{base} = \sqrt{2} I_n$
- Impedance: $Z_{base} = \frac{V_{base}}{I_{base}}$
- Angular frequency: $\omega_{base} = \omega_0$
- Power: $S_{base} = \frac{3}{2} V_{base} I_{base}$

- DC link voltage: $V_{DC,base} = 2V_{base}$

Using, these base values, the per-unit values of the AFE converter can be expressed as listed below:

- Filter reactances: $x_l = \frac{\omega_0 L_1}{Z_{base}}$
  $x_c = \frac{1}{\omega_0 C_1 Z_{basis}}$
- Filter resistance: $r_1 = \frac{R_1}{Z_{base}}$

Appendix B

Control Theory

A summary of some of the basic control theory from [21] applied throughout this thesis is given here. Figure B.1 depicts a generic control system with unity feedback which is affected by two contributions, namely, the input reference signal, y^*, and the disturbance, v. The reference signal is compared to the measured controller output, y, for computation of the error signal, e. This error is fed into the the controller block, $D(s)$, which objective is to make the output track the reference, forcing the error to zero, as well as suppressing the disturbance. The plant transfer function, $G(s)$, represents the system to be controlled.

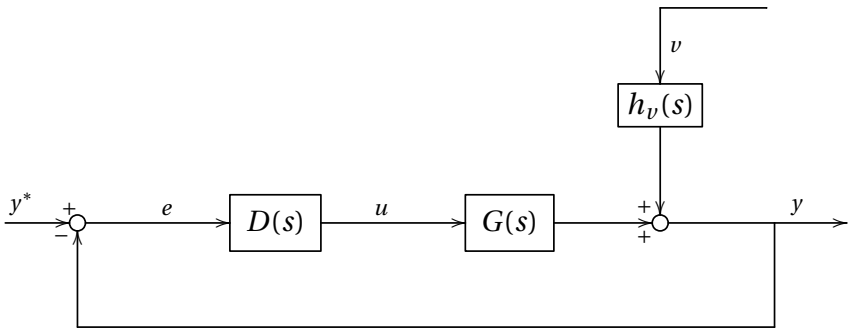

Figure B.1: Generic block diagram of a feedback loop control system

Considering Figure B.1, the transfer function of the output, y is given by (B.1):

$$y(s) = \frac{D(s)G(s)}{1+D(s)G(s)}y^*(s) + \frac{1}{1+D(s)G(s)}h_v(s)v(s) \tag{B.1}$$

As can be seen from Equation (B.1), the open loop system transfer function from the reference, y^*, to the output, $h_0(s)$, can be derived through superposition by neglecting the contribution from the disturbance, that is, by letting $v = 0$ and ignoring the feedback loop.

$$h_0(s) = D(s)G(s) \tag{B.2}$$

Furthermore, this relation can be used to express the *closed loop transfer function*, again neglecting the effect of the disturbance:

$$h_{cl}(s) = \frac{y}{y^*}(s) = \frac{h_0(s)}{1 + h_0(s)} \tag{B.3}$$

The transfer function of (B.3) is also referred to as the *tracking transfer function*, playing av important role when analyzing how well the output is tracking the reference signal. Whenever $h_{cl} = 1$, perfect reference tracking is achieved. Considering Equation (B.3), this corresponds to having $|h_0| >> 1$. Again, studying Figure B.1, and the relation of Equation (B.1), the effect of the disturbance, v, on the output, y, can be derived through superposition, now neglecting the reference input, that is, by letting $y^* = 0$:

$$\frac{y}{v}(s) = \frac{1}{1 + h_0(s)} h_v(s)\, v(s) \tag{B.4}$$

In, B.4, the *sensitivity transfer function*,

$$S(s) = \frac{1}{1 + h_0(s)} \tag{B.5}$$

is present. In order to obtain perfect reference tracking, (B.4) shows that the magnitude of the sensitivity transfer function should be zero ($|S(s)| = 0$), which again corresponds to having $|h_0| >> 1$. Moreover, the sensitivity transfer function directly expresses the effect that the applied feedback is having on suppressing the disturbances.

Another important tool for analyzing control systems are the *Bode diagram*, which is a plot of the system frequency response. A bode diagram showing the frequency response of a generic open loop transfer function is shown in Figure B.2.

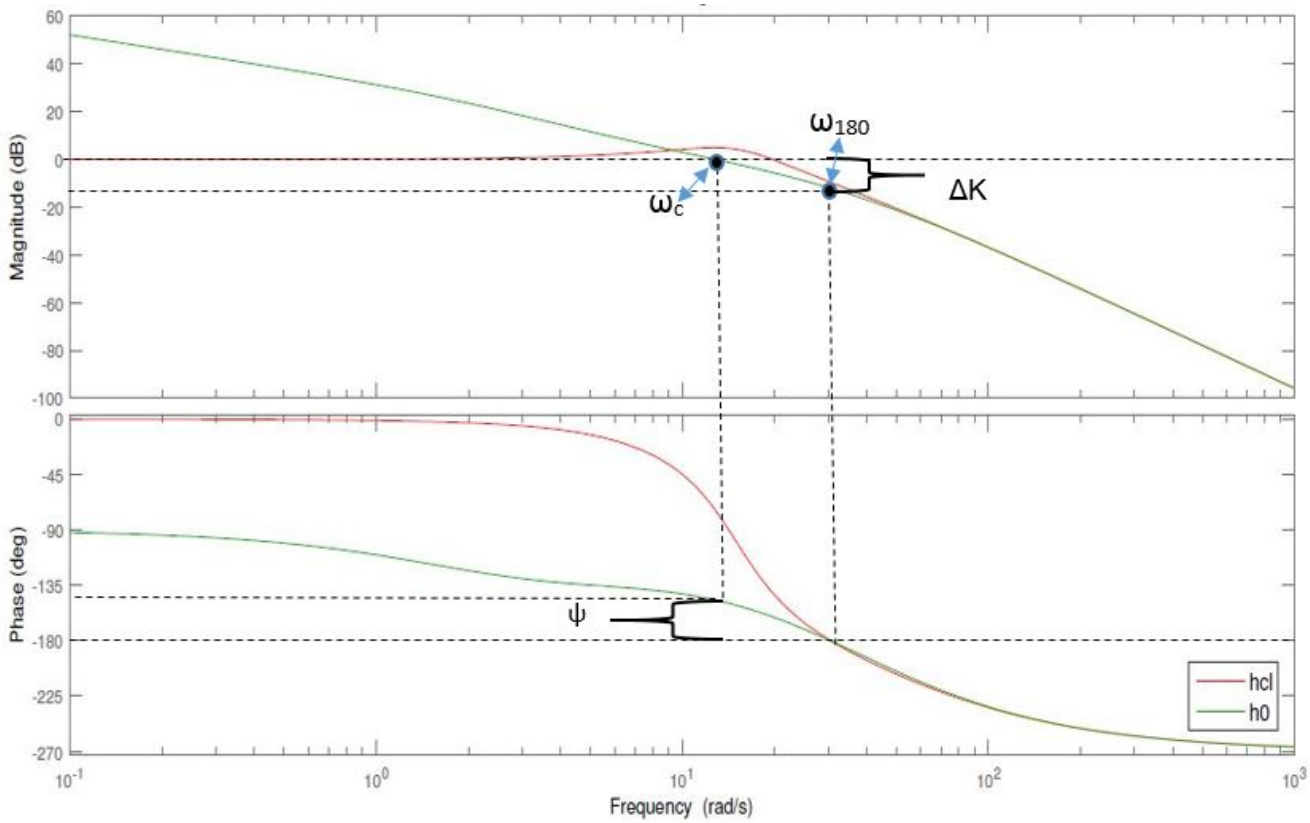

Figure B.2: Generic bode diagram of an open and a closed loop transfer function displaying the phase margin, ψ, and gain margin, ΔK

In the bode diagram, the decibel scale is applied, having the following relation between the absolute amplitude and the decibel unit of the ordinate axis:

$$|h(j\omega)|\,[dB] = 20\,log_{10}\,|h(j\omega)| \tag{B.6}$$

The system cross-frequency, ω_c, can be read directly from the bode diagram of the open loop transfer function and corresponds to the frequency at which $|h_0(j\omega)| = 0\,[dB]$. The frequency at which the phase drops below $-180°$, ω_{180}, is another important point to notice in the bode plot. Considering these two frequencies of the bode diagram, it can be showed that the system of interest is stable if the following apply:

$$\angle h_0(j\omega_c) < 180°, \quad |h_0(j\omega_{180})| < 1 = 0\,[dB], \tag{B.7}$$

The limits indicated in (B.7) are an adaptation of the *Nyquist stability criterion* [21]. By defining

expressions for the system *phase margin*, ψ, and *gain margin*, ΔK, according to:

$$\psi = \angle h_0(j\omega_c) - (-180^\circ), \quad \Delta K = \frac{1}{|h_0(j\omega_{180})|}, \tag{B.8}$$

the stability criterion of (B.7) can be redefined as:

$$\psi > 0, \quad \Delta K > 1 = 0\,[dB] \tag{B.9}$$

Due to possible system parameter modifications over time, it is common to define some stability margin. Typical stability phase, and gain margins are, $\psi \geq 45^\circ$ and $\Delta K \geq 2 = 6\,[dB]$, respectively. Bode plots of the tracking- and sensitivity transfer functions can also be applied for system analysis. One property that is particularly important for control systems tracking a sinusoidal reference, is that the magnitude of $\angle h_{cl}(j\omega)$ in these cases directly reflects the phase deviation of the regulator output signal, y.

Appendix C

Simulation Blocks and Complementary Results

C.1 Complementary Simulation Results for Case 5

Here, the simulation results of the harmonic performance presented in Chapter 7, Case 5 are presented.

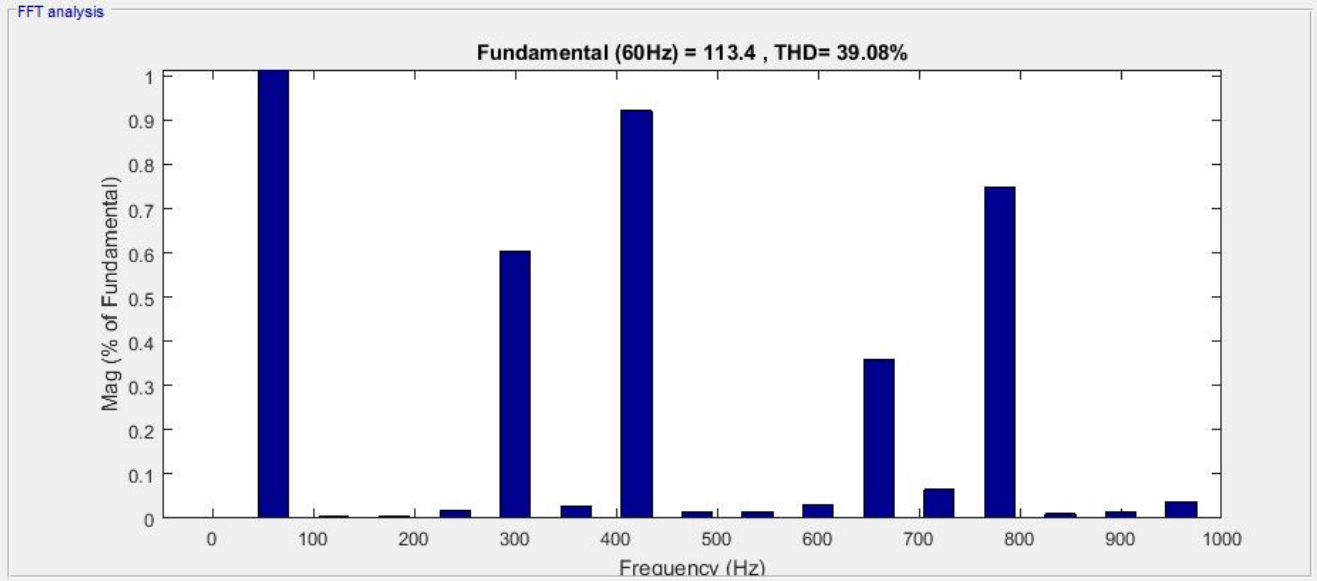

Figure C.1: Complete current harmonic spectrum of Case 5, Chapter 7 of PIR current controller *without* harmonic compensation

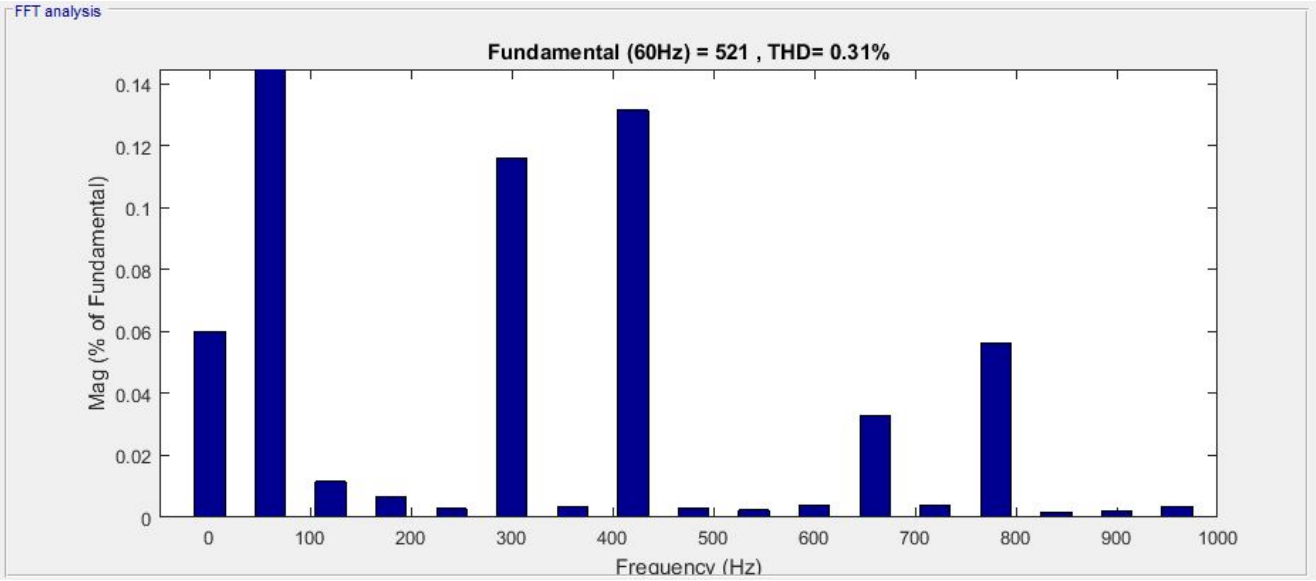

Figure C.2: Complete voltage harmonic spectrum of Case 5, Chapter 7 of PIR current controller *without* harmonic compensation

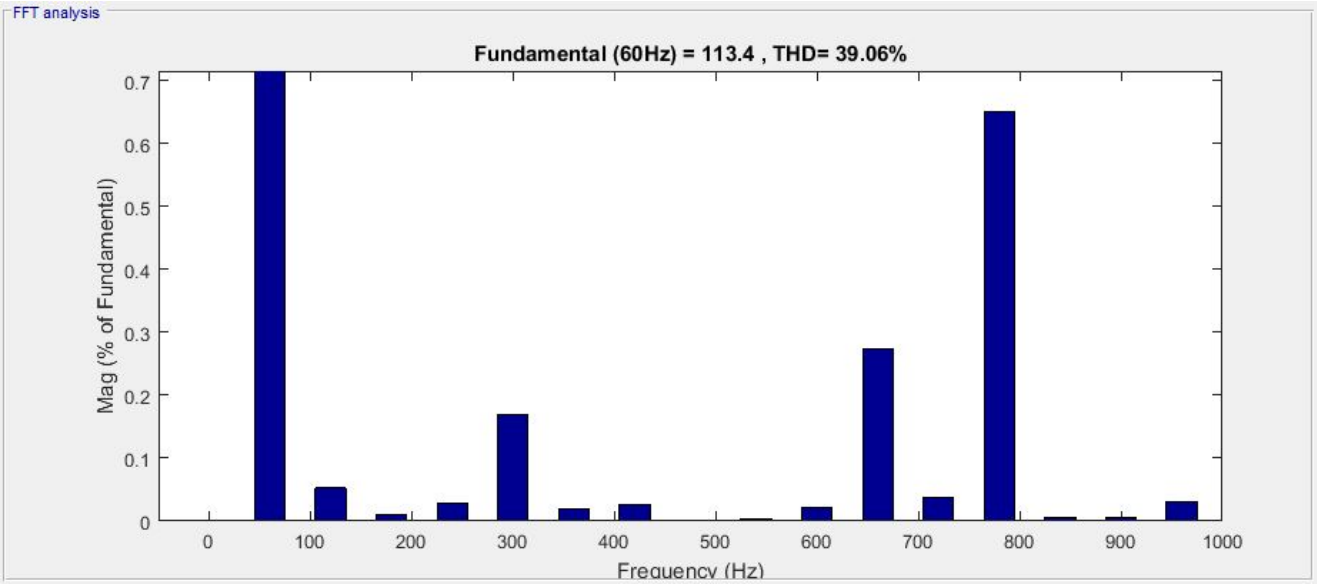

Figure C.3: Complete current harmonic spectrum of Case 5, Chapter 7 of PIR current controller *with* harmonic compensation

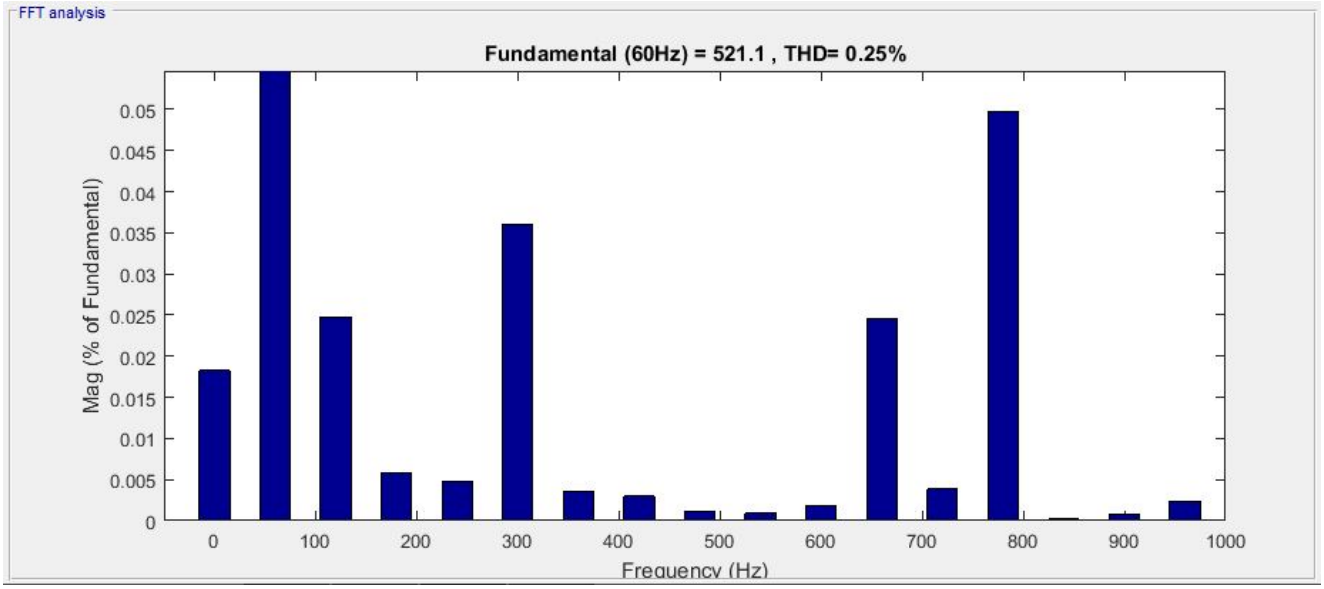

Figure C.4: Complete voltage harmonic spectrum of Case 6, Chapter 7 of PIR current controller *with* harmonic compensation

C.2 Complementary Simulation Results for Case 6

Figure C.5 shows the simulation model of the inner current control loop and the outer voltage loop, employing PI + multi-resonant $\alpha\beta$-controllers, control structure corresponding to that of Figure 6.30.

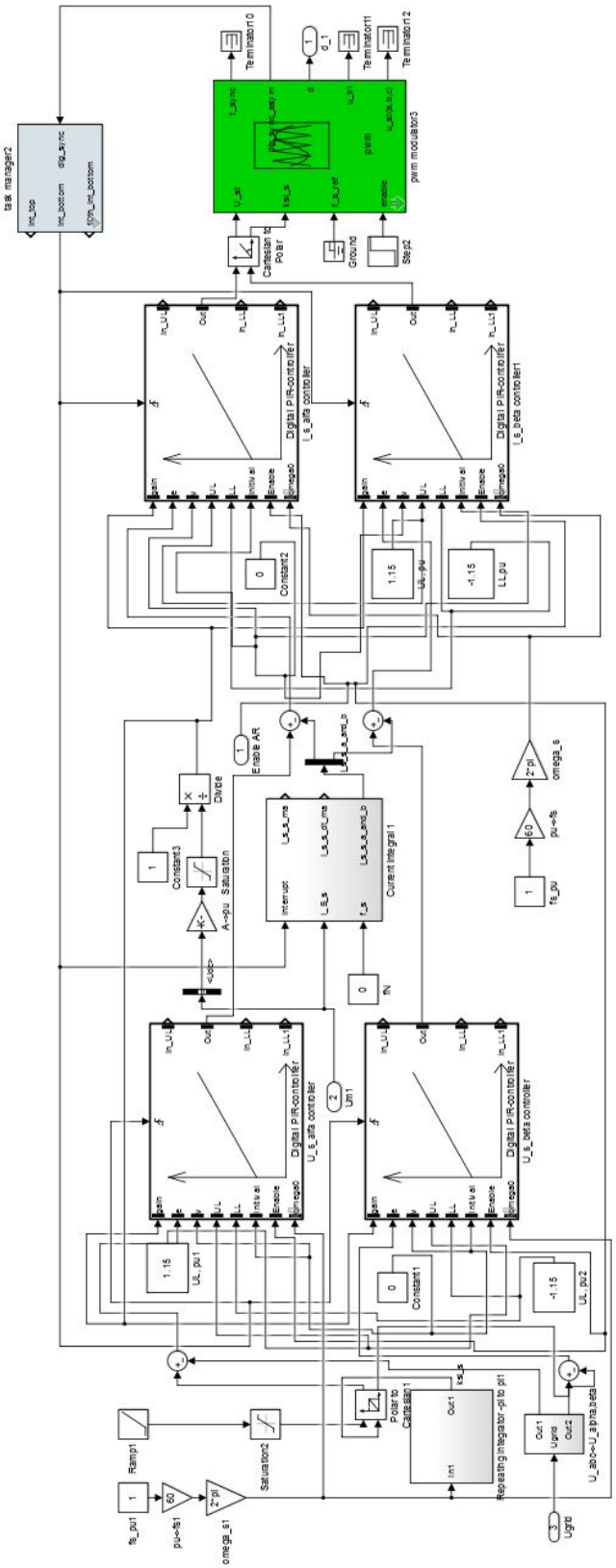

Figure C.5: Simulation model of inner current control loop and outer voltage control loop

Here, the simulation results of the harmonic performance presented in Chapter 7, Case 6 are presented.

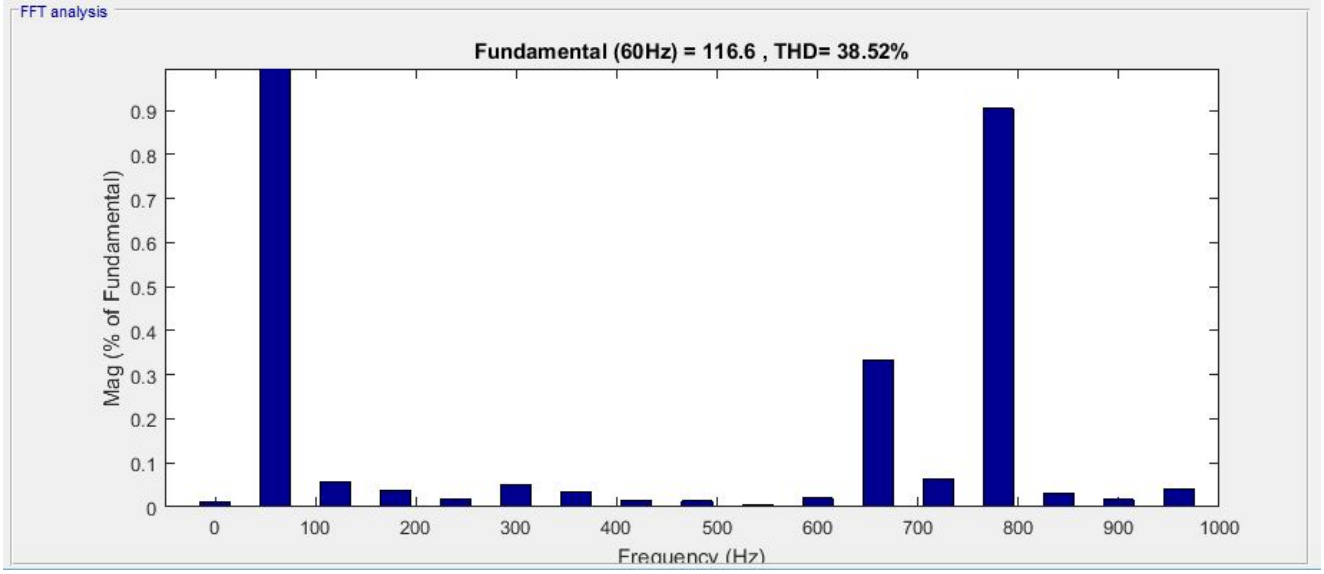

Figure C.6: Complete current harmonic spectrum of Case 6, Chapter 7, of PIR current and voltage controllers with harmonic compensation

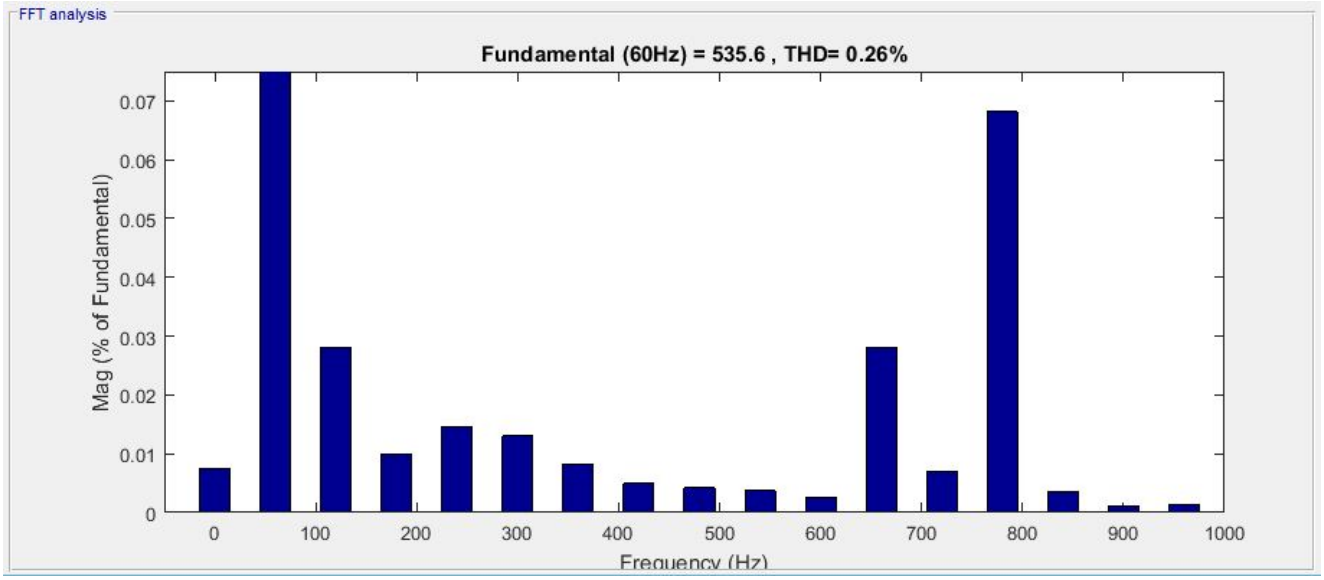

Figure C.7: Complete voltage harmonic spectrum of Case 6, Chapter 7, of PIR current and voltage controllers with harmonic compensation

C.3 Complementary Simulation Results for Case 7

Figures C.8-C.9 show the harmonic spectrum for the converter output current and the capacitor voltage with connection to the full-bridge diode rectifier load.

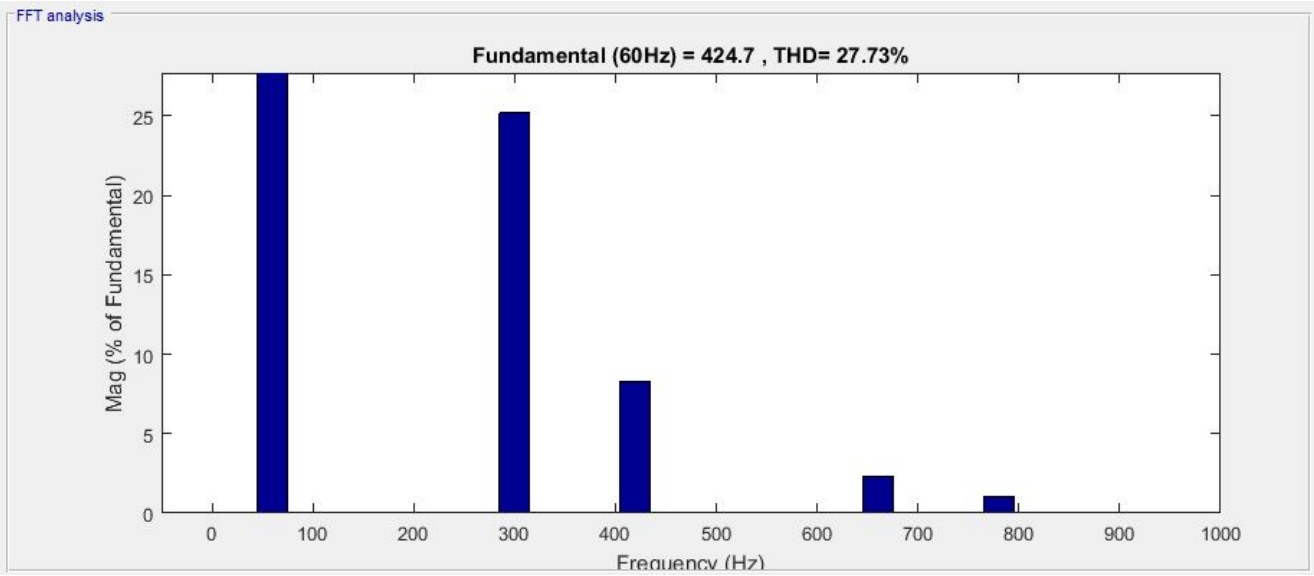

Figure C.8: Complete current harmonic spectrum of Case 7, Chapter 7, with PIR current and voltage controllers with harmonic compensation and nonlinear load

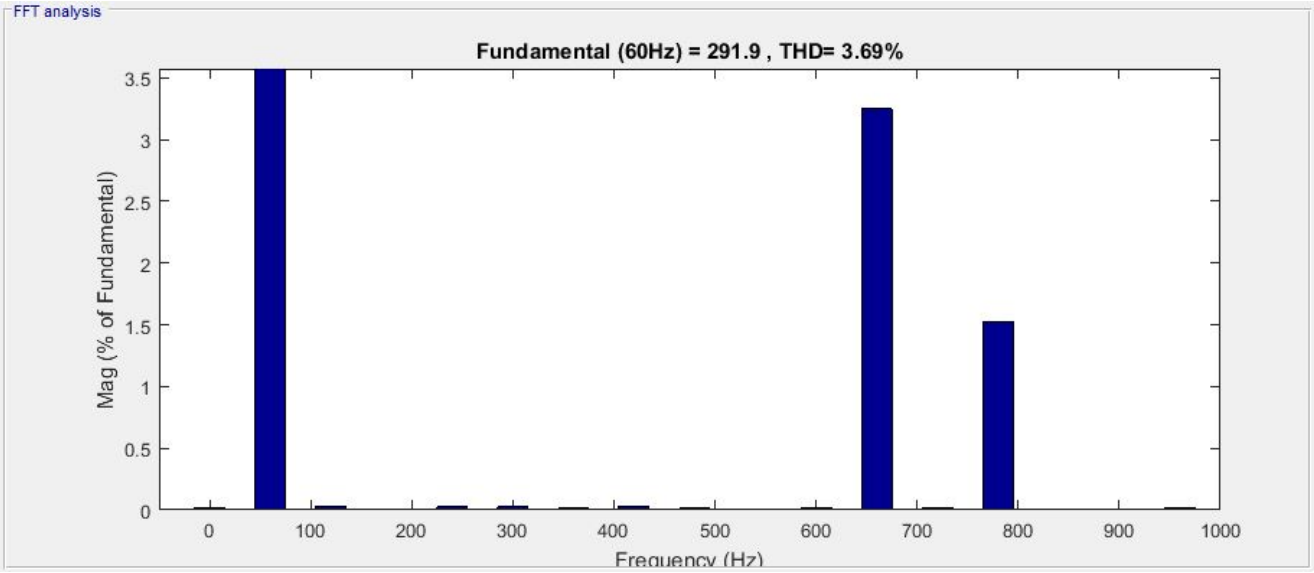

Figure C.9: Complete voltage harmonic spectrum of Case 7, Chapter 7, with PIR current and voltage controllers with harmonic compensation and nonlinear load

The effect of the harmonic compensation is evident when considering the voltage spectrum

of Figure C.9, where $h = 3,5$ is compensated for while, $h = 11,13$ are the dominant higher order frequency components.